Towards upscaling the Battolyser- An Integrated Ni-Fe Alkaline Battery and Electrolyser A combined modeling and experimental study

Mangel Raventos, A.

DOI
10.4233/uuid:b980646c-b40f-48f1-977e-9ccb4a86bcab

Publication date
2023

Document Version
Final published version

Citation (APA)
Mangel Raventos, A. (2023). *Towards upscaling the Battolyser- An Integrated Ni-Fe Alkaline Battery and Electrolyser: A combined modeling and experimental study*. [Dissertation (TU Delft), Delft University of Technology]. https://doi.org/10.4233/uuid:b980646c-b40f-48f1-977e-9ccb4a86bcab

TOWARDS UPSCALING THE BATTOLYSER- AN INTEGRATED NI-FE ALKALINE BATTERY AND ELECTROLYSER

A COMBINED MODELING AND EXPERIMENTAL STUDY

TOWARDS UPSCALING THE BATTOLYSER- AN INTEGRATED NI-FE ALKALINE BATTERY AND ELECTROLYSER

A COMBINED MODELING AND EXPERIMENTAL STUDY

Dissertation

for the purpose of obtaining the degree of doctor
at Delft University of Technology,
by the authority of the Rector Magnificus prof. dr. ir. T.H.J.J. van der Hagen,
chair of the Board of Doctorates,

to be defended publicly on
FRIDAY 31 of MARCH 2023 at 10:00am

by

Andrea MANGEL RAVENTOS

Master of Science in Sustainable Energy Technologies,
Delft University of Technology, Netherlands
born in San Jose, Costa Rica.

This dissertation has been approved by:

promotor: prof. dr. ir. W. de Jong
promotor: prof. dr. F. M. Mulder
copromotor: dr. R. Kortlever

Composition of the doctoral committee:

Rector Magnificus,	voorzitter
Prof. dr. ir. W. de Jong,	Technische Universiteit Delft
Prof. dr. F. M. Mulder,	Technische Universiteit Delft
Dr. R. Kortlever,	Technische Universiteit Delft
Independent members:	
Dr. A. Forner-Cuenca	Technische Universiteit Eindhoven
Prof. dr. P.P. Pescarmona	Rijksuniversiteit Groningen
Prof. dr. T. Breugelmans,	Universiteit Antwerpen
Prof. dr. ir. O. Isabella,	Technische Universiteit Delft
Prof. dr. ir. J.T. Padding,	Technische Universiteit Delft, reservelid

An electronic version of this dissertation is available at
http://repository.tudelft.nl/.

Pero si algo habían aprendido juntos era que
la sabiduría nos llega cuando ya no sirve para nada.

Gabriel García Márquez

CONTENTS

List of Figures xi

List of Tables xv

Summary xvii

Samenvatting xix

1 Introduction 1
- 1.1 Scope of the Thesis . . . 4
  - 1.1.1 Research Questions . . . 5
  - 1.1.2 Outline of the Thesis . . . 5

2 Literature Review 9
- 2.1 Large-scale renewable energy storage technologies . . . 10
  - 2.1.1 Size and application . . . 10
  - 2.1.2 Technical maturity . . . 11
- 2.2 Water electrolysis . . . 11
- 2.3 Alkaline Electrolysis . . . 13
  - 2.3.1 Fundamentals . . . 13
  - 2.3.2 Thermodynamics . . . 14
  - 2.3.3 Kinetics . . . 15
  - 2.3.4 Resistance and loss mechanisms . . . 16
  - 2.3.5 Electrocatalyst materials . . . 16
  - 2.3.6 Cathode catalysts . . . 18
  - 2.3.7 Anode catalysts . . . 18
  - 2.3.8 Catalyst surface . . . 19
  - 2.3.9 Electrolyte . . . 20
  - 2.3.10 Efficiency . . . 21
  - 2.3.11 New developments . . . 21
- 2.4 Nickel-Iron batteries . . . 22
  - 2.4.1 Fundamentals . . . 23
  - 2.4.2 Electrolyte . . . 23
  - 2.4.3 Advantages . . . 24
- 2.5 An integrated Ni-Fe battery and electrolyser- the battolyser . . . 24

3 Modeling the Performance of an Integrated Battery and Electrolyzer System 31
- 3.1 Introduction . . . 33
- 3.2 Modeling and experimental methods . . . 35
  - 3.2.1 Model . . . 35
  - 3.2.2 Experimental Validation . . . 40

3.3 Results and Discussion . . . 41
3.3.1 Model Validation . . . 41
3.3.2 Optimization of Battolyser Parameters . . . 42
3.3.3 Design Recommendations . . . 45
3.4 Conclusions . . . 46

4 Effect of Different Alkali Metal Cations on the Oxygen Evolution Activity and Battery Capacity of Nickel Electrodes in Concentrated Hydroxide Electrolytes 53
4.1 Introduction . . . 55
4.2 Experimental methods . . . 56
4.2.1 Electrode preparation for RDE experiments . . . 56
4.2.2 Electrolyte preparation . . . 57
4.2.3 Rotating Disk Electrode (RDE) measurements . . . 57
4.2.4 Battery cycling . . . 58
4.3 Results and discussion . . . 58
4.3.1 Rotating disk electrode measurements . . . 58
4.3.2 Battery cycling . . . 62
4.3.3 Battolyser electrolyte optimization . . . 63
4.4 Conclusions . . . 65
4.5 Acknowledgements . . . 66

5 Effect of flow in an integrated battery and electrolyser system- A preliminary experimental study 71
5.1 Introduction . . . 72
5.2 Experimental methods . . . 73
5.2.1 Cell design and setup . . . 73
5.2.2 Experimental tests . . . 74
5.3 Results and discussion . . . 74
5.3.1 Effect of the gap and the membrane . . . 74
5.3.2 Effect of the shadowed area . . . 74
5.3.3 Comparing different flow field patterns . . . 76
5.4 Conclusions . . . 78
5.4.1 Further experiments . . . 78

6 Conclusions and Recommendations 83
6.1 Conclusions . . . 84
6.2 Recommendations . . . 85

A Appendix Chapter 3 87
A.1 Model parameters . . . 87
A.2 SEM images of electrode particles . . . 90
A.3 XRD of electrode materials . . . 91
A.4 BET surface area calculation . . . 92
A.5 Elemental composition of the electrode materials . . . 93
A.6 Experimental setup for validation . . . 94
A.7 Model validation at different charging rates . . . 96

A.8 Gap thickness and electrolyte conductivity optimization 97
A.9 Electrolyte concentration profiles calculated with the model 100

B Appendix Chapter 4 **103**
B.1 RDE results 103
B.2 Battery cycling data comparison 105
B.3 SEM images for the nickel electrode used in 1 M MOH Battery cycling experiments 108
B.4 Elemental composition of the commercial nickel electrode materials 109
B.5 RDE Setup 111
B.6 Battery cycling Setup 112
B.7 Additional CVs 113

C Appendix Chapter 5 **117**

D Nomenclature **123**

Curriculum Vitæ **127**

List of Publications **129**

List of Figures

1.1 Net renewable capacity additions by technology, 2017-2023[9] 2
1.2 (a) Global radiation values in Delft, The Netherlands, on a sunny spring day. (b) Average global radiation values in the Netherlands for one calendar year 3
1.3 Overview of various storage types[15] 3
1.4 Inputs and outputs required to run a battolyser system. 5
1.5 Upscaling the battolyser- a schematic representation of future integration into energy systems. 6

2.1 Different energy storage technologies, divided into 5 categories: chemical, electrical, electrochemical, mechanical, and thermal technologies[1]. . . . 11
2.2 System power rating and discharge time at rated power for various large-scale energy storage systems[2]. 12
2.3 Polarization curves and specific energy consumption (in kWh/m^3) of main water electrolysis technologies: (1 in blue) alkaline electrolysers (AEL), (2 in green) solid polymer electrolysers (PEMEL), (3 in red) high temperature solid-oxide electrolysers (SOEL) [13]. 13
2.4 A schematic representation of a simple alkaline electrolysis cell. 14
2.5 Operational regimes depending on the applied potential and temperature for hydrogen production [16]. 15
2.6 Distribution of cell voltage in alkaline water electrolysis [16] [20] 17
2.7 Overpotential in V at 10 mA/cm^2 for various catalysts in Acid and Base electrolytes[24]. 17
2.8 3D plot of specific conductivity of KOH with respect to temperature and concentration calculated with an empirical correlation proposed by Gilliam et al.[33]. 20
2.9 Schematic representation of a Nickel-Iron battery and the charging/discharging reactions. 22
2.10 Charge and discharge curves of a typical Ni-Fe battery- voltage characteristics at constant current charge/discharge [47] 24
2.11 Schematic representation of the battolyser operation during charging and electrolysis. 25

3.1 Schematic illustration of the chemical reactions that occur during charging, overcharging, and discharging of the battolyser. 34
3.2 Schematic diagram of battolyser cells and their model representation including the Ni(OH)2 positive electrode, aqueous KOH electrolyte, polyphenylene sulphide separator and Fe(OH)2 negative electrode. 36

3.3 a) Schematic diagram of the cell geometry used for validation and b) a comparison of the cell potential during charge and discharge cycles at constant current for experimental and simulation results. Cell potential vs. time during a galvanostatic charge and discharge cycle. Charging and discharging at C/5 rate equal to 2 A. 41
3.4 a) Battery and total integrated energy efficiency with respect to the scaling electrode thickness factor, where n is multiplied by the electrode thickness to analyze the effect of decreasing and increasing the electrode thickness, and b) battery capacity and total hydrogen production vs. scaling electrode thickness factor. 44
3.5 a) Battery and total integrated efficiency with respect to the electrode porosity, and b) battery capacity and total hydrogen production vs. the electrode porosity. 45

4.1 Cyclic voltammograms of $Ni(OH)_2$ material deposited on a GC electrode recorded in different electrolytes with a total OH- concentration of 6.5 M. Measurements were performed using an RDE setup with a rotation speed of 1600 rpm and the voltammograms were recorded at scan rate of 20 mVs^{-1}. Five cycles were performed, and the figure shows the third cycle for all electrolyte compositions. The currents are normalized by milligrams of $Ni(OH)_2$ electrocatalyst present for the sake of comparison. 59
4.2 Peak oxidation (red) and reduction (green) potential of the $Ni(OH)_2$ /NiOOH redox couple and the potential at which 200 mA/mg for OER (blue) is reached for different electrolyte compositions. (a) LiOH, (b) NaOH, (c) RbOH, and (d) CsOH additions to a KOH electrolyte. Data from cyclic voltammograms of a $Ni(OH)_2$ film deposited on a GC-RDE at 1600 rpm. 61
4.3 Changes in the discharge capacity after 30 subsequent charging/discharging cycles in 5 M KOH (activation), electrolyte mixtures (MOH electrolyte) and 5 M KOH (after MOH). The discharge capacity of the last cycle of each phase is calculated and compared to the capacity after activation of each individual battery. Changes in the discharge capacity are displayed as percentages with respect to the activation phase as references. The figures shows electrolytes containing: (a) LiOH, (b) NaOH, (c) RbOH, and (d) CsOH additions to a KOH electrolyte. 63
4.4 Cell potentials at which gas evolution (H_2 and O_2 evolution) occurs after full charging NiFe batteries for 17 different electrolyte compositions at a 2 A charging current. Average values of 5 cycles are presented, where the error bars indicate the maximum and minimum values of the 5 last cycles. 64

5.1 Schematic view of the flow cell designed and built for this study, (a) exploded view of the serpentine flow field design and (b) stacked cell. 73
5.2 Charge/discharge curve of the battolyser flow setup with one empty FFP vs. 2 empty FFPs and a separator. 75
5.3 Schematic view of the flow field pattern (FFP) designs; a) Serpentine pattern, b) Parallel pattern, c) Empty pattern. 75

5.4 Charge/discharge curve of the battolyser flow setup with different FFPs without flow. 76
5.5 Charge/discharge curve of the battolyser flow setup with the Empty flow field pattern at different flow field rates. 77
5.6 Charge/discharge curve of the battolyser flow setup with the (a) serpentine and (b) parallel flow field pattern at different flow field rates. 77
5.7 Charge/discharge curve of the battolyser flow setup with the serpentine flow field pattern at different flow field rates with one serpentine FFP and no membrane. 78

A.1 Standard electrode potential of the nickel hydroxide positive electrode dependent on state of charge of the battery[1]. 88
A.2 SEM-SEI images of the active electrode material. (a) Nickel positive electrode material and (b) Iron negative electrode material. 90
A.3 . XRD analysis of the active electrode material. (a) Nickel positive electrode material, where the red lines indicate the peaks associated with β- $Ni(OH)_2$ and the blue lines are related to graphitic carbon peaks and (b) Iron negative electrode material, where the red lines indicate peaks associated with magnetite Fe3O4 and the blue lines are again related to the graphitic carbon content. 91
A.4 BET surface area plot for the nickel and iron materials. 92
A.5 (a) Commercial battery setup including: 3 positive nickel electrodes (in green), 2 negative iron electrodes (in grey), alkaline electrolyte and rubber separators (black) to avoid short-circuits. The cell is encased in a plastic casing with metal connectors for the positive and negative electrodes. (b) Schematic of the reverse burette experimental setup to measure the total gas production (c) Experimental setup used to measure total gas production. 94
A.6 Cell potential vs. elapsed time during a charging gas production cycle . . . 95
A.7 Cell potential vs. elapsed time during a charging gas production cycle at (a) 1.5A (b) 2A and (c) 4A. 96
A.8 (a) Battery and total integrated efficiency with respect to a scaling factor that multiplies the gap thickness (b) Battery capacity and total hydrogen production vs. gap thickness. 97
A.9 (a) Battery and total integrated efficiency with respect to the electrolyte conductivity (b) Battery capacity and total hydrogen production vs. electrolyte conductivity. 98
A.10 Specific conductivity of KOH with respect to concentration at 20 °C. Data from Gilliam et al. [6] 99
A.11 ((a) Hydroxide concentration profiles in the x-coordinate during charge and electrolysis (b) Hydroxide concentration profiles in the x-coordinate during discharge. 100

B.1 (a)-(d) Cyclic voltammogram of a $Ni(OH)_2$ film deposited on a GC-RDE at 1600 rpm with 6.5 M MOH electrolytes, where M consists of the K^+ and Li^+, Na^+, Rb^+ and Cs^+ additions. (a) LiOH concentrations, (b) NaOH concentrations, (c) RbOH concentrations, and (d) CsOH concentrations added to a KOH electrolyte, while keeping the final OH^- contentration at 6.5 M. . . . 103
B.2 Battery charge/discharge cycles with different MOH concentration additions. . . . 107
B.3 SEM SEI images at x2000 magnification of the nickel electrode material from batteries with the highest concentrations of alkali metal cations. (a) 1M LiOH + 5.5M KOH, (b) 1M NaOH + 5.5M KOH, (c) 1M RbOH + 5.5M KOH, (d) 1M CsOH + 5.5M KOH. . . . 108
B.4 (a) Photograph and (b) schematic of the RDE setup used for experiments. 111
B.5 (a) Photograph of the (a) Battery charging setup and (b) commercial Ni-Fe IronCore batteries used for experiments. . . . 112
B.6 Cyclic voltammograms of $Ni(OH)_2$ material deposited on a GC electrode recorded in different electrolytes with a total OH- concentration of 6.5 M. Measurements were performed using an RDE setup with a rotation speed of 1600 rpm and the voltammograms were recorded at scan rate of 20 mV s1 in the following electrolyte compositions: (a) 5.5M KOH + 1M LiOH, (b) 5.5M KOH + 1M NaOH, (c) 5.5M KOH + 1M RbOH, (d) 5.5M KOH + 1M CsOH, (e) 6.5M KOH. . . . 113
B.7 Figure 1 with current density in mA/cm-2, using the geometric surface area of the GC electrode. . . . 114

C.1 Electrode frame . . . 118
C.2 End plate frame . . . 119
C.3 Empty flow plate pattern frame . . . 120
C.4 Parallel flow pattern frame . . . 121
C.5 Serpentine flow pattern frame . . . 122

List of Tables

2.1 Main electrocatalyst materials and their current development [28] 19

3.1 Optimized cell parameters 46

4.1 Electrolyte composition variations used in this study. The total hydroxide concentration is kept constant at 6.5 M, while different alkali hydroxides (M = Li, Na, Cs, Rb) are mixed with KOH. 57
4.2 Battery cycling test steps and details 58

A.1 Kinetic parameters for the battery charging reactions for $Ni(OH)_2$ from [1]. 87
A.2 Kinetic parameters for the gas production reaction (OER and HER) on both electrodes. 88
A.3 Parameter values used- base case scenario. 89
A.4 ICP-OES results for the nickel and iron electrode sample 93

B.1 Peak oxidation potential and peak reduction potential of cycle 3 of consecutive CVs shown in Figure B.1 compared to the average value of 3 consecutive cycles. 104
B.2 ICP-OES results for the nickel electrode sample 109

D.1 Variables and greek symbols used throughout the document. 123
D.1 Variables and greek symbols used throughout the document. 124
D.2 Subscripts, superscripts and abbreviations used throughout the document. 125

SUMMARY

Electrochemical cells and systems have been around for a few centuries. Lately, these technologies have been attracting attention. Although the technology to generate electricity from renewable sources is well developed and widely available -such as photovoltaic and wind energy- this is not always available. Because of this, it is necessary to store produced surplus electricity to be able to use it at moments when the sun is not shining or the wind is not blowing. Many different electrochemical technologies can be used to store electricity or transform it to a useful energy carrier- such as hydrogen. However, the energy transition will also need to address the optimal usage of critical materials. Integrating functionalities and optimizing energy storage can help bridge the gap between electricity production and consumption using only a limited amount of critical materials.

New innovative technologies that use less critical materials will be key to sustainably transition to a fossil-fuel free future. It will be necessary to move forward and upscale technologies at a quick pace. A combined modeling and experimental approach can help move through the TRL development stages quickly, optimizing the use of resources and experimental work required.

The battolyser is a new integrated battery and electrolyser system that provides flexibility in energy storage. During periods of high availability of renewable energy it can be charged indefinitely, filling up the battery capacity first and producing hydrogen from there on out. A battolyser system can be used to guarantee access to cheap electricity and green hydrogen, all in one device and using the materials required for one device.

Modeling the electrochemical reactions of the battolyser and optimizing the cell design parameters when moving towards an upscaled system is a tool that can be used for the continuous development of a better prototype and scaling up. Chapter 3 describes the modeling studies performed on the battolyser system, including the relevant experimental validation. Here, a 1D COMSOL model was developed to study the cell parameters and understand the effect of electrode and gap thickness, electrode porosity, and electrolyte conductivity.

Testing experimentally at larger scales is challenging and often not done. Highly alkaline KOH electrolytes are usually not tested in lab conditions, and therefore the effect of higher concentrations than 5M KOH is unknown on new electrode material developments. To optimize an integrated device, the effect on both the electrolysis function and the battery function need to be reconciled and designed for the specific application. In Chapter 4, extensive lab scale experiments on the electrolyte concentration are described, including different alkali metal cation concentrations. To optimize for different functionalities of the battolyser, different cations can be used at specific concentrations.

A flow cell was designed and built, and different flow configurations were tested. 3D printing technology allows for quick iterations and modifications of the design, however the proprietary resins are usually not tested at highly alkaline conditions which could

potentially cause degradation of the cell components. Working with higher than 5M KOH concentrations results in practical difficulties that will only scale with plant capacity. In Chapter 5, the preliminary results of a flow cell configuration are included.

The results of this work can be applied directly to predict the optimal design and operating parameters of an up-scaled battolyser cell. This will allow for quicker iterations of up-scaled designs to further develop the prototype technology. For this, it is important to verify simulation results with experimental data. Using a combined approach including simulations and experimental work allows testing various setups and optimizing the energetic efficiency of the device. 3D printing manufacturing technology can also help speed up this iterative process to generate design modifications and quickly manufacture experimental setups to validate the simulation data.

SAMENVATTING

Elektrochemische cellen en systemen bestaan al een paar eeuwen, maar de laatste tijd staan deze technologieën opnieuw in de schijnwerpers. Hoewel de technologie om elektriciteit op te wekken uit hernieuwbare bronnen, zoals fotovoltaïsche en windenergie, goed ontwikkeld en algemeen beschikbaar is, is de toevoer uit deze bronnen niet altijd beschikbaar. Daarom is het noodzakelijk om ongebruikte geproduceerde elektriciteit op te slaan om deze later te kunnen gebruiken op momenten dat de zon niet schijnt of de wind niet waait. Veel verschillende elektrochemische technologieën kunnen worden gebruikt om elektriciteit op te slaan of een bruikbare brandstof te produceren, zoals waterstof. De energietransitie is echter ook een kwestie van optimaal gebruik van kritieke grondstoffen. Door functionaliteiten te integreren en energieopslag te optimaliseren, kan de kloof tussen elektriciteitsproductie en -verbruik worden overbrugd met slechts een beperkte hoeveelheid kritieke grondstoffen.

Nieuwe innovatieve technologieën, die minder kritieke grondstoffen gebruiken, zullen de sleutel zijn tot een duurzame overgang naar een toekomst zonder fossiele brandstoffen. Het is noodzakelijk om in een snel tempo vooruit te gaan en technologieën op te schalen. Een gecombineerde aanpak van modellering en experimenteel werk kan helpen om snel door de TRL-ontwikkelingsfasen te gaan, waarmee het gebruik van middelen en experimenteel werk kan worden geoptimaliseerd.

De battolyser is een nieuw geïntegreerd batterij- en elektrolysersysteem dat flexibiliteit biedt in de opslag van energie. Tijdens periodes van hoge beschikbaarheid van hernieuwbare energie kan het onbeperkt worden opgeladen, waarbij eerst de batterijcapaciteit volledig wordt gevuld en hierna waterstof wordt geproduceerd. Met een battolysersysteem kan de toegang tot goedkope elektriciteit en groene waterstof worden gegarandeerd, alles met slechts de benodigde materialen voor één enkel apparaat.

Het modelleren van de elektrochemische reacties in de battolyser en het optimaliseren van het ontwerp zijn hulpmiddelen die kunnen worden gebruikt voor de continue ontwikkeling van een beter prototype en de opschaling hiervan. In hoofdstuk 3 worden de modelstudies beschreven die zijn uitgevoerd op het battolyser-systeem, inclusief de relevante experimentele validatie hiervan. Een 1D COMSOL-model is ontwikkeld om de celparameters te bestuderen en het effect van de dikte en porositeit van de electrode, afstand tussen de elektrodes, en geleidbaarheid van het elektrolyt te begrijpen.

Het experimenteel testen van het prototype op grotere schaal is een uitdaging en wordt vaak niet gedaan. Sterk basische KOH-elektrolyten worden meestal niet getest onder laboratoriumomstandigheden, en daarom is het effect van concentraties hoger dan 5M KOH op nieuwe elektrodematerialen niet bekend. Om een geïntegreerd apparaat te kunnen optimaliseren, moet het effect van de hogere concentraties KOH op zowel de elektrolyse- als de batterijfunctie van de battolyser worden afgestemd en aangepast voor de specifieke toepassing. In Hoofdstuk 4 worden uitgebreide experimenten op laboratoriumschaal beschreven met betrekking tot de elektrolytconcentratie, inclusief concen-

traties van verschillende kationen. Verschillende kationen kunnen worden gebruikt in specifieke concentraties om de functionaliteiten van de battolyser te optimaliseren.

Er is een flow-cell ontworpen, gebouwd, en op verschillende stroomconfiguraties getest. 3D-printen maakt het mogelijk snel iteraties en aanpassingen aan het ontwerp uit te voeren, maar de gebruikte harsen van de 3D printer worden meestal niet getest onder sterk basische omstandigheden waardoor mogelijk degradatie van de celcomponenten wordt veroorzaakt. Hogere concentraties dan 5M KOH veroorzaken praktische problemen die alleen maar zullen toenemen met de productiecapaciteit. In Hoofdstuk 5 zijn de voorlopige resultaten van een flow-cell configuratie opgenomen.

De resultaten van dit werk kunnen direct worden toegepast om het optimale ontwerp en gebruiksparameters van een opgeschaalde battolyser-cel te voorspellen. Dit zal leiden tot snellere iteraties van opgeschaalde ontwerpen om de technologie van de battolyser verder te ontwikkelen. Hiervoor is het belangrijk om resultaten van simulaties te verifiëren met experimentele gegevens. Door een gecombineerde aanpak toe te passen kunnen verschillende opstellingen worden getest en kan de energetische efficiëntie van het apparaat worden geoptimaliseerd. 3D-printproductietechnologie kan ook helpen dit iteratieve proces te versnellen om ontwerpwijzigingen te genereren en snel experimentele opstellingen te genereren die kunnen worden gebruikt om de gegevens uit de simulatie te valideren.

1

Introduction

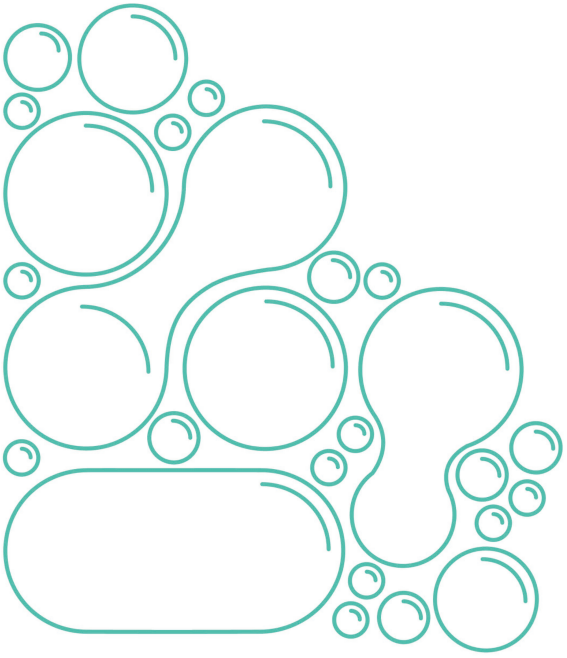

1

In 2016, the levels of CO_2 in the atmosphere reached the threshold of 400 ppm. The combustion of fossil fuels accounts for the majority of anthropogenic greenhouse gas (GHG) emissions[1]. The increasing concentration of CO_2 in the atmosphere together with a growing world population show the need for a shift in primary energy generation technologies[2]. To reduce the amount of carbon based emissions into the atmosphere, fossil fuel consumption has to decrease. Renewable energy technologies have the technical maturity to fulfil the necessary energy requirements[3]. However, due to the intermittent nature of renewable technologies such as solar and wind, storage will play an important role in the future energy systems. Although a large amount of research has been focused on large-scale energy storage, technologies are still techno-economically not mature for utility-scale storage[4][5][6]. In the near future, when electricity production will mostly be dependent on renewable energy sources, increased storage capacity will be critical in security of energy supply[7][8].

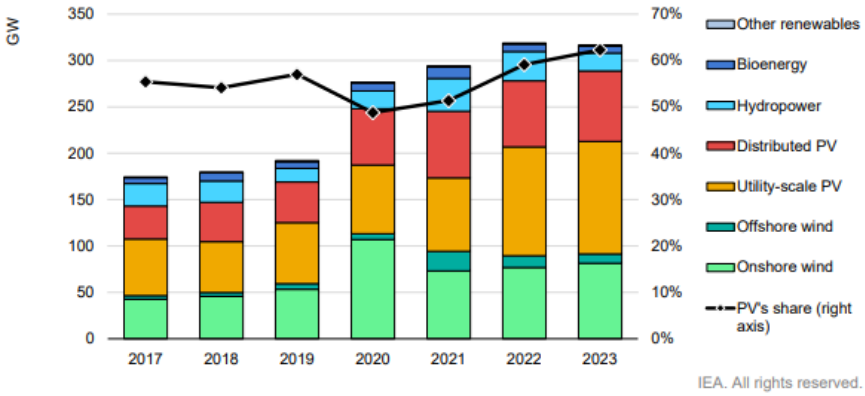

Figure 1.1: Net renewable capacity additions by technology, 2017-2023[9]

Increase in net renewable capacity in the last 6 years can be seen in Figure 1.1, with a mostly stable capacity predicted for 2023 unless stronger policies are implemented. Although net capacity is expected to stay constant, installed photovoltaic capacity is predicted to grow. Additionally, new policies and incentives are expected to provide incentives to further increase renewable energy capacity in Europe[9].

Solar energy is the most widely available form of renewable energy. In one year, the total amount of radiation incident on Earth is more than the total fossil fuel reserves on Earth[10]. Even though solar energy is widely available, it is inherently fluctuating[11][12]. As an example, typical global radiation values of solar energy in Delft are presented in Figure 1.2, on a (a) daily time scale and (b) a yearly time scale with data obtained from METEONORM software.

The availability of sustainable energy technologies, together with the ambitious Renewable Energy Directive sets rules for the EU to achieve 32% renewables target by 2030, suggest an increase in the variability of electricity generation. Therefore, an electrical grid completely based on renewable energy will result in mismatch between production and consumption[5][10]. Currently, the storage needed to balance this mismatch is

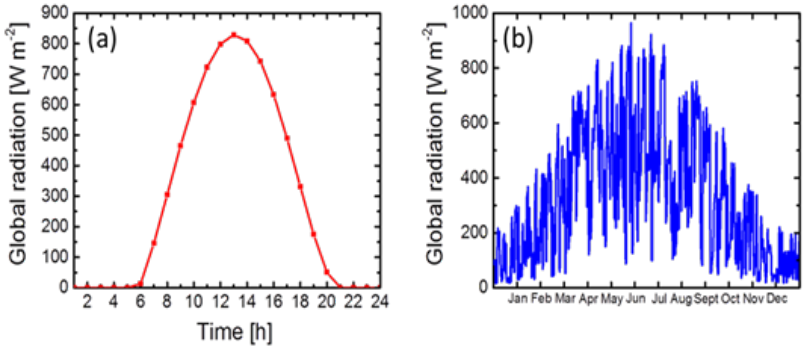

Figure 1.2: (a) Global radiation values in Delft, The Netherlands, on a sunny spring day. (b) Average global radiation values in the Netherlands for one calendar year

provided by fossil fuels. As the renewable energy capacity increases and fossil fuel use decreases, an alternative storage technology will be needed.

Batteries are an attractive option to cover short-term fluctuations because of their high round trip efficiency, typically around 80%[13]. However, due to their limited cycling rate and self-discharge, batteries alone cannot meet long-term energy storage requirements[14]. Battery overall energy capacity scales with the amount of material, and would consequently require extensive amount of battery material for seasonal energy storage. More importantly, the cost of long-term battery storage would be prohibitive for large applications[14]. Therefore, an alternative solution for long-term energy storage is required. A summary of different storage technologies and their scale is shown in Figure 1.3. Hydrogen can cover a broad range of capacities and power ranges[15].

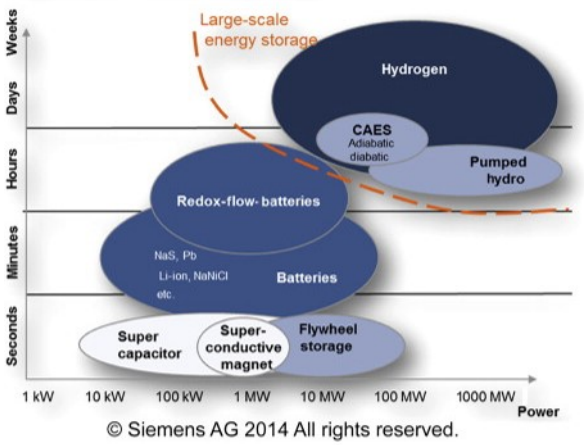

Figure 1.3: Overview of various storage types[15]

Electrochemical conversions, or power-to-x technologies, can bridge the gap be-

tween power production and power consumption and provide a means for longer-term seasonal energy storage. Power-to-x can refer to the production of different molecules, such as methane, ammonia, or hydrogen, using renewable electricity as main driving force. Although very attractive in theory, these technologies, except for some specific examples of water electrolysis, are still not deployed on the utility level scale. Hydrogen gas is a carbon-free alternative energy carrier, thus water electrolysis has been the subject of research and policy developments[16][17][18]. In addition, hydrogen as a feedstock has a significant role in current chemical process industry, which may be extended to various other energy and feedstock roles in a renewable future. For instance, hydrogen as a feedstock or energy carrier could decarbonise steel, concrete production, and ammonia synthesis, large chemical processes responsible for bulk fractions of industrial CO_2 emissions[19].

The battolyser system offers an integrated storage solution, where a battery is used for short term storage, such as daily time scales, and hydrogen is produced as a long-term storage method, for seasonal variations in renewable energy production. As soon as the battery becomes fully charged, hydrogen is produced through electrolysis, as a clean fuel can that can be produced during high renewable energy production periods[20]. Hydrogen is a carbon-free energy carrier that can be burned in a gas turbine, engine, or used in a fuel cell. The only by-product of pure hydrogen combustion is water[1][21].

The battolyser is comprised out of two different storage mechanisms: a nickel-iron battery and an alkaline electrolyser. The nickel-iron battery serves as a short-term energy storage mechanism. It stores electricity in the form of chemical bonds which can then be transformed back into electricity[22]. When the maximum battery capacity is reached, the device acts as an alkaline electrolyser, using the electricity available to split water molecules in the electrolyte, thus generating hydrogen[20]. This carbon-free fuel can be stored and later used, for example, in a fuel cell for electricity production in periods of low renewable energy availability. This device combines short-term and long-term storage options which will be an essential attribute for future renewable energy systems.

1.1. SCOPE OF THE THESIS

The battolyser technology was demonstrated at lab scale, and patented in 2018[23]. This thesis is focused on the parameters necessary to upscale the technology. Studies were performed, both computationally and experimentally, to determine the optimum unit cell composition. These include a model and experimental verification of the unit cell parameters. Further studies on the composition of the electrolyte and the effects on both the battery component and the electrolyser component were performed at two different scales. Finally, a preliminary study of the effect of liquid flow on the electrode surface was performed. For this, a lab scale setup was designed and built, and experiments were run. This is represented by the illustration in Figure 1.5 as the steps to upscale the prototype technology to a full-scale utility battolyser that can be used for industry and grid stabilization. A block diagram of the inputs and outputs required to run a battolyser system is included in Figure 1.4.

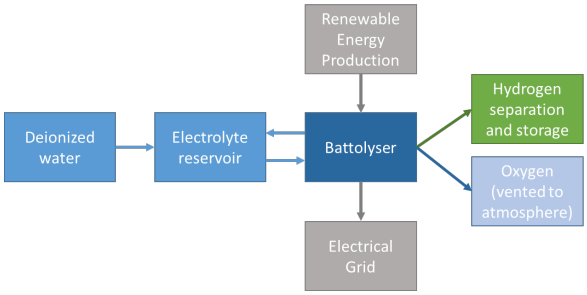

Figure 1.4: Inputs and outputs required to run a battolyser system.

1.1.1. RESEARCH QUESTIONS

The main research question addressed throughout this thesis is: How can the battolyser prototype be improved so as to enable upscaling?

The research subtopics presented here, each refer to a specific chapter in the thesis:

- How can we model the performance of the unit cell and improve its performance?
- What is the impact of alkali metal cations on the performance of an integrated battery and electrolyser?
- What is the effect of different electrolyte flow configurations and flow rate for an integrated battery and electrolyser?

1.1.2. OUTLINE OF THE THESIS

Chapter 1 has given the reader a general introduction to the topic. Next, in Chapter 2, the basic theory behind both technologies will be discussed, including theoretical background information necessary to understand the simulation and experimental work done in the next chapters. Chapter 3 is based on a publication in Industrial & Engineering Chemistry Research and details the simulation work done to design the optimum unit cell layout of the battolyser. Chapter 4 includes the experimental study and is based on published work in Electrochimica Acta regarding the composition of the electrolyte and the effect of alkaline metal cations on the electrolyser and battery performance in the integrated device. Chapter 5 is a preliminary study on the effects of flow, detailed by an experimental study with a lab-scale setup designed and built in house. Finally, 6 includes conclusions and recommendations for further research regarding the battolyser.

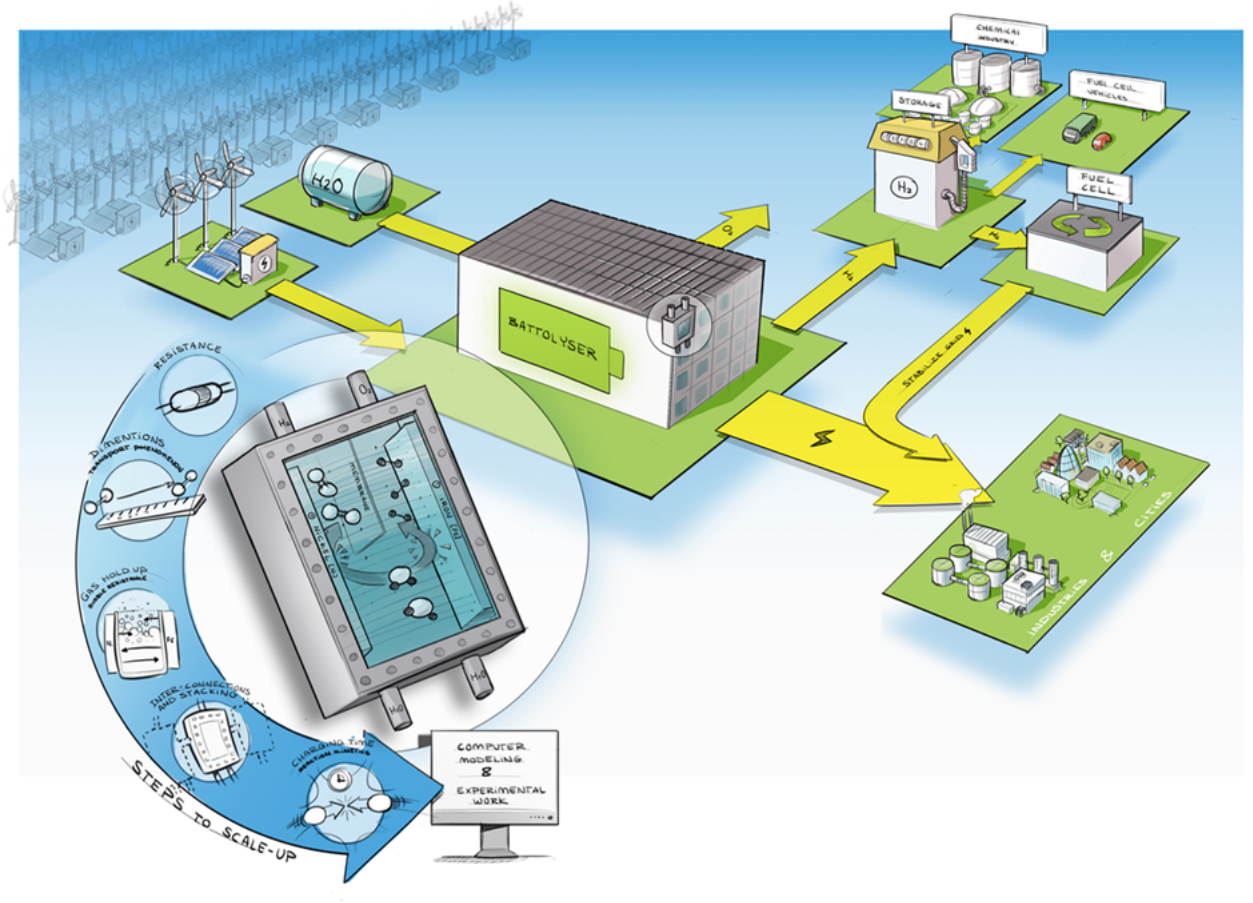

Figure 1.5: Upscaling the battolyser- a schematic representation of future integration into energy systems.

BIBLIOGRAPHY

[1] R. Quadrelli and S. Peterson, "The energy–climate challenge: Recent trends in CO2 emissions from fuel combustion", *Energy policy*, vol. 35, no. 11, pp. 5938–5952, 2007.

[2] P. Denholm, E. Ela, B. Kirby, and M. Milligan, "Role of energy storage with renewable electricity generation", National Renewable Energy Lab.(NREL), Golden, CO (United States), Tech. Rep., 2010.

[3] IEA, *World energy outlook 2020*. OECD Publishing, 2020.

[4] S. Kapila, A. O. Oni, and A. Kumar, "The development of techno-economic models for large-scale energy storage systems", *Energy*, vol. 140, pp. 656–672, 2017.

[5] P. Denholm and G. L. Kulcinski, "Life cycle energy requirements and greenhouse gas emissions from large scale energy storage systems", *Energy Conversion and Management*, vol. 45, no. 13-14, pp. 2153–2172, 2004.

[6] R. Hemmati, H. Saboori, and M. A. Jirdehi, "Multistage generation expansion planning incorporating large scale energy storage systems and environmental pollution", *Renewable Energy*, vol. 97, pp. 636–645, 2016.

[7] S. P. Badwal, S. S. Giddey, C. Munnings, A. I. Bhatt, and A. F. Hollenkamp, "Emerging electrochemical energy conversion and storage technologies", *Frontiers in chemistry*, vol. 2, p. 79, 2014.

[8] F. Mulder, "Implications of diurnal and seasonal variations in renewable energy generation for large scale energy storage", *Journal of Renewable and Sustainable Energy*, vol. 6, no. 3, p. 033 105, 2014.

[9] IEA, "Renewable energy market update", *IEA, Paris*, 2020.

[10] N. Kannan and D. Vakeesan, "Sun based vitality for future world: A survey", *Exam Clean Sustain Energy*, vol. 62, pp. 1092–1105, 2016.

[11] C. S. Tao, J. Jiang, and M. Tao, "Natural resource limitations to Terawatt-scale solar cells", *Solar Energy Materials and Solar Cells*, vol. 95, no. 12, pp. 3176–3180, 2011.

[12] J. B. Goodenough, "Energy storage materials: A perspective", *Energy storage materials*, vol. 1, pp. 158–161, 2015.

[13] A. Evans, V. Strezov, and T. J. Evans, "Assessment of utility energy storage options for increased renewable energy penetration", *Renewable and Sustainable Energy Reviews*, vol. 16, no. 6, pp. 4141–4147, 2012.

[14] K. Agbossou, M. Kolhe, J. Hamelin, and T. K. Bose, "Performance of a stand-alone renewable energy system based on energy storage as hydrogen", *IEEE Transactions on energy Conversion*, vol. 19, no. 3, pp. 633–640, 2004.

[15] P. Moseley and J. Garche, *Electrochemical energy storage for renewable sources and grid balancing*. Newnes, 2014.

[16] S. Sasanpour, K.-K. Cao, H. C. Gils, and P. Jochem, "Strategic policy targets and the contribution of hydrogen in a 100% renewable european power system", *Energy Reports*, vol. 7, pp. 4595–4608, 2021.

[17] B. D. Solomon and A. Banerjee, "A global survey of hydrogen energy research, development and policy", *Energy policy*, vol. 34, no. 7, pp. 781–792, 2006.

[18] IRENA, "Scaling up electrolysers to meet the 1.5°*C* climate goal", *International Renewable Energy Agency, Abu Dhabi*, 2020.

[19] C. Philibert, "Renewable energy for industry", *Paris: International Energy Agency*, vol. 65, 2017.

[20] F. M. Mulder, B. M. H. Weninger, J. Middelkoop, F. G. B. Ooms, and H. Schreuders, "Efficient electricity storage with a battolyser, an integrated Ni–Fe battery and electrolyser", *Energy Environ. Sci.*, vol. 10, no. 3, pp. 756–764, 2017.

[21] A. Ozarslan, "Large-scale hydrogen energy storage in salt caverns", *International journal of hydrogen energy*, vol. 37, no. 19, pp. 14 265–14 277, 2012.

[22] B. Hariprakash, S. Martha, M. Hegde, and A. Shukla, "A sealed, starved-electrolyte nickel–iron battery", *Journal of Applied Electrochemistry*, vol. 35, no. 1, pp. 27–32, 2005.

[23] F. M. Mulder, *Hybrid battery and electrolyser*, WO/2016/178564, Nov. 2016.

2

Literature Review

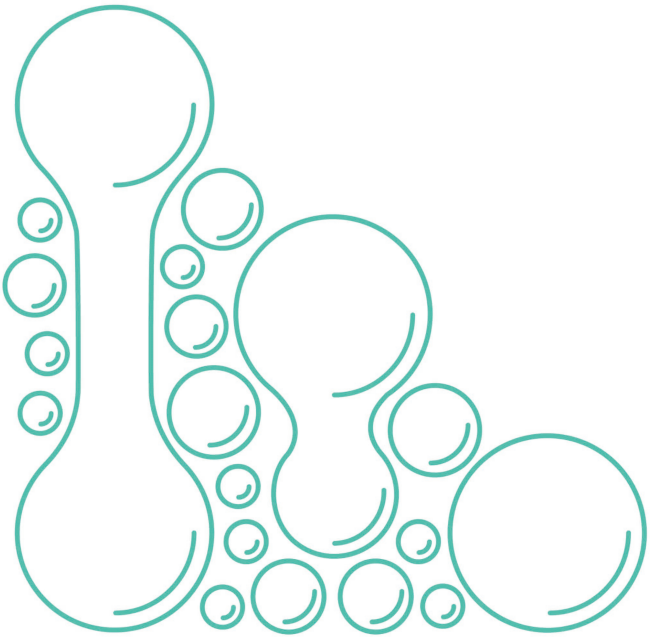

2.1. LARGE-SCALE RENEWABLE ENERGY STORAGE TECHNOLOGIES

The increasing penetration of intermittent renewable energy requires a considerable amount of large-scale energy storage for utility level and industry-scale requirements of power availability. Due to the inherent fluctuations of wind and solar energy, the installation of large scale renewable electricity generation will undoubtably include grid-scale instabilities of power availability. Many different technologies are being developed to provide the storage capacity required, including batteries, electrolysis for hydrogen production, compressed or liquefied air storage, thermal storage, and pumped hydropower storage, among many other technologies. Battery technologies are composed of numerous different chemical compositions, each with their own technical limitations and advantages. Many battery compositions are considered mature technologies that can be implemented at high technology readiness levels (TRL) currently. Pumped hydropower storage requires large footprints and a geographically specific location with altitude differences that can be used to store potential energy in the form of water. Hydrogen and fuel cells have been gaining interest regarding power generation in the last decade as much of the EU policy regarding climate change is geared towards the adaptation of hydrogen as a carbon-free energy carrier.

2.1.1. SIZE AND APPLICATION

Energy storage technologies can be subdivided into chemical, electrical, electrochemical, mechanical, and thermal technologies. Some examples of energy storage technologies available or under development are presented in Figure 2.1.

Because of the growing need for and flexibility required for renewable energy systems of the future, energy storage technologies have gained traction in both the research and policy space. Depending on the application and the discharge time required, different technologies are available to provide the energy storage required. Figure 2.2 shows the scale and rated power of different large-scale energy storage technologies currently in the market.

Storage systems on the bottom of Figure 2.2 are used for power quality applications. Discharge times of minutes to an hour are used for bridging power and power quality applications, while the technologies shown on the top of Figure 2.2 with discharge times of hours and longer are used for energy management applications[3].

Each technology has an ideal application and energy storage scale. Therefore, to obtain an optimal system, the specifications of the storage device and application have to be analyzed[4]. Large-scale energy storage can improve the system quality and reliability by providing electricity during peak periods [3]. To develop a fully renewable power generation system, a combination of all time scales will be required.

Apart from the technical challenges, cost is still an issue to deploy these technologies at massive scales required for widespread use of renewable energy. As many of the storage technologies mentioned are in the early stages of commercialization, it is difficult to predict the levelized costs of storage (LCOS) for future applications. Many studies have been performed, however variations in LCOS calculations are high and equal comparisons are difficult to establish[5][6][7].

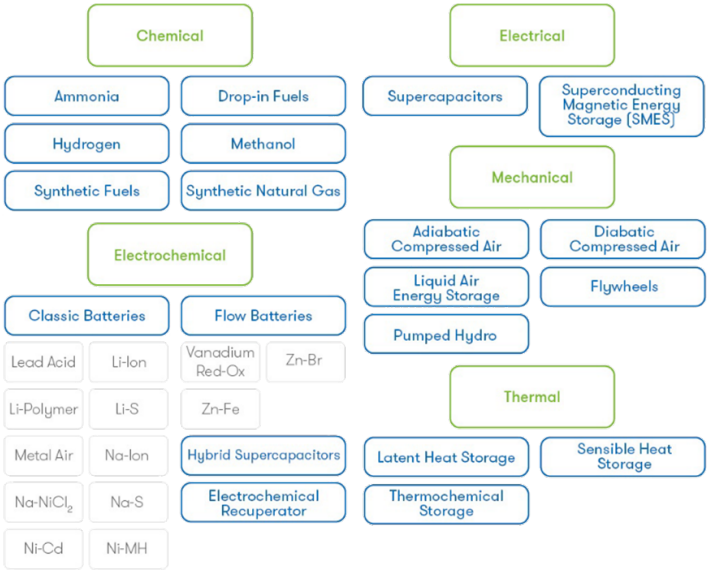

Figure 2.1: Different energy storage technologies, divided into 5 categories: chemical, electrical, electrochemical, mechanical, and thermal technologies[1].

2.1.2. TECHNICAL MATURITY

Technical maturity can be assessed using the TRL scale, as advised by the European Commission for research and innovation projects. The scale goes from 1-9, with 1 and 2 referring to basic technology research and 9 being a fully commercial technology available on the market. Some of the technologies included in Figure 2.2 can be placed high on the TRL scale, however integration and full deployment in operational environments is currently not the case. Because of this, although already on the market and commercially available, most of the technologies shown above are still under intensive research and development[4].

2.2. WATER ELECTROLYSIS

Water electrolysis was discovered around 200 years ago by William Nicholson and Anthony Carlisle. The invention of the Gramme machine in 1869, made water electrolysis an economical method for hydrogen production[8]. However, nowadays less than 5% of worldwide hydrogen is produced through electrolysis[8]. Hydrogen is mostly produced from natural gas through steam methane reforming (SMR)[9]. Compared to SMR, water electrolysis has the benefit of producing extremely pure hydrogen (>99.9%). This is ideal for processes where high hydrogen purity is required[8]. Other advantages of electrolysis include fast start-up and shutdown times, making it ideal for intermittent renewable energy sources[10].

During the late 19th century, alkaline electrolysis was the main chemical process

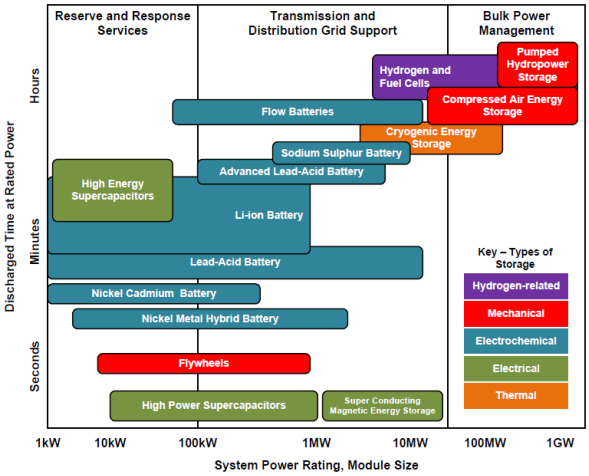

Figure 2.2: System power rating and discharge time at rated power for various large-scale energy storage systems[2].

used to produce hydrogen[11]. In 1902, more than 400 industrial alkaline electrolysers were in operation worldwide[12].

In the 1960s, large scale systems for industrial applications were commercially available. All the systems were based on alkaline electrolytes and operated at atmospheric pressure with asbestos fabric as diaphragm[11]. Using cheap and widely available hydropower, hydrogen could be widely produced. Towards the end of the 20th century, the growing production of fossil hydrocarbons shifted production methods towards coal gasification and natural gas steam reforming, mainly for economic reasons[11]. Due to this shift in production methods, water electrolysis technology has not changed drastically in the last 100 years. Currently, because of the world-wide requirements for carbon-free energy carriers, research has again been focused on electrochemical production of hydrogen through electrolysis.

The main technologies have been defined depending on the electrolyte used in the cell.

- Alkaline electrolysis (AEL)
- Proton exchange membrane electrolysis (PEMEL)
- Solid oxide electrolysis (SOEL)
- Proton conductive ceramic electrolysis (PCCEL)

The polarization curves and specific energy consumption of the first three technologies mentioned are included in Figure 2.3. Alkaline electrolysers are more robust and the technology is mature and well known. Alkaline electrolysers are generally less expensive to manufacture and operate than PEM electrolysers. PEM electrolysers have a

fast response time and can thus be used in conjunction with renewable energy generation patterns[13]. Additionally, higher current densities can be obtained. With PEM electrolyser systems, the balance of plant can be streamlined and results in a lower capital expenditure per megawatt of hydrogen produced. Solid oxide electrolysers operate at higher temperatures and are built out of ceramic materials. Because of the high temperatures, operation is not flexible and not suited for dynamic control, as the ramp-up and ramp-down periods are slow. Solid oxide electrolysers are not yet demonstrated at industrial scale.

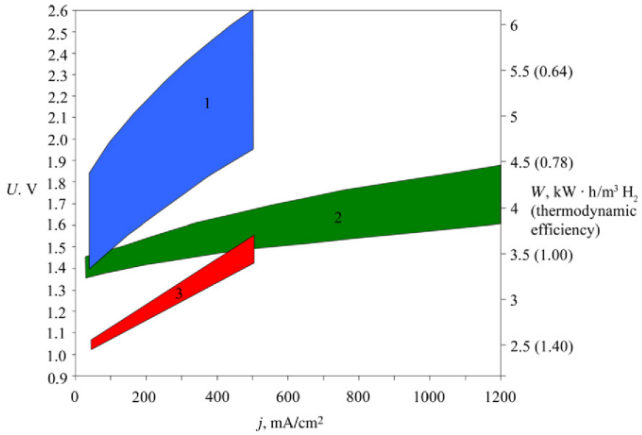

Figure 2.3: Polarization curves and specific energy consumption (in kWh/m^3) of main water electrolysis technologies: (1 in blue) alkaline electrolysers (AEL), (2 in green) solid polymer electrolysers (PEMEL), (3 in red) high temperature solid-oxide electrolysers (SOEL) [13].

2.3. ALKALINE ELECTROLYSIS

2.3.1. FUNDAMENTALS

An alkaline electrolyser can be described, in the simplest terms, as a cathode and an anode submerged in an alkaline electrolyte and connected by an external power supply. The main components of the electrochemical cell are the electrodes, the electrolyte, and the separator. A basic scheme of such a simple alkaline electrolysis cell is presented in Figure 2.4.

During electrolysis, a direct current (DC) is applied, and electrons flow into the cathode where hydrogen is produced on the surface. Hydroxide ions (OH^-) are produced on the cathode and transported through the electrolyte and the separator to the anode surface where oxygen is produced and OH^- is consumed[14].

The electrochemical half-reactions and cell reaction that take place in the electrolyser are presented below:

The minimum absolute reversible cell potential required for these reactions to take place is 1.23 V. However, due to irreversibilities present in the system, the required potential is higher[14]. The additional potential required is called the overpotential. This

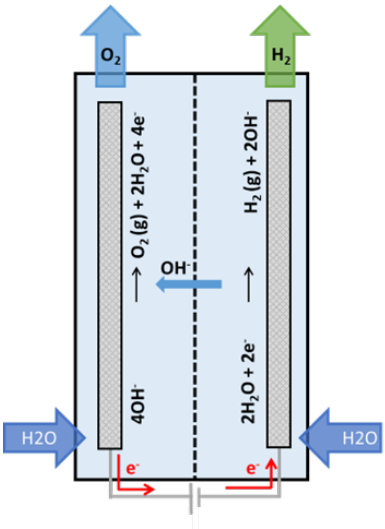

Figure 2.4: A schematic representation of a simple alkaline electrolysis cell.

Cathode	$2H_2O + 2e^- \longrightarrow H_2 + 2OH^-$	E^0 = -0.83 vs. SHE
Anode	$4OH^- \longrightarrow O_2 + 2H_2O + 4e^-$	E^0 = 0.40 vs. SHE
Overall	$2H_2O \longrightarrow 2H_2 + O_2$	E^0 = -1.23 V vs. SHE

overpotential typically includes multiple contributors, such as the activation overpotential, mass transfer overpotential, and overpotentials caused by ohmic resistances[15].

2.3.2. THERMODYNAMICS

Thermodynamically water is a stable molecule, therefore, water splitting is a thermodynamically unfavourable process. It is necessary to supply electrical energy to split water molecules into hydrogen and oxygen. The entropy is increased when converting liquid into two gases, and the enthalpy value of this conversion is very high[8].

The standard equilibrium cell potential (E^0_{cell}) is the minimum potential that must be applied to split water under standard conditions. The reversible cell potential, described in Equation 2.1, is defined as the difference of the equilibrium potential between the anode and the cathode[16].

$$E^0_{cell} = E^0_{cathode} - E^0_{anode} \tag{2.1}$$

At equilibrium the rate of the forward reaction is equal to the rate of the reverse reaction. In this case, there is no net reaction happening[17][18]. This equilibrium potential can be related to the Gibbs free energy through the following expression:

$$\Delta G = -nFE^0_{cell} \tag{2.2}$$

For a process to be spontaneous, or thermodynamically favoured, the Gibbs free energy must be smaller than zero. For alkaline water splitting, the equilibrium cell po-

tential is -1.23 V, therefore the minimum amount of energy that has to be provided is 237.3 kJ/mol. Since this value is larger than zero, the process is thermodynamically unfavourable.

In reality, the potential needed is higher. This is because of additional energy required in the form of heat. If the process is performed adiabatically, all the enthalpy required must be provided in the form of potential[16].

$$\Delta H_{cell} = \Delta G_{cell} + T * \Delta S_{cell} \tag{2.3}$$

$$\Delta H_{cell} = 237.3 + 48.3 = 285.6 kJ/mol$$

Consequently, the thermoneutral voltage that is needed to maintain the reaction without heat generation or absorption from the environment, using Equation 2.2:

$$E^0_{cell} = \frac{-\Delta H_{cell}}{nF} = \frac{-285.6 kJ/mol}{2 * 96485.3 C/mol} = -1.48 V$$

The cell potential is dependent on the operation temperature. Figure 2.5 shows the regimes depending on the applied potential and temperature. If the applied potential is lower than the equilibrium cell potential, hydrogen generation is impossible. If the potential is between the equilibrium potential and the thermoneutral potential the reaction occurs endothermically, and requires heat input from the environment. If the potential applied is higher than the thermoneutral potential heat is generated[16].

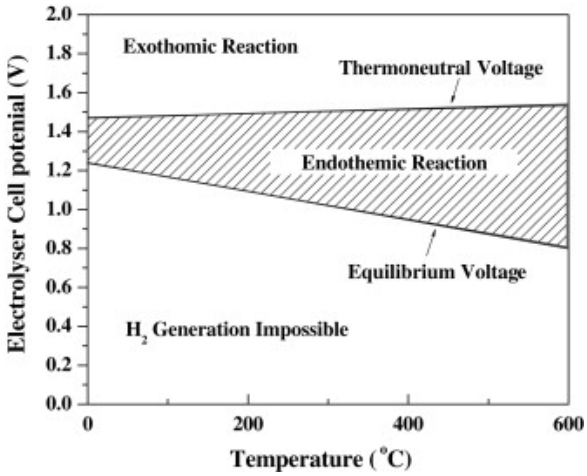

Figure 2.5: Operational regimes depending on the applied potential and temperature for hydrogen production [16].

2.3.3. KINETICS

The rate of the electrode reactions depend on the current density. This rate of reaction can be expressed as [18]

$$j = nFv \tag{2.4}$$

Where v is the rate of reaction and n the number of electrons transfered. For any chemical reaction, the rate constant can be expressed by the Arrhenius equation[16]

$$r = A * e^{\frac{-a_i}{RT}} \tag{2.5}$$

Electrochemical reaction kinetics can be described by the Butler-Volmer equation for one-step, one electron reactions[19][18]

$$j = j_0 * \left(e^{\frac{\alpha F \eta}{RT}} - e^{\frac{-\alpha F \eta}{RT}}\right) \tag{2.6}$$

At large overpotentials, the first term dominates and thus, the relationship between the current and the overpotential can be expressed as the Tafel equation[18].

$$\eta = a + log\, i \tag{2.7}$$

With the Tafel equation the rate of electrolysis can be expressed as a function of the current. Thus, it is possible to determine the kinetics of the reaction dependent on the current applied.

2.3.4. RESISTANCE AND LOSS MECHANISMS

Resistance can be classified into three main categories: electrical resistance, reaction resistance, and transport resistance. Transport resistances describe physical resistance. They include ionic transfer through the electrolyte and the membrane. Electrical resistances are calculated using Ohm's law. Heat is generated through both kinds of resistances[8]. The sum of all the resistances found in a typical water electrolysis system is given in Equation 2.8

$$R_{total} = R_{electric} + R_{anode} + R_{bubbleO_2} + R_{ions} + R_{membrane} + R_{bubbleH_2} + R_{cathode} \tag{2.8}$$

Where $R_{electric}$ refers to the external circuit resistances, namely the wiring and the connections. The overpotential resistances at both electrodes are denoted by R_{anode} and $R_{cathode}$. R_{bubble,O_2} and R_{bubble,H_2} regard the bubble resistances, due to the formation of O_2 and H_2 bubbles which cover the electrode surfaces partially. Finally, R_{ions} and $R_{membrane}$ refers to the resistance in the electrolyte and membrane[8].

Figure 2.6 describes the different contributions of overpotentials and resistances to the total cell potential in a typical alkaline water electrolyser.

2.3.5. ELECTROCATALYST MATERIALS

Through fundamental research, new electrocatalyst materials are constantly being developed both for the hydrogen evolution reaction (HER) and the oxygen evolution reaction (OER). However, OER has inherently higher overpotentials because it is a multiple electron transfer reaction, and usually the limiting factor of alkaline electrolysers systems[21].

The requirements for an electrocatalyst material, both anode and cathode include:

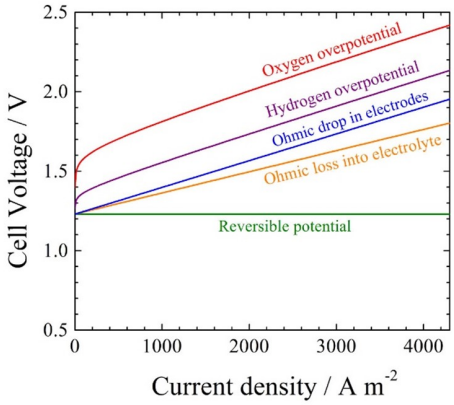

Figure 2.6: Distribution of cell voltage in alkaline water electrolysis [16] [20]

- Large active surface area
- High intrinsic activity of the material
- High chemical and electrochemical stability
- High electronic conductivity[22]

Although many simulations have been performed, most studies on new electrocatalyst materials are experimental[23]. A benchmarking study on the activity of different catalysts, both for OER and HER has been performed by McCrory et al.[24]. This includes both OER and HER catalysts in acidic and basic electrolytes. The activity is measured in overpotential at a given current density, in this case 10 mA/cm^2 The summary of the activity of various catalyst at said current density is included in Figure 2.7.

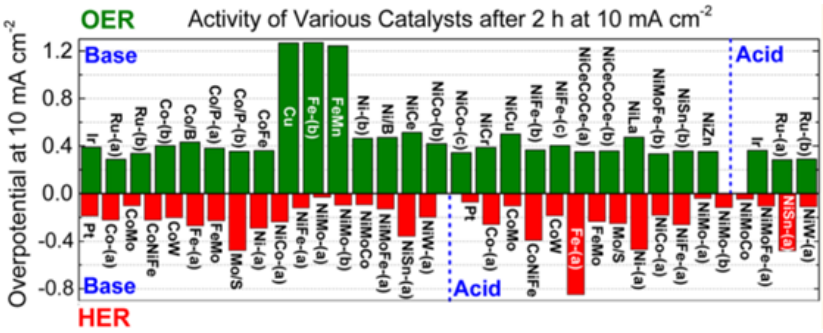

Figure 2.7: Overpotential in V at 10 mA/cm^2 for various catalysts in Acid and Base electrolytes[24].

2.3.6. CATHODE CATALYSTS

On the cathode surface in alkaline electrolysis, the hydrogen evolution reaction takes place. As mentioned previously, this reaction has been widely studied and as it consists of a two-electron transfer process. As such, hydrogen evolution reaction (HER) is the simplest electrochemical reaction, and can be described in 3 steps: adsorption, Volmer reaction, and finally desorption[23].

Many reviews have been published related to different HER catalysts[23][22][25]. Different additives and synthesis methods are used to optimize the active surface area and increase apparent activities.

Platinum is widely considered to be the most active electrocatalyst for hydrogen evolution in acidic media[24]. However, due to the availability and high costs of platinum, steel and nickel are widely used. Nickel is used widely because of its stability in alkaline media. Different additives are used to increase the exchange current density and improve synergistic effects from the different alloy phases. These include, but are not limited to Fe-Mo and Ni-Co[21].

Although Ni-based alloys exhibit high activity and stability, and are therefore widely used in alkaline media, it is not due to their intrinsic electrode activity, but mostly because of the large surface area in the catalyst surfaces[26]. An extensive table of the HER performance of common electrode materials, including the structure and activity compiled by Eftekhari[25] shows the wide variety of materials and alloys that have been studied. Some of the main HER electrocatalyst materials are presented in Table 2.1, including activity, stability and scale at which they have been used[27].

2.3.7. ANODE CATALYSTS

In contrast with the hydrogen evolution reaction, oxygen evolution is a highly complex reaction with multiple electron transfer processes. Because of the sluggish kinetics and 4 electron transfer processes involved, it is considered the limiting step for water evolution[29][30].

In alkaline conditions the reaction mechanism can be described as follows[29]:

$$
\begin{aligned}
OH^- + \cdot &\longrightarrow HO\cdot \\
HO\cdot + OH^- &\longrightarrow O\cdot + H_2O \\
O\cdot + OH^- &\longrightarrow HOO\cdot + e^- \\
HOO\cdot + OH^- &\longrightarrow \cdot + O_2 + H_2O
\end{aligned}
$$

Where $\cdot$ represents the active sites on the catalyst surface.

Traditionally, RuO_2 and IrO_2 are the reference OER catalysts in acidic environments. However, neither of them is thermodynamically ideal. RuO_2 binds oxygen too weakly (hindering the oxidation of $HO\cdot$), while IrO_2 binds oxygen too strongly (limiting the formation of $HOO\cdot$)[30].

Because of the relationship between binding energy of the catalyst material and the intermediates, an overpotential will always be required for a reaction transferring more than 2 electrons[30]. Therefore, many optimization processes have been studied to decrease the overpotential and increase the efficiency of the water splitting process. Transition metal based electrocatalysts are more stable in alkaline environments and more widely abundant than Ru and Ir[29].

Table 2.1: Main electrocatalyst materials and their current development [28]

Material	Activity	Stability	Status
Raney Ni	Sufficient activity	Deactivation after intermittent operation	Commercially used
Ni-Co, Ni-Fe	High activity, which can be further improved upon alloying with rare earth metals	Better stability than Raney Ni, but still not optimal	Laboratory applications
$NiFe_2O_4$	Very high activity	Long term stability	Applied in lab-scale electrolysis with polymeric membrane
Ni-Mo	Very high activity	Long term stability	Pyrophoric material: inappropriate for commercialization
(Ni,Co)-W	High activity	Unknown	Laboratory applications
Co_2Si	Very high activity	Unknown	Laboratory applications
Ni_3N	High activity	Unknown	Laboratory applications

An extensive review on transition metal based electrocatalysts has been published by Lu et al. [29]. Other studies include future directions in the OER research field, including better understanding of the mechanistic pathways to develop simulations that accurately describe the reaction intermediates[31]. Modeling the intermediate binding energies could provide pathways to new catalyst material development. The search for a stable, active, and abundant electrocatalyst is still ongoing for the further development of large-scale hydrogen production.

2.3.8. CATALYST SURFACE

Although active surface area plays a significant role in electrocatalysis, it is still complex to decouple the effect of surface area and intrinsic catalyst activity[26]. As surface area can have such a large effect on the catalyst activity of the material, electrode production processes are important. Due to this, electrocatalyst material choice or selection is not the only important parameter in catalyst development. Specific surface area and roughness play a role in catalyst activity[32]. There are numerous research works focus on production methods that result in larger surface areas and decrease of the overpotentials. Because of the large effect the electrochemically active surface area has on the current density, it is often difficult to compare different catalysts[24].

2.3.9. ELECTROLYTE

Highly concentrated KOH and NaOH electrolytes are used, which gives origin to the name of alkaline electrolysis. The main disadvantage is that these solutions are highly corrosive, and some additives are used to counteract the corrosive nature[28][21]. Leakage is a major issue in alkaline electrolytes, but advantages include the high conductivity of the solution[28].

As seen in Figure 2.8, the conductivity is dependent on the concentration and temperature and can therefore be optimized to reduce ohmic overpotentials in the electrolyte gap. Using the empirical calculation proposed by Gilliam et al.[33] the highest specific conductivity is around 6 M. Increasing temperature compared to ambient is advantageous for the conductivity of the solution.

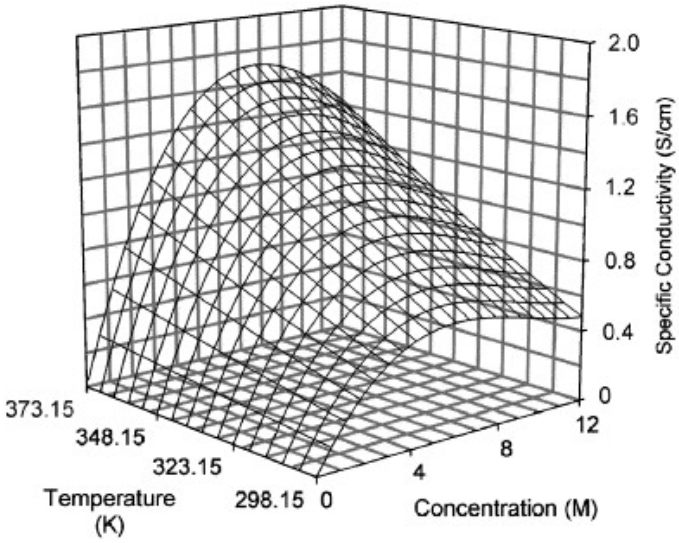

Figure 2.8: 3D plot of specific conductivity of KOH with respect to temperature and concentration calculated with an empirical correlation proposed by Gilliam et al.[33].

In commercial scale alkaline electrolysis the addition of alkali metal cations is not usual. It has been reported that different cations have catalytic effects on the overpotentials of oxygen evolution[34]. Garcia et al. postulate the effect of cations present in the electrolyte, leading to a stabilization of the precursor to O_2 evolution[35]. Adding other alkali metal cations into the electrolyte can affect the conductivity of the electrolyte, and therefore can be unfavorable.

Other contaminants in the electrolyte can affect the OER potential and thus affect the catalytic activity. Iron content in the electrolyte has a significant catalytic effect on the OER activity[35]. The effect of cations in the electrolyte is further discussed in Chapter 4 of this thesis.

2.3.10. EFFICIENCY

System energy efficiencies of commercial electrolysers plants typically range from 60 to 73%[36]. System energy efficiency is calculated as the ratio between the energy content of the produced hydrogen, using the LHV, and the electric energy consumed for electrolysis plus the electric energy required to run the auxiliary equipment.

Some of the conditions that can minimize the required voltage include the modification of the electrode materials, the reduction of the distance between the electrodes, the maximization of the electrolyte conductivity, and the selection of an appropriate separator[37]. New developments are being researched to obtain larger energy efficiencies.

2.3.11. NEW DEVELOPMENTS

The most important development points in alkaline electrolysers during the recent decades include:

- Zero-gap configuration to reduce the ohmic losses due to the electrolyte gap[38][39][40][41].
- New diaphragm materials such as porous composites composed of a polysulfone matrix and ZrO_2 (Zirfon)[42]
- Temperature increases to increase conductivity and improve reaction kinetics[28].
- New developments in electrocatalysts reduce overpotentials at the electrodes[30]

New developments focus on increasing the efficiency of alkaline electrolysis. Therefore the focus is on addressing the greatest losses in efficiency, which according to Zouhri and Lee[43], are due to:

1. Hydrogen bubbles on the surface
2. Ionic resistivity of the electrolyte
3. Oxygen bubbles on the anode surface
4. Electrode distance
5. Membrane resistivity[28]

To limit bubble overpotentials, some methods to avoid bubble formation include magnetic ultrasonic, super gravity field, and zero gap configuration [21].

Most developments aim to reduce the cost of hydrogen production. To reduce construction costs, one possible solution is to increase operational current densities. Therefore it is important to limit the overpotentials required to increase efficiency[28]

2.4. NICKEL-IRON BATTERIES

Batteries can be divided into 2 main categories: primary and secondary batteries. Primary batteries apply irreversible electrochemical reactions, and thus can only be used once [44]. Secondary batteries can be recharged by applying a larger voltage to make the current run in the opposite direction, therefore also known as rechargeable batteries[45]. The nickel-iron battery is a secondary battery developed by Edison in 1901. Although successfully developed and commercialized in the 20th century, Lead Acid batteries won a larger market share due to their lower costs[46]. However, Ni-Fe batteries have resurfaced recently due to their long cycle lives and robust nature. They consist of a nickel hydroxide positive electrode and an iron hydroxide negative electrode[47] with an open circuit cell potential of 1.37 V. A schematic representation of a nickel iron battery is presented in Figure 2.9.

Similarly to the alkaline electrolyser, a battery system can be described as two electrodes connected by an ionic conductor called an electrolyte. When the electrodes are connected by an external circuit, electrons flow spontaneously from the more negative electrode to the more positive potential electrode. Ions are transported through the electrolyte to complete the circuit[45].

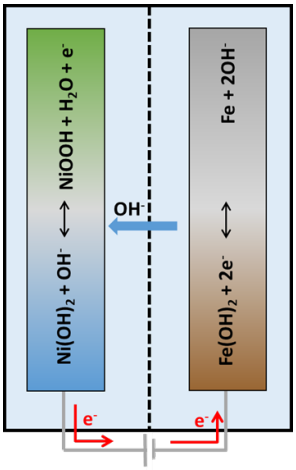

Figure 2.9: Schematic representation of a Nickel-Iron battery and the charging/discharging reactions.

The Ni/Fe battery is very robust and can withstand vibrations, mechanical shock, overcharge and overdischarge[48]. The limited use of critical raw materials is environmentally beneficial and has renewed the interest in this particular battery composition[46]. However, its round trip efficiency is around 50%[48]. This is mainly due to water splitting during charging and high self-discharge rates. The cause of these high self-discharge rates is the low overpotential for hydrogen evolution on the iron electrode and the proximity of the potential of the iron electrode and the hydrogen evolution reaction[48]. A disadvantage for mobile applications is their relatively low specific energy density (30-50 Wh/kg)[46]. However, they could potentially be a cost-effective solution for large-scale stationary energy storage solutions, where weight is not a concern.

Due to the proximity of the potentials for charging of the iron electrode and HER, during and after charging, hydrogen is evolved on the iron electrode. Therefore, the main focus of research on Ni/Fe batteries in the past has been to suppress the hydrogen evolution reaction. Suppression of oxygen evolution on the nickel electrode has also been addressed by lowering the equilibrium charge potential by doping the hydroxide with Co, and thus increasing the distance to the OER potential[48].

2.4.1. FUNDAMENTALS

During discharge, the reaction of this battery can be expressed as:

$$2\,\mathrm{NiOOH} + \mathrm{Fe} + 2\,\mathrm{H_2O} \longrightarrow 2\,\mathrm{Ni(OH)_2} + \mathrm{Fe(OH)_2} \tag{2.9}$$

At deep discharge rates, the iron electrode can undergo further discharge.

$$\mathrm{NiOOH} + \mathrm{Fe(OH)_2} \longrightarrow \mathrm{Ni(OH)_2} + \mathrm{FeOOH} \tag{2.10}$$

The first reaction is highly reversible. However, the second oxidation step of $Fe(OH)_2$ results in damage to the battery life[47]. Typically, cells include an excess of iron electrodes in order to eliminate the chance of $Fe(OH)_2$ oxidation[48][49].

The electrodes are placed in a 30 wt.% KOH solution, which provides the necessary conductivity for the ionic current. Typically 50 g/L of LiOH is added to improve the capacity of the positive nickel electrode. Although this is common practice, the reason why the lifetime of the electrode increases with LiOH additions is not understood. The chemical reaction can be expressed as two half reactions, each one pertaining to one electrode.

The half reactions, for battery discharging, can be presented as follows:

Positive electrode	$\mathrm{NiOOH} + \mathrm{H_2O} + \mathrm{e^-} \longrightarrow \mathrm{Ni(OH)_2} + \mathrm{OH^-}$	E^0 = 0.53 vs. SHE
Negative electrode	$\mathrm{Fe} + 2\,\mathrm{OH^-} \longrightarrow \mathrm{Fe(OH)_2} + 2\,\mathrm{e^-}$	E^0 = -0.87 vs. SHE
Overall	$2\,\mathrm{NiOOH} + \mathrm{Fe} \longrightarrow 2\,\mathrm{Ni(OH)_2} + \mathrm{Fe(OH)_2}$	E^0 = 1.4 V vs. SHE

Figure 2.10 shows the voltage characteristics for a typical nickel/iron battery at constant current. A discharge curve is followed by a charging curve at constant current.

2.4.2. ELECTROLYTE

Nickel iron batteries use an aqueous electrolyte consisting of highly concentrated KOH. As mentioned in the previous section, cobalt is used to dope the iron electrode to increase the overpotential of OER and thus prevent water splitting of the aqueous electrolyte[48]. LiOH is added to increase the lifetime of the battery, although it is not clear why this happens[34][50]. Additionally, potassium sulfide[46] increases the performance of the NiFe cells by increasing the coulombic efficiency[51]. Other known additives used to increase battery lifetime include wetting agents[52], long chain thiols[53], and organic acids[54].

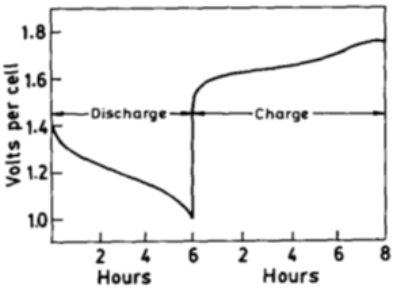

Figure 2.10: Charge and discharge curves of a typical Ni-Fe battery- voltage characteristics at constant current charge/discharge [47]

2.4.3. ADVANTAGES

Nickel-iron batteries are among the cheapest batteries available[55]. Furthermore, they have 1.5-2 times the specific energy of typical lead/acid batteries[56]. The calendar life of nickel/iron batteries is approximately 20 years, or in the order of 3000 cycles. This includes abusive usage, such as deep discharge between cycles[47]. Although they are cheap and robust, they are not commonly used because of the catalytic activity of iron and nickel for respectively hydrogen and oxygen evolution production which results in water splitting during charging and a high self-discharge rate[56]. The daily self-discharge is approximately 1 to 2% of the nominal capacity at ±25°C, but can be as high as 10% at ±40°C[48]. Because of this limiting factor, they can only be used in applications where they are cycled often, normally in periods shorter than 48 hours[47].

2.5. AN INTEGRATED NI-FE BATTERY AND ELECTROLYSER- THE BATTOLYSER

According to the International Renewable Energy Agency (IRENA) stationary applications of battery storage is poised to grow 17-fold by 2030[35]. As renewable energy capacity grows, greater flexibility is needed. By providing different time-scales of storage, this can drive a further decarbonisation of the electrical grid[35].

The main idea of the battolyser prototype is for it to integrate the need for both long-term and short-term storage requirements. This has been achieved by the combination of an Edison battery with an alkaline electrolyser. In this way, the battery capacity can be used to mitigate daily variations in renewable energy generation, while the alkaline electrolyser will convert the additional electricity into hydrogen. Hydrogen can be subsequently stored for future use in a fuel cell[36].

The main processes in the battolyser are indicated in Figure 2.11.

This device is made from a modified Ni-Fe battery. The electrodes are manufactured from nanostructured NiOOH and reduced Fe. Therefore, when the battery is fully charged, the Fe acts as a HER catalyst, while the NiOOH acts as an OER catalyst [57].

The capacity limit of this system is not a fixed characteristic of the battery material. Excess electricity can be used to produce hydrogen. Furthermore, Ni-Fe batteries are

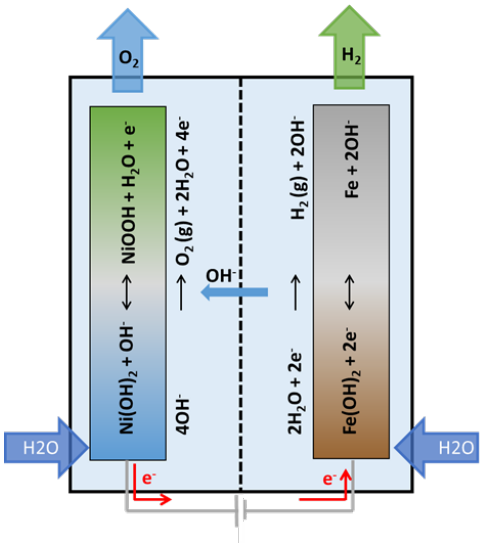

Figure 2.11: Schematic representation of the battolyser operation during charging and electrolysis.

very robust and have a lifetime of approximately 3000 cycles [47]. The total faradaic efficiency of the battery and hydrogen production is close to 100% [57]. Moreover, the device can follow electricity fluctuations typical of renewable energies, such as solar and wind[57].

The energy efficiency is calculated as the amount of electricity available when the battery is discharged plus the energetic content of the hydrogen produced divided by the electric energy required to charge and perform electrolysis[57].

Currently the battolyser prototype is being scaled up and commercialized as a proof-of-concept. As mentioned on their website[58], a pilot plant will be installed at the Vattenfall Magnum power plant at the Eemshaven in The Netherlands. This consists of a pressurized cell stack of 15 kWh with appropriate Balance of Plant and power electronics. The next phase for the commercial demonstration of the technology is planned to be at MWh scale at the clean tech campus 'The Green Box' in Hengelo in The Netherlands.

BIBLIOGRAPHY

[1] *Energy storage technologies*, Aug. 2015. [Online]. Available: https://ease-storage.eu/energy-storage/technologies/.

[2] D. Sprake, Y. Vagapov, S. Lupin, and A. Anuchin, "Housing estate energy storage feasibility for a 2050 scenario", in *2017 Internet Technologies and Applications (ITA)*, IEEE, 2017, pp. 137–142.

[3] D. Akinyele and R. Rayudu, "Review of energy storage technologies for sustainable power networks", *Sustainable energy technologies and assessments*, vol. 8, pp. 74–91, 2014.

[4] I. Hadjipaschalis, A. Poullikkas, and V. Efthimiou, "Overview of current and future energy storage technologies for electric power applications", *Renewable and sustainable energy reviews*, vol. 13, no. 6-7, pp. 1513–1522, 2009.

[5] M. M. Rahman, A. O. Oni, E. Gemechu, and A. Kumar, "Assessment of energy storage technologies: A review", *Energy Conversion and Management*, vol. 223, p. 113 295, 2020.

[6] J. Elio, P. Phelan, R. Villalobos, and R. J. Milcarek, "A review of energy storage technologies for demand-side management in industrial facilities", *Journal of Cleaner Production*, vol. 307, p. 127 322, 2021.

[7] S. Hameer and J. L. van Niekerk, "A review of large-scale electrical energy storage", *International journal of energy research*, vol. 39, no. 9, pp. 1179–1195, 2015.

[8] D. M. Santos, C. A. Sequeira, and J. L. Figueiredo, "Hydrogen production by alkaline water electrolysis", *Quımica Nova*, vol. 36, pp. 1176–1193, 2013.

[9] S. Venkata Mohan and A. Pandey, "Chapter 1 - sustainable hydrogen production: An introduction", in *Biohydrogen (Second Edition)*, A. Pandey, S. V. Mohan, J.-S. Chang, P. C. Hallenbeck, and C. Larroche, Eds., Second Edition, Elsevier, 2019, pp. 1–23, ISBN: 978-0-444-64203-5. DOI: https://doi.org/10.1016/B978-0-444-64203-5.00001-0. [Online]. Available: https://www.sciencedirect.com/science/article/pii/B9780444642035000010.

[10] S. P. Badwal, S. S. Giddey, C. Munnings, A. I. Bhatt, and A. F. Hollenkamp, "Emerging electrochemical energy conversion and storage technologies", *Frontiers in chemistry*, vol. 2, p. 79, 2014.

[11] T. Smolinka, H. Bergmann, J. Garche, and M. Kusnezoff, "The history of water electrolysis from its beginnings to the present", in *Electrochemical Power Sources: Fundamentals, Systems, and Applications*, Elsevier, 2022, pp. 83–164.

[12] E. Zoulias, E. Varkaraki, N. Lymberopoulos, C. N. Christodoulou, and G. N. Karagiorgis, "A review on water electrolysis", *Tcjst*, vol. 4, no. 2, pp. 41–71, 2004.

[13] P. Millet, S. Grigoriev, and L. Diéguez, "Renewable hydrogen technologies", *Production, Purification, Storage, Applications and Safety*, pp. 19–40, 2013.

[14] A. J. Bard, L. R. Faulkner, and H. S. White, *Electrochemical methods: fundamentals and applications*. John Wiley & Sons, 2022.

[15] A. Demirbas, "Green energy and technology", in 2010, pp. 139–157, ISBN: 978-1-84882-720-2. DOI: 10.1007/978-1-84996-050-2_6.

[16] K. Zeng and D. Zhang, "Recent progress in alkaline water electrolysis for hydrogen production and applications", English, *Progress in Energy and Combustion Science*, vol. 36, pp. 307–326, 2010, ISSN: 0360-1285. DOI: 10.1016/j.pecs.2009.11.002.

[17] V. S. Bagotsky, *Electrochemical methods: fundamentals and applications*. John Wiley & Sons, 2005.

[18] S. Marini, P. Salvi, P. Nelli, *et al.*, "Advanced alkaline water electrolysis", *Electrochimica Acta*, vol. 82, pp. 384–391, 2012.

[19] M. Berrettoni, "Advanced alkaline water electrolysis", *Electrochimica Acta*, vol. 82, pp. 384–391, 2012.

[20] EPFL. "Alkaline electrolyser@ONLINE". (2021), [Online]. Available: https://www.epfl.ch/labs/lepa/grid2mobility-demonstrator-martigny/key-technologies/alkaline-electrolyser/.

[21] M. Bodner, A. Hofer, and V. Hacker, "H2 generation from alkaline electrolyzer", *Wiley Interdisciplinary Reviews: Energy and Environment*, vol. 4, no. 4, pp. 365–381, 2015.

[22] M. A. Khan, H. Zhao, W. Zou, *et al.*, "Recent progresses in electrocatalysts for water electrolysis", *Electrochemical Energy Reviews*, vol. 1, no. 4, pp. 483–530, 2018.

[23] A. Lasia, "Mechanism and kinetics of the hydrogen evolution reaction", *international journal of hydrogen energy*, vol. 44, no. 36, pp. 19 484–19 518, 2019.

[24] C. C. McCrory, S. Jung, I. M. Ferrer, S. M. Chatman, J. C. Peters, and T. F. Jaramillo, "Benchmarking hydrogen evolving reaction and oxygen evolving reaction electrocatalysts for solar water splitting devices", *Journal of the American Chemical Society*, vol. 137, no. 13, pp. 4347–4357, 2015.

[25] A. Eftekhari, "Electrocatalysts for hydrogen evolution reaction", *International Journal of Hydrogen Energy*, vol. 42, no. 16, pp. 11 053–11 077, 2017.

[26] L. Birry and A. Lasia, "Studies of the hydrogen evolution reaction on raney nickel—molybdenum electrodes", *Journal of applied electrochemistry*, vol. 34, no. 7, pp. 735–749, 2004.

[27] F. M. Sapountzi, J. M. Gracia, H. O. Fredriksson, J. H. Niemantsverdriet, *et al.*, "Electrocatalysts for the generation of hydrogen, oxygen and synthesis gas", *Progress in Energy and Combustion Science*, vol. 58, pp. 1–35, 2017.

[28] M. David, C. Ocampo-Martınez, and R. Sánchez-Peña, "Advances in alkaline water electrolyzers: A review", *Journal of Energy Storage*, vol. 23, pp. 392–403, 2019.

[29] F. Lu, M. Zhou, Y. Zhou, and X. Zeng, "First-row transition metal based catalysts for the oxygen evolution reaction under alkaline conditions: Basic principles and recent advances", *Small*, vol. 13, no. 45, p. 1 701 931, 2017.

[30] M. T. Koper, "Thermodynamic theory of multi-electron transfer reactions: Implications for electrocatalysis", *Journal of Electroanalytical Chemistry*, vol. 660, no. 2, pp. 254–260, 2011.

[31] X. Kong and Z. Peng, "Low-dimensional materials for alkaline oxygen evolution electrocatalysis", *Materials today chemistry*, vol. 11, pp. 119–132, 2019.

[32] S. Sun, H. Li, and Z. J. Xu, "Impact of surface area in evaluation of catalyst activity", *Joule*, vol. 2, no. 6, pp. 1024–1027, 2018.

[33] R. Gilliam, J. Graydon, D. Kirk, and S. Thorpe, "A review of specific conductivities of potassium hydroxide solutions for various concentrations and temperatures", *International Journal of Hydrogen Energy*, vol. 32, no. 3, pp. 359–364, 2007.

[34] B. Reddy and D. Linden, *Handbook of Batteries*. McGraw-Hill, 2002.

[35] A. C. Garcia, T. Touzalin, C. Nieuwland, N. Perini, and M. T. Koper, "Enhancement of oxygen evolution activity of nickel oxyhydroxide by electrolyte alkali cations", *Angewandte Chemie International Edition*, vol. 58, no. 37, pp. 12 999–13 003, 2019.

[36] J. Silveira, *Sustainable Hydrogen Prodution Processes*. Feb. 2017, ISBN: 978-3-319-41614-4. DOI: 10.1007/978-3-319-41616-8.

[37] F. Goodridge and K. Scott, *Electrochemical process engineering: a guide to the design of electrolytic plant*. Springer Science & Business Media, 2013.

[38] R. Phillips, A. Edwards, B. Rome, D. R. Jones, and C. W. Dunnill, "Minimising the ohmic resistance of an alkaline electrolysis cell through effective cell design", *International Journal of Hydrogen Energy*, vol. 42, no. 38, pp. 23 986–23 994, 2017.

[39] D. Pletcher and X. Li, "Prospects for alkaline zero gap water electrolysers for hydrogen production", *International Journal of Hydrogen Energy*, vol. 36, no. 23, pp. 15 089–15 104, 2011.

[40] J. Haverkort and H. Rajaei, "Voltage losses in zero-gap alkaline water electrolysis", *Journal of Power Sources*, vol. 497, p. 229 864, 2021.

[41] M. T. de Groot and A. W. Vreman, "Ohmic resistance in zero gap alkaline electrolysis with a zirfon diaphragm", *Electrochimica Acta*, vol. 369, p. 137 684, 2021.

[42] P. Vermeiren, W. Adriansens, J. Moreels, and R. Leysen, "Evaluation of the zirfon® separator for use in alkaline water electrolysis and Ni-H2 batteries", *International Journal of Hydrogen Energy*, vol. 23, no. 5, pp. 321–324, 1998, ISSN: 0360-3199. DOI: https://doi.org/10.1016/S0360-3199(97)00069-4. [Online]. Available: https://www.sciencedirect.com/science/article/pii/S0360319997000694.

[43] K. Zouhri and S.-y. Lee, "Evaluation and optimization of the alkaline water electrolysis ohmic polarization: Exergy study", *International Journal of Hydrogen Energy*, vol. 41, no. 18, pp. 7253–7263, 2016.

[44] R. Huggins, *Advanced batteries: materials science aspects*. Springer Science & Business Media, 2008.

[45] M. Armand and J.-M. Tarascon, "Building better batteries", *Nature*, vol. 451, pp. 652–7, Mar. 2008. DOI: 10.1038/451652a.

[46] J. O. G. Posada, A. J. Rennie, S. P. Villar, *et al.*, "Aqueous batteries as grid scale energy storage solutions", *Renewable and Sustainable Energy Reviews*, vol. 68, pp. 1174–1182, 2017.

[47] A. Shukla, M. Ravikumar, and T. Balasubramanian, "Nickel/iron batteries", *Journal of power sources*, vol. 51, no. 1-2, pp. 29–36, 1994.

[48] C. Chakkaravarthy, P. Periasamy, S. Jegannathan, and K. Vasu, "The nickel/iron battery", *Journal of power sources*, vol. 35, no. 1, pp. 21–35, 1991.

[49] S. U. Falk and A. J. Salkind, "Alkaline storage batteries", 1969.

[50] B. Hariprakash, S. Martha, M. Hegde, and A. Shukla, "A sealed, starved-electrolyte nickel–iron battery", *Journal of Applied Electrochemistry*, vol. 35, no. 1, pp. 27–32, 2005.

[51] J. O. G. Posada, A. H. Abdalla, C. I. Oseghale, and P. J. Hall, "Multiple regression analysis in the development of Ni-Fe cells as energy storage solutions for intermittent power sources such as wind or solar", *international journal of hydrogen energy*, vol. 41, no. 37, pp. 16 330–16 337, 2016.

[52] A. K. Manohar, C. Yang, S. Malkhandi, G. S. Prakash, and S. Narayanan, "Enhancing the performance of the rechargeable iron electrode in alkaline batteries with bismuth oxide and iron sulfide additives", *Journal of the Electrochemical Society*, vol. 160, no. 11, A2078, 2013.

[53] S. Malkhandi, B. Yang, A. K. Manohar, G. S. Prakash, and S. Narayanan, "Self-assembled monolayers of n-alkanethiols suppress hydrogen evolution and increase the efficiency of rechargeable iron battery electrodes", *Journal of the American Chemical Society*, vol. 135, no. 1, pp. 347–353, 2013.

[54] J. O. G. Posada and P. J. Hall, "The effect of electrolyte additives on the performance of iron based anodes for Ni-Fe cells", *Journal of The Electrochemical Society*, vol. 162, no. 10, A2036, 2015.

[55] T. R. Cook, D. K. Dogutan, S. Y. Reece, Y. Surendranath, T. S. Teets, and D. G. Nocera, "Solar energy supply and storage for the legacy and nonlegacy worlds", *Chem. Rev*, vol. 110, pp. 6474–6502, 2010.

[56] R. Dell, "Batteries: Fifty years of materials development", *Solid State Ionics*, vol. 134, no. 1-2, pp. 139–158, 2000.

[57] F. Mulder, B. Weninger, J. Middelkoop, F. Ooms, and H. Schreuders, "Efficient electricity storage with a battolyser, an integrated Ni-Fe battery and electrolyser", *Energy & Environmental Science*, vol. 10, no. 3, pp. 756–764, 2017.

[58] "Battolyser systems". (2022), [Online]. Available: https://www.battolysersystems.com/.

3

Modeling the Performance of an Integrated Battery and Electrolyzer System

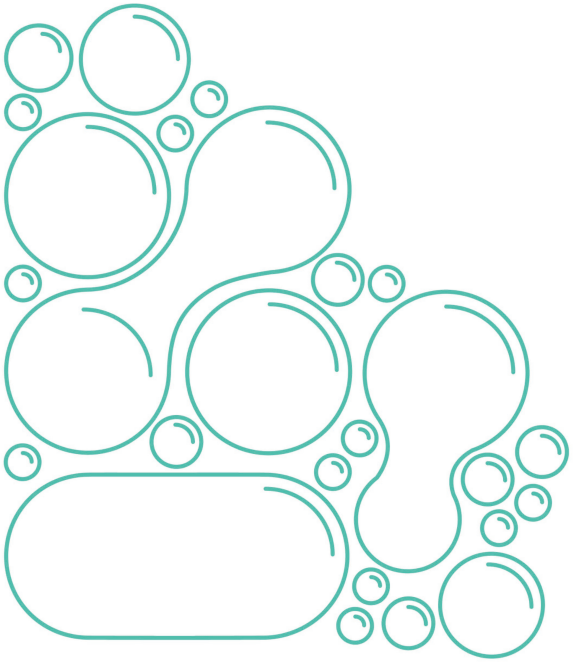

Both daily and seasonal fluctuations of renewable power sources will require large-scale energy storage technologies. A recently developed integrated battery and electrolyser system, called battolyser, fulfills both time-scale requirements. Here, we develop a macroscopic COMSOL Multiphysics model to quantify the energetic efficiency of the battolyser prototype that, for the first time, integrates the functionality of a nickel iron battery and an alkaline electrolyser. The current prototype has a rated capacity of 5 Ah, and to develop a larger, enhanced system it is necessary to characterize the processes occurring within the battolyser and to optimize the individual components of the battolyser. Therefore, there is a need for a model that can provide a fast screening on how the properties of individual components influence the overall energy efficiency of the battolyser prototype. The model is validated using experimental results, and new configurations are compared and the energy efficiency optimized for the scale-up of this lab-scale device. Based on the modeling work, we find an optimum electrode thickness for the nickel electrode of 3 mm and 2.25 mm for the iron electrode with optimal electrode porosities range of void fraction of 0.15 - 0.35. Additionally, electrolyte conductivity and the gap thickness are found to have a small effect on the overall efficiency of the device.

This chapter has been published in Ind. Eng. Chem. Res. 2021, 60, 30, 10988–10996

3.1. INTRODUCTION

THE increasing share of wind and solar energy, together with COP21 Paris targets set for renewable energy capacity growth, imply an increase in the variability of future electricity generation[1][2]. Therefore, an electrical grid completely based on largely intermittent renewable energy sources will require widespread and efficient energy storage[3][4]. Currently, fossil fuels provide the buffer capacity necessary to balance this mismatch between energy supply and demand[1][5]. As the capacity of renewable energy increases and fossil fuel use decreases, energy storage technologies will be key for developing grids with higher flexibility and the large-scale utilization of renewable energy sources[6][7].

Batteries are a good option to cover short-term grid fluctuations because of their dynamics and high round-trip efficiency, typically around 80%[8][9]. However, due to their cost, limited cycling rate, self-discharge, and low specific energy storage capacity (energy stored per unit mass), large-scale, longer-term storage options are required alongside battery capacity[7][8]. An alternative solution for long-term energy storage is the production of fuels using renewable energy. Hydrogen is an example of such a fuel that can either be burned in a gas-fired internal combustion engine, gas turbine or electrochemically converted in a fuel cell to generate electricity. The advantages of using hydrogen as an energy carrier include it being a carbon free fuel with a high mass specific energy density[8][10][11]. Besides being a fuel, hydrogen is also used as feedstock in the chemical industry, as well as in the refining, food industry, metallurgical, and electronic industry[12].

An integrated battery and electrolyser device, known as the battolyser, has recently been developed[6]. The battolyser was demonstrated as a possible energy storage solution, as its battery functionality can stabilize short-term electricity fluctuations while its electrolyser functionality can stabilize long-term seasonal fluctuations[6][13]. Furthermore, the device was shown to be stable for more than 300 cycles[13]. As can be seen in Figure 3.1, the battolyser utilizes two different energy storage functionalities: a nickel-iron battery and an alkaline electrolyser. The nickel-iron battery, also known as the Edison battery, serves as a short-term energy storage mechanism[14]. Electricity can be stored and generated from the materials in the electrodes via the $NiOH_2$ /NiOOH and $Fe(OH)_2$ /Fe redox couples[15]. When the maximum battery capacity is reached, the battolyser makes use of the electrocatalytic properties of Fe and NiOOH for electrochemical hydrogen and oxygen evolution and the device then acts as an alkaline electrolyser. Thereby, the excess electricity that cannot be stored in the battery functionality is used to split water molecules from the electrolyte, generating hydrogen and oxygen[14][15].

Since the system operates as both a battery and electrolyser, the capacity limit of this system is not fixed by the amount of the active battery material. An additional advantage of using Ni-Fe batteries in the system is that they are very robust and have a life time of approximately 3000 cycles, or 20 years[13][16]. The total energy efficiency of the system, combining battery functionality and hydrogen production, is around 90%[13]. Moreover, the device can follow electricity fluctuations typical of renewable energies, such as solar and wind[13].

Here, we report on the development of a macroscopic model that can quantify the energy efficiency of the existing battolyser prototype. The current battolyser prototype

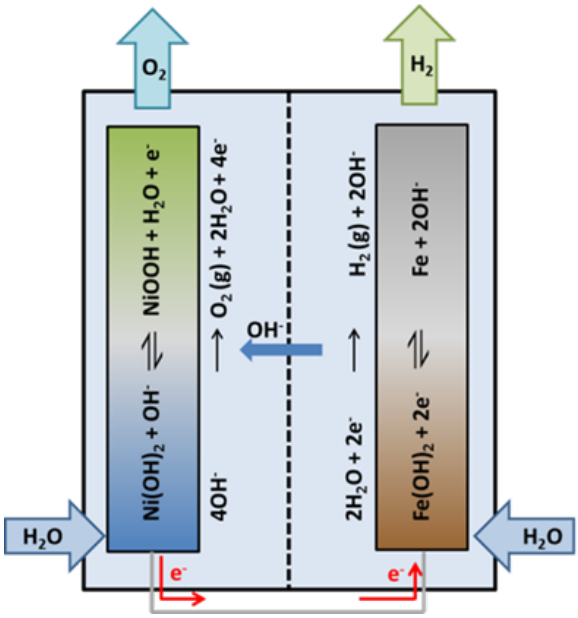

Figure 3.1: Schematic illustration of the chemical reactions that occur during charging, overcharging, and discharging of the battolyser.

has a rated capacity of 5 Ah, and to develop a larger, more optimized system it is necessary to characterize the processes occurring within the battolyser and to optimize the individual components of the battolyser. Therefore, there is a need for a model that can provide a fast screening on how the properties of individual components influence the overall energy efficiency of the battolyser prototype.

Many empirical and semi-empirical models have been proposed to simulate alkaline electrolysis[17][18], however our approach integrates thermodynamics, kinetics, and transport mechanisms to model the performance of the integrated storage device including details of the specific geometry. Furthermore, only a handful models of alkaline electrolysis have been validated experimentally[19]. Many models simulate the I-V characteristics of different electrochemical cells, however, not many can determine the effect of the geometric cell parameters on the functionality[17][19][20]. The model developed here is validated using experimental results, and new configurations and design parameters have been compared and optimized for the upscaling of this lab-scale device. The model developed is able to predict the energy efficiency of different configurations without having to test these configurations individually, which is of utmost importance in upscaling the current battolyser prototype. In addition, the developed model is to the best of our knowledge the first model that integrates a battery and electrolyser functionality for Nickel Iron batteries. A comprehensive model for Zinc Nickel batteries has been recently published[21]. Using the model, we will give design recommendations that can improve the device efficiency, taking into account both the battery and electrolyser functionality and the trade-offs inherent for the optimization. Some of the limitations of the

current model include bubble production and thermal effects, and future efforts can be made to study these effects.

3.2. MODELING AND EXPERIMENTAL METHODS

3.2.1. MODEL

A 1D COMSOL Multiphysics model has been developed to simulate the integration of battery and electrolyser functionalities of the battolyser system. The COMSOL Multiphysics model is a time-dependent partial differential equation system using a Backward Differentiation Formula (BDF) solver with variable size up to extremely fine finite elements. This tool was chosen to solve the governing physical equations detailed here. To describe the integration of both storage functionalities a number of aspects must be taken into account, including:

- the diffusion of hydroxide ions from one electrode to another and the concentration profiles of hydroxide and potassium ions through the width of the cell,
- the calculation of the cell potential, including the overpotential of each chemical reaction,
- the electrochemical reactions for the battery functionality including the nickel positive electrode and the iron negative electrode reactions and the determination of the state of charge of the battery,
- the electrochemical reactions for the electrolyser functionality including the hydrogen evolution reaction (HER) and oxygen evolution reaction (OER),
- the bubble production.

These phenomena are all quantified for different time scales, therefore building a time-dependent model that simulates both battery and electrolyser functionalities in the x dimension of the battolyser cell.

The COMSOL Multiphysics model is a time-dependent partial differential equation system using a Backward Differentiation Formula (BDF) solver with variable size extremely fine finite elements. A schematic representation of the electrochemical cell is presented in Figure 3.2. The cell is composed of an iron negative electrode, a nickel positive electrode (both from Ironcore) and a polyphenylene sulphide fabric commercial separator (Zirfon PERL, AGFA). All three components are porous and considered to be filled with aqueous liquid 5 M KOH electrolyte. A cross-section of the battolyser is modeled in one dimension. Thereby, length and height effects are neglected. The average particle diameter is considered for solid diffusion. The model includes effects of the electronic current conduction in the electrodes and ionic charge transport through the electrodes, electrolyte, and separator.

This model simulates mass transport in the electrolyte and within the particles that form the electrodes. A similar model was developed by Newman and Paxton to describe NiMH batteries. A similar approach is taken, but secondary reactions are included to take into account HER/OER production. The reaction source term includes

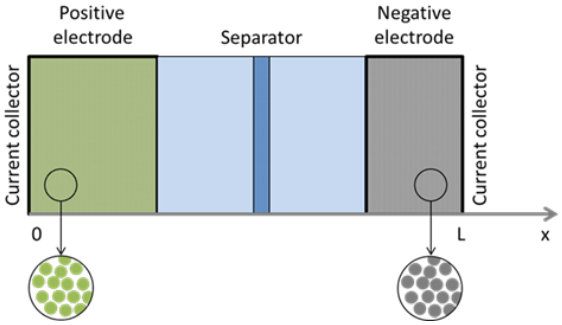

Figure 3.2: Schematic diagram of battolyser cells and their model representation including the Ni(OH)2 positive electrode, aqueous KOH electrolyte, polyphenylene sulphide separator and Fe(OH)2 negative electrode.

Butler-Volmer kinetics, both for the charging/discharging reactions and the gas production reactions. All the simulations are considered at ambient temperature and pressure. Thermal effects are not considered as the current density is relatively low compared to industrial electrolyser systems. Therefore, thermal effects due to high current density effects are assumed to be negligible. Pressure effects are not considered as the system operates under atmospheric pressure conditions.

Diffusion and Migration – The transport of species in the electrolyte is calculated using the Nernst-Planck equation:

$$N_i = -D_i \nabla c_i - z_i u_{mi} F c_i \nabla \Phi_l \tag{3.1}$$

where N_i is the particle flux of species i, D_i the diffusion coefficient, c_i the concentration, z_i the valence, u_{mi} is the mobility, F is Faraday's constant.

Since there is no forced flow, transport is due to diffusion and migration. An effective ambipolar diffusivity is used for the electrolyte, which considers the diffusion of both ions in the electrolyte. The diffusive flow of K^+ and OH^- is coupled due to the requirement of electroneutrality on the movement of the respective ions.

As the electrolyte used is highly concentrated (5 - 6.5 M KOH), a concentrated solution model is considered, and therefore changes in conductivity and diffusivity in the electrolyte are concentration dependent. The electrolyte is modelled using concentrated solution theory with three mobile species: K^+, OH^- and H_2O. Concentrated electrolyte theory for a binary (1:1) electrolyte is used to describe charge transport in the electrolyte phase. For a binary electrolyte with equal valences, electroneutrality stipulates that the concentration of OH- and K+ are taken to be equal at all points in space. The effective ionic and electronic conductivity are corrected to factor in the tortuosity of a porous electrode material filled with liquid electrolyte using the following expression:

$$\sigma_s^{eff} = \sigma_s \epsilon_s^{\Upsilon} \tag{3.2}$$

where σ_s^{eff} is the effective conductivity of the solid electrodes and Υ is the Bruggeman coefficient set to 1.5 for a packed bed of spherical particles[22]. The diffusion coefficient for the electrolyte is corrected to take into account tortuosity and porosity in the same way. Diffusivity in the electrolyte gap is faster due to bubble movement. The empiric relationship used to describe the effect of bubbles in the electrolyte gap is further discussed in a separate section.

Potential – The electronic current in the solid electrode particles is determined by Ohm's law:

$$i_s = -\sigma_s \nabla \Phi_s \tag{3.3}$$

where is the electronic current, σ_s is the solid conductivity, and Φ_s is the potential difference in the solid. The ionic current through the liquid electrolyte can be described by:

$$i_l = -\sigma_l \nabla \Phi_l - \frac{(2\sigma_l RT)}{F} * (1 + \frac{(\delta * \ln \alpha)}{(\delta * \ln C_l)}) * (t_+ + \frac{c_l}{c_0}) * \nabla \ln C_l \tag{3.4}$$

where i_l is the ionic current through the electrolyte, σ_l is the conductivity of the liquid electrolyte, Φ_l is potential in the electrolyte, C_l is the concentration of hydroxide ions in the electrolyte, C_0 is the initial concentration of hydroxide ions, a is the activity, R is the universal gas constant, T is temperature, and F is Faraday's constant. The total current is:

$$i = i_l + i_s \tag{3.5}$$

where is i_s the electronic current through the solid electrodes and i_l is the ionic current through the electrolyte. The boundary condition at the grounded electrode is:

$$\phi_s = 0 \tag{3.6}$$

The Nickel electrode's external metal surface is at one potential, depending on the applied constant current. This defines whether the battery is charging or discharging by multiplying the current value with a step function which changes from 1 to -1 depending on the time. The iron electrode is also at a constant potential, equal to zero since it is considered to be grounded.

The overpotential is calculated as the difference between the electrode potential, the electrolyte potential, and the standard electrode potential.

$$\eta = \phi_s - \phi_l - E^0 \tag{3.7}$$

where η is the overpotential and E^0 is the standard electrode potential of the electrode material. The equilibrium potential of the positive electrode is composition dependent and based on experimental data[22]. A more accurate description of the dependence of the equilibrium potential on the state of charge of the electrode can be found in Appendix A, Figure A.1. Ohm's law is used to describe charge transport in the electrodes. Diffusion inside the porous electrodes is modeled by Fickian diffusion, assuming that the particles are spherical.

Both electrodes are modeled as consisting of spherical porous particles with uniform size and porosity. Particle size and porosity are assumed to be independent of the state of charge of the battery and constant. Each electrode is considered as a two-phase system consisting of a porous particle matrix and liquid electrolyte. Gaseous products are modeled as dissolved species in the liquid electrolyte. Gas build-up is therefore not considered in the model, only dissolved hydrogen and oxygen in the liquid electrolyte, which is a reasonable assumption for low current density operation. Bubbles are considered to increase the ambipolar diffusivity coefficient of the electrolyte. The reverse reactions for both HER and OER are not considered.

Electrochemical reactions – The following electrochemical reactions describe the Faradaic processes occurring at the electrodes.

On the positive nickel electrode:

$$\mathrm{Ni(OH)_2 + OH^- \longleftrightarrow NiOOH + H_2O + e^-}$$
$$\mathrm{4\,OH^- \longleftrightarrow O_2 + 2\,H_2O + 4\,e^-}$$

On the negative iron electrode:

$$\mathrm{Fe(OH_2) + 2\,e^- \longleftrightarrow Fe + 2\,OH^-}$$
$$\mathrm{2\,H_2O + 2\,e^- \longleftrightarrow H_2 + 2\,OH^-}$$

During charging, hydroxide ions move from the negative electrode to the positive electrode. As the battery starts charging, the catalysts for oxygen evolution and hydrogen evolution are generated, resulting in oxygen production on the nickel oxyhydroxide (NiOOH) particles and hydrogen production on the metallic iron surface. The cell potential increases during charging, dependent on the state of charge of the battery. Once fully charged, the device performs solely as an alkaline electrolyser.

Chemical reaction rates are derived from the general Butler-Volmer equation:

$$j = j_0 * (e^{\frac{\alpha_a F \eta}{RT}} - e^{\frac{-\alpha_c F \eta}{RT}}) \tag{3.8}$$

where j is the current density, j_0 the exchange current density, α_a is the anodic charge transfer coefficient, α_c is the cathodic charge transfer coefficient, η is the overpotential, F is Faraday's constant, R is the universal gas constant, and T is the temperature.

The model considers transport of species in one direction. The material balance for species i is given by:

$$R_i = \frac{\delta_i}{\delta t} + \nabla * (-D_i \nabla c_i - z_i u_m i F c_i \nabla \phi_l) \tag{3.9}$$

where R_i is the reaction rate, c_i is the concentration of species, D_i is the diffusion coefficient, z_i is the number of electrons, $u_m i$ is the mobility and ϕ_l is the ionic potential in the liquid electrolyte.

Chemical reactions are proportional to the electrochemically active surface area. This is measured from the active material via BET measurements, and can be found in Appendix A, Section A.4. The intercalation reaction is taken into account as a solid concentration which can then be used to calculate the state of charge considering the amount of active material available:

$$SoC = \frac{c_s}{c_{s,max}} \tag{3.10}$$

where c_s is the average concentration of the reacted species in the electrode materials, $c_{s,max}$ is the maximum concentration that can be loaded, which indicates the theoretical capacity of the battery materials. The exchange current density of the secondary reactions,HER and OER, is assumed to increase linearly with the local SoC of the electrodes. This assumption is made tosimulate the different catalytic activity of the discharged and charged battery electrode materials. The gaseous products of the electrochemical reactions are assumed to remain in liquid phase. In reality, due to the low solubility of both O_2 and H_2 only a small fraction of the gaseous products will dissolve in the electrolyte while most will bubble out. The products of charging and discharging electrochemical reactions remain in the solid phase.

Bubble effects – Although the gas fraction is not explicitly calculated, the increased mass transfer due to bubble movements is simulated as a simple empirical relation. The effects of bubble break-off and the movement of fluid that replaces that space is calculated using the Rousar correlation in a characteristic Sherwood number, Sh_1 [23][24]:

$$Sh_1 = \sqrt{\frac{12}{\pi}} Re_G^{0.5} Sc^{0.5} \theta^{0.5} \tag{3.11}$$

For the effect of growth and wake flow, Vogt's correlation for low bubble coverage (θ smaller than 0.5) is used to calculate another characteristic Sherwood number, Sh_2[24]:

$$Sh_2 = \frac{2}{\sqrt{5}} Re_G^{0.5} Sc^{0.34} (1 - \frac{\sqrt{8}}{3} \frac{R_a}{R} \theta^{0.5})(1+\theta) \tag{3.12}$$

where the total effect of the bubbles is calculated as:

$$Sh_{bubbles} = (Sh_1^2 + Sh_2^2 + 1)^{0.5} \tag{3.13}$$

The bubble coverage, θ, is calculated using the empirical relationship developed by Vogt on a flat-plated electrode[23]:

$$\theta = 0.023 \frac{I}{A}^{0.3} \tag{3.14}$$

where I is the current and A is the geometric area. The Reynolds and Schmidt numbers are described as:

$$Re_G = \frac{V_{gas}}{A} \frac{d_b}{\nu} \tag{3.15}$$

$$Sc = \frac{\nu}{D} \tag{3.16}$$

where d_b is the characteristic length scale, ν is the kinematic viscosity of the electrolyte, D is diffusivity, and the gas volume flux can be defined as:

$$\frac{V_{gas}}{A} = \frac{j}{zF} \frac{RT}{P} \tag{3.17}$$

where R,T, F, and P are known, j is the gas evolving current density and z the number of electrons.

Simplifications from [23] and [24] are used to calculate the effect of bubbles on the diffusion coefficient of the electrolyte. Assumptions of this simplification evaluate the gas production on a flat-plane electrode. As the pocket-type electrodes used in the battolyser are porous, the active surface area per volume will be larger, consequently the electrochemical gas production will be higher. Following Vogt's assumptions, R_a/R is assumed to be 0.75. The resulting value is used to enhance the diffusion coefficient during charging, increasing the ambipolar diffusivity by a factor of 30%.

3.2.2. EXPERIMENTAL VALIDATION

An experimental setup was designed to validate the model results. The setup consists of a commercial Ni-Fe battery (Ironcore Batteries, 10Ah capacity) in its original casing. A schematic representation of the cell design can be found in Appendix A, Section A.6 and the composition of the electrode materials can be found in Appendix A, A.5. The electrodes are kept separate by rubber separator plates to avoid a short-circuit. The set-up includes 3 nickel electrodes and 2 iron electrodes. The battery set-up was conditioned as recommended by the manufacturer. The conditioning procedure consisted of 15 cycles of charge/discharge at C/5 rate. During these cycles ultrapure water is added to replenish the electrolyte once a week.

The electrolyte used in the validation experiments is a 5 M KOH solution. Details on the conductivity of KOH are presented in Appendix A, Figure A.10. A 5 M KOH electrolyte is chosen because of its high conductivity, whereas further increasing the KOH concentration did not significantly increase the conductivity. Ultrapure water, from a Milli-Q water purification system, and KOH flakes (85%, Merck) were used to prepare the electrolyte.

The electrodes used in the experimental tests are commercial electrodes purchased from Iron Core Power, taken from commercial nickel iron batteries with a nominal capacity of 10 Ah. The positive nickel electrode is prepared from $Ni(OH)_2$ precipitated from a nickel sulfate solution using NaOH. This is then filtered, washed and dried. The resulting hydroxide is ball milled with a 13 wt% graphitic carbon additive to increase the conductivity. This material is then compacted and placed in nickel coated steel perforated pockets. The negative iron electrode is composed of ground magnetite Fe3O4, metallic iron, and 2 wt% of graphitic carbon. NaCl is added as a pore former. After compacting and sintering at 700°C the NaCl is dissolved. The active material is compacted and collected in nickel coated steel perforated pockets.

The particle size distribution of both porous electrode materials was measured via scanning electron microscopy (SEM) images. SEM imaging and energy-dispersive X-ray spectroscopy (EDX) were performed using a JEOL JSM 6500F electron microscope. The measured average particle size is used to model diffusion inside the electrode particles. More information can be found in Appendix A, section A.3.

The electrochemically active surface area (ECSA) was measured experimentally using the Brunauer-Emmett-Teller (BET) technique. A Gemini VII 2390p analyzer was used to perform this measurement. It is assumed that the porosity of the materials is independent of state of charge and therefore does not change throughout the charge/discharge

cycles.

The cell was charged at a constant current of 2 A for a duration of 12 hours to account for the total capacity and an additional 2 hours of gas production. Subsequently, the cell was discharged at a constant current of -2 A or until the cell potential dropped to 1.1 V. This is done to limit the iron reaction to the first discharge plateau.

3.3. RESULTS AND DISCUSSION

3.3.1. MODEL VALIDATION

To validate the COMSOL Multiphysics model a representation of the commercial cells is developed. The geometry of the validation model is presented in Figure 3.3 a. Using this 1 dimensional cell geometry simulation, the model is validated experimentally. Experimental and modeling results of the variation of cell potential during charge/discharge cycles at constant current and the gas production quantities are compared. A 1D approach is chosen because it is found to

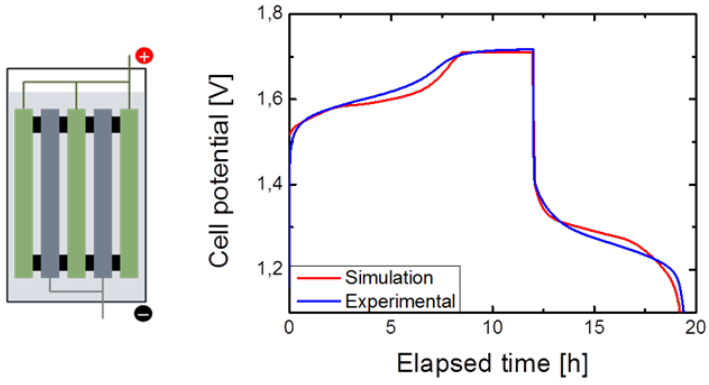

Figure 3.3: a) Schematic diagram of the cell geometry used for validation and b) a comparison of the cell potential during charge and discharge cycles at constant current for experimental and simulation results. Cell potential vs. time during a galvanostatic charge and discharge cycle. Charging and discharging at C/5 rate equal to 2 A.

show good agreement with experimental data and, as bubble formation is not included in the model, height differences will not be taken into account. Therefore, a 1D version that agrees with the experimental data is used to optimize the setup.

As is shown in Figure 3.3 b, the simulated onset potentials of the battery charging reactions and the gas production reactions are very similar to the experimental values. The total discharge capacity is also predicted very accurately. The transition from battery charging in the first hours of operation to gas production, the plateau observed between 9-12 hours of operation, is smoother in the experimental results than in the modeling results. A possible explanation for this difference is the use of a linear relationship between the exchange current density of HER and the state of charge (SoC) of the battery electrodes. Since the catalyst for HER is produced during charging, gas production will

be dependent on the overall SoC of the battery. As can be seen in Figure S6, gas production can be described as two separate linear relationships with different slopes, however, in the model this is simplified to a single linear relationship. The simplification of the dependence of gas production with SoC could therefore explain the smoother transition in experimental data. Particle size and porosity are assumed to be independent of the SoC, and this assumption could also be a possible explanation for the discrepancies between the simulation and the experimental results.

The total gas production quantities predicted by the model were validated with small-scale experimental measurements of the volumes of H_2 and O_2 produced during operation. More information on the measurement of O_2 and H_2 production can be found in Appendix A, section A.6 Figure A.6. At the end of the charging time, after 12 hours of applying current to the system, the total hydrogen production predicted by the model is 0.2 mol. Experimentally, we measured gas production for 9.5 hours. With this data we extrapolated the total gas production for the total 12 hours simulated. Using this linear extrapolation, we obtain a production of 5 L of gas in 12 hours of total charging time, and using the pressure and temperature of the lab at the moment, together with GC measurements of the percentage of hydrogen present in the sample, we measured hydrogen production to be 0.194 mol. This is in accordance to the amount of hydrogen measured experimentally, therefore the model in this respect corresponds with experimental measurements.

Further validation is done by performing galvanostatic charge and discharge cycles at different current rates. The validation data at different currents is presented in Appendix A, SectionA.7. Important parameters such as the potential for gas evolution and the battery capacity are modeled correctly in accordance to the experimental data. The slight differences between experimental and modeling results can be explained by the simplifications and assumptions used to build the model, as described above, and are small enough to proceed with using the built model for the subsequent optimization of the unit cell.

3.3.2. OPTIMIZATION OF BATTOLYSER PARAMETERS

The main objective of this study is to optimize cell parameters to increase the energetic efficiency of the battolyser. The energetic efficiency of the battery component can be calculated using equation 3.18, while the total efficiency of the battolyser considering hydrogen production is calculated using equation 3.19.

$$\eta_{total} = \frac{I_{discharge} * \int_{t_{discharge}}^{t_{total}} V_{cell} dt}{I_{charge} * \int_{0}^{t_{discharge}} V_{cell} dt} \tag{3.18}$$

$$\eta_{total} = \frac{(I_{discharge} * \int_{t_{discharge}}^{t_{total}} V_{cell} dt) + (molH_2 * HHV)}{I_{charge} * \int_{0}^{t_{discharge}} V_{cell} dt} \tag{3.19}$$

Using the model parameters validated in the previous section, a 2-electrode geometry was simulated using COMSOL Multiphysics software. This setup allows for the efficient separation of hydrogen and oxygen gas produced in the electrolysis functionality of the device by including an open mesh polyphenylene sulphide fabric separator coated

with a mixture of a polymer and zirconium oxide, between the negative and positive electrodes. Zirfon PERL is used industrially in alkaline electrolysis as it is one of the few stable separators at high pH values[25]. Therefore, this configuration is used to optimize the unit cell. The parameters that are modified and optimized are the electrode thickness, electrode porosity, the electrolyte conductivity and gap thickness.

Electrode thickness – By modifying the electrode thickness it is possible to modify the energy density of the device by increasing the total amount of active material in a single unit cell. Electrode thickness is varied by multiplying the electrode thickness, maximum theoretical capacity, and current by a certain factor. To keep the charging and discharging time scales constant, the current scales with the amount of active battery material, keeping the current density per active material constant throughout the different scenarios. However, by making the electrode thickness larger, the innermost active material in the porous electrode might be more difficult to charge. Moreover, the distance from one current collector to the other increases as electrode thickness increases, increasing the ohmic drop in the electrodes. This will cause a decrease in the percentage of the electrode that is effectively used during charging and discharging.

The electrode thickness is multiplied by a scaling factor “n” ranging from 0.1 to 4. Results of the efficiencies, battery capacity, and hydrogen production for different electrode thicknesses are presented in Figure 3.4. Increasing the electrode thickness results in a decreased efficiency as can be seen in Figure 3.4 (a). This can be explained by the relatively low electronic conductivity of the electrode materials[22], which is comparable in order of magnitude to the effective ionic conductivity of the electrolyte. However, this effect has to be balanced with the total battery capacity and the final use the battery will have. Since this device integrates two functionalities, it is possible to optimize for increased battery storage or hydrogen production. For example, if hydrogen production is preferred, thinner electrodes with a very high surface area are more beneficial. If a specific application requires a specific battery capacity this can be achieved by modifying the electrode thickness to adapt to the discharging capacity and time-scale. It is therefore important to compare the practical utilization of the battery electrodes and the charging cycle duration. Furthermore, increasing electrode thickness will decrease the relative cost per active separator area[26][27].

Figure 3.4 (b) shows the effect of changing the electrode thickness on the battery capacity and total hydrogen production. Hydrogen production increases more than linear with n, resulting in larger increases at larger scaling factors. This can be due to less of the current being used to charge the battery, as the battery capacity no longer increases linearly with an increasing scaling factor after the thickness is doubled. Because of this, the relationship between battery capacity and hydrogen production changes, resulting in a reduction in both the battery and the total efficiency. Battery capacity begins to plateau after n = 4.

By reducing the thickness of the electrodes there is hardly any change in the efficiency of the device. Nevertheless, it is important to take into account that the battery capacity is reduced because the amount of active material is reduced. Overall, a thinner electrode will result in a higher efficiency due to smaller ohmic drops inside the electrodes. According to Haverkort[28], thinner electrodes result in higher efficiency. However, this does not take into account the time scales required for charging and discharg-

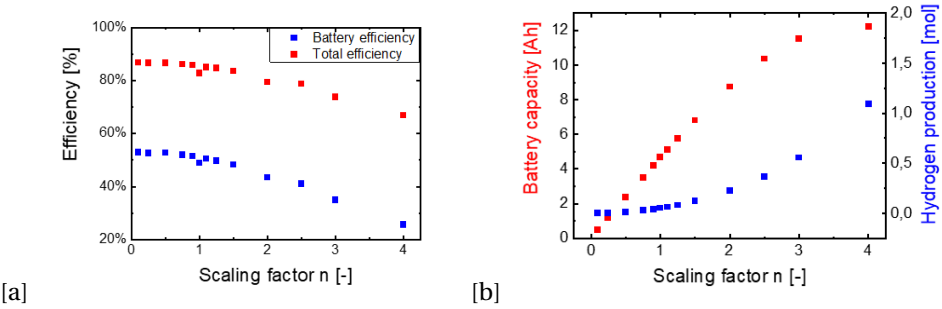

Figure 3.4: a) Battery and total integrated energy efficiency with respect to the scaling electrode thickness factor, where n is multiplied by the electrode thickness to analyze the effect of decreasing and increasing the electrode thickness, and b) battery capacity and total hydrogen production vs. scaling electrode thickness factor.

ing. Depending on the intended function of the battery and the resulting time-scales necessary for charge and discharge of the specific application, battery capacity and discharge time should be included in the analysis.

Taking into account the required battery storage capacity, a thicker electrode is more favorable. Therefore, to increase battery capacity and optimize the energy efficiency of the device, a slightly thinner electrode is chosen as the optimum. Taking into account the time-frame or renewable energy availability, this is chosen to keep the capacity of battery storage to hydrogen production relatively equal. This can be modified depending on the application required, and should be further optimized taking this into account.

Because of the battery capacity required and the hydrogen production increase related to the increase of electrode thickness, the value chosen for these electrodes is n = 0.75 of the benchmark electrode thickness, corresponding to a nickel electrode thickness of 3 mm and an iron electrode thickness of 2.25 mm. Using these electrode thicknesses results in a battery capacity of 3.5 Ah, with a total energy efficiency of 86%.

Electrode porosity – The electrode porosity is defined as the electrolyte volume fraction or the percentage of volume taken up by electrolyte. The starting point is e = 0.5, meaning that equal volumetric portions of the electrode are taken up by active material as electrolyte. This parameter is modified from 0.1 to 0.7, as can be seen in Figure 3.4.

Decreasing the porosity values results in a lower ionic conductivity in the electrode, as the ionic pathways through the porous electrode material would be limited in an electrode with a low volumetric fraction of electrolyte.

Due to the high porosity of the electrode material, the void fraction filled with electrolyte can be larger than the expected void fraction of a packed bed of spheres. Decreasing the porosity results in a higher battery capacity due to the increase in active material. As can be seen in Figure 3.5 (b), as the void fraction increases, battery capacity decreases, as expected. Hydrogen production remains relatively constant with respect to the void fraction.

In the porosity range of 0.15-0.35 electrode volume fraction an optimum device efficiency is found, as this electrode porosity results in an increased total efficiency. This is comparable to a theoretical optimum for a porous foam-like electrode.28 Above e = 0.35

the battery capacity.

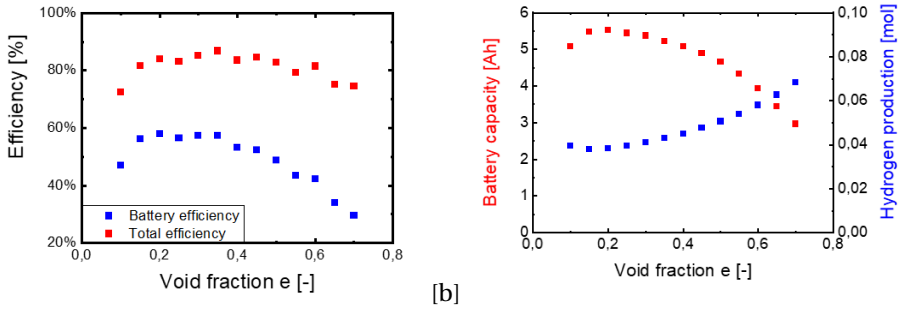

Figure 3.5: a) Battery and total integrated efficiency with respect to the electrode porosity, and b) battery capacity and total hydrogen production vs. the electrode porosity.

reduces because less active material can be charged, and more charge is converted to hydrogen. Smaller void fractions result in similar battery capacity but lower overall efficiency.

Electrolyte conductivity and gap thickness – Both the electrolyte conductivity and gap thickness were also optimized, but as expected, at low current densities the impact on the efficiency is small. Results of this optimization can be found in Appendix A, Figure A.8 and Figure A.9. In short, the highest conductivity of KOH is chosen as optimal, and for this a KOH concentration of 5 M is chosen, as a further increase in KOH concentration results only in a small increase in conductivity[29]. Increasing the gap thickness leads to increasing ohmic resistances. Therefore, the smaller the gap between the electrodes, the lower the ohmic drop. However, there is also an accumulation of gaseous products in the gap that results in a reduction of hydroxide concentration close to the electrode surface[8]. Given the simplification of bubble transport in the model, the optimization results do not consider the products bubbling out. Consequently, a constant gap thickness of 3 mm on each side of the membrane was chosen for the sake of comparison.

3.3.3. DESIGN RECOMMENDATIONS

Following the energy efficiency based modeling optimization the optimal battolyser unit cell will consist of a nickel electrode of 3 mm thickness and an iron electrode of 2.25 mm thick. The electrode material porosity for both electrodes should be designed to be at a void fraction of range between 0.15-0.35. This is possible due to the highly porous active electrode material. The electrolyte consists of a 5 M KOH solution and the electrodes should be placed 3 mm from the membrane, resulting in a total gap thickness of 6.05 mm, including the membrane thickness.

Using the model, specific parameters can be fine-tuned without extensive experimental measurements. This provides a pathway to developing integrated solutions to couple long-term and short-term energy storage. By analyzing the effect of specific parameters and their effect on both battery capacity and total energy efficiency, the unit cell can be optimized to fit a specific application where a certain battery capacity or

hydrogen production is required. Furthermore, the model developed can be used as a complex integration tool where specific functionalities can be improved. The integration of a battery and electrolyser in a single device presents its challenges, as optimizing the device can result in an improvement of only one of the functionalities. Hence, according to the final application of the device a specific end target can be used as the optimization criteria.

A summary of the final optimized cell is presented in Table 3.1.

Table 3.1: Optimized cell parameters

Parameter	Optimized values
Positive electrode	Nickel hydroxide
Positive electrode thickness	3 mm
Negative electrode	Iron hydroxide
Negative electrode thickness	2.25 mm
Electrode void fraction	0.35
Battery capacity	3.5 Ah
Hydrogen production	0.03 mol
Energy efficiency	86%
Pressure	Ambient
Temperature	Ambient

By using the developed modeling tool, charging and discharging cycles can be simulated in approximately 2 minutes, reducing the time required to optimize for specific parameters. This facilitates the iterative design process and allows for many quick modifications in the unit cell layout.

3.4. CONCLUSIONS

We have developed a COMSOL Multiphysics model for the optimization of the battolyser, an integrated battery and electrolyser system. The model includes the electrochemical reactions related to battery charging and discharging, electrochemical reactions of hydrogen and oxygen production, transport mechanisms through the electrolyte gap, membrane and porous electrodes, and effective diffusivity and conductivity inside the porous electrodes. We validated the model with experimental results. Using the simulation results we showed that the optimum electrode thickness is smaller than that of the commercial Ni-Fe battery electrodes used, 0.75 times the commercial electrode thickness, corresponding to an electrode thickness of 3 mm for the nickel electrode and 2.25 mm for the iron electrode. Optimizing for the porosity of the electrodes we found that the optimum range of electrode void fraction lies between 0.15 – 0.35.. Both modifications result in a combined overall efficiency of 86%, compared to a base-case efficiency of 80%.

The electronic resistance from the electrode material and battery capacity are the main limitations of the battolyser design. Battery electrodes are comparatively orders of magnitude thicker than those used in alkaline electrolysis. Therefore, the optimization of the integrated device is a complex process with many trade-offs and depends on

application demands. Depending on the application profile of the device and the main product required – being hydrogen or electricity – the system can easily be optimized by running these simulations.

For a combined approach where both battery storage and hydrogen production are used, an optimized cell design was obtained by modifying the electrode thickness and porosity. Electrolyte conductivity and gap width were also optimized. However, due to the high ionic conductivity of the electrolyte and limited current density, the effect is negligible.

Appendix A includes:

- Model parameters and time dependent equations.
- Experimental details of the materials used, including elemental composition, SEM, XRD, and BET surface area calculation.
- Experimental details for the validation and further modeling results including different charging rates, gap thickness variations and electrolyte conductivity modifications.
- Further simulation results of the electrolyte concentration profiles.

BIBLIOGRAPHY

[1] D. Paul, E. Ela, B. Kirby, and M. Milligan, "The role of energy storage with renewable electricity generation", *National Renewable Energy Laboratory: Golden, CO, USA*, 2010.

[2] IEA, "World energy outlook 2020–analysis", 2020.

[3] H. Ibrahim, A. Ilinca, and J. Perron, "Energy storage systems—characteristics and comparisons", *Renewable and sustainable energy reviews*, vol. 12, no. 5, pp. 1221–1250, 2008.

[4] M. Y. Suberu, M. W. Mustafa, and N. Bashir, "Energy storage systems for renewable energy power sector integration and mitigation of intermittency", *Renewable and Sustainable Energy Reviews*, vol. 35, pp. 499–514, 2014.

[5] K. Ibata-Arens, L. Monticelli, T. Geelan, and K. K. Chen, "Opportunities and challenges for a sustainable energy future", in *Proceedings of the 30th Annual Meeting*, SASE, 2018.

[6] F. Mulder, "Implications of diurnal and seasonal variations in renewable energy generation for large scale energy storage", *Journal of Renewable and Sustainable Energy*, vol. 6, no. 3, p. 033 105, 2014.

[7] A. Evans, V. Strezov, and T. J. Evans, "Assessment of utility energy storage options for increased renewable energy penetration", *Renewable and Sustainable Energy Reviews*, vol. 16, no. 6, pp. 4141–4147, 2012.

[8] J. P. Barton, R. J. Gammon, and A. Rahil, "Characterisation of a nickel-iron battolyser, an integrated battery and electrolyser", *Frontiers in Energy Research*, p. 318, 2020.

[9] K. Agbossou, M. Kolhe, J. Hamelin, and T. K. Bose, "Performance of a stand-alone renewable energy system based on energy storage as hydrogen", *IEEE Transactions on energy Conversion*, vol. 19, no. 3, pp. 633–640, 2004.

[10] N.-K. C. Nair and N. Garimella, "Battery energy storage systems: Assessment for small-scale renewable energy integration", *Energy and Buildings*, vol. 42, no. 11, pp. 2124–2130, 2010.

[11] R. Quadrelli and S. Peterson, "The energy–climate challenge: Recent trends in CO2 emissions from fuel combustion", *Energy policy*, vol. 35, no. 11, pp. 5938–5952, 2007.

[12] R. Ramachandran and R. K. Menon, "An overview of industrial uses of hydrogen", *International journal of hydrogen energy*, vol. 23, no. 7, pp. 593–598, 1998.

[13] F. Mulder, B. Weninger, J. Middelkoop, F. Ooms, and H. Schreuders, "Efficient electricity storage with a battolyser, an integrated Ni-Fe battery and electrolyser", *Energy & Environmental Science*, vol. 10, no. 3, pp. 756–764, 2017.

[14] S. U. Falk and A. J. Salkind, “Alkaline storage batteries”, 1969.

[15] B. Hariprakash, S. Martha, M. Hegde, and A. Shukla, “A sealed, starved-electrolyte nickel–iron battery”, *Journal of Applied Electrochemistry*, vol. 35, no. 1, pp. 27–32, 2005.

[16] A. Shukla, M. Ravikumar, and T. Balasubramanian, “Nickel/iron batteries”, *Journal of power sources*, vol. 51, no. 1-2, pp. 29–36, 1994.

[17] K. Sandeep, S. Kamath, K. Mistry, *et al.*, “Experimental studies and modeling of advanced alkaline water electrolyser with porous nickel electrodes for hydrogen production”, *International Journal of Hydrogen Energy*, vol. 42, no. 17, pp. 12 094–12 103, 2017.

[18] Ø. Ulleberg, “Modeling of advanced alkaline electrolyzers: A system simulation approach”, *International journal of hydrogen energy*, vol. 28, no. 1, pp. 21–33, 2003.

[19] J. Rodrıguez and E. Amores, “Cfd modeling and experimental validation of an alkaline water electrolysis cell for hydrogen production”, *Processes*, vol. 8, no. 12, p. 1634, 2020.

[20] W. Lao-Atiman, K. Bumroongsil, A. Arpornwichanop, P. Bumroongsakulsawat, S. Olaru, and S. Kheawhom, “Model-based analysis of an integrated zinc-air flow battery/zinc electrolyzer system”, *Frontiers in Energy Research*, vol. 7, p. 15, 2019.

[21] S. Yao, R. Zhou, X. Huang, D. Liu, and J. Cheng, “Three-dimensional transient model of zinc-nickel single flow battery considering side reactions”, *Electrochimica Acta*, vol. 374, p. 137 895, 2021.

[22] B. Paxton and J. Newman, “Modeling of nickel/metal hydride batteries”, *Journal of the Electrochemical Society*, vol. 144, no. 11, p. 3818, 1997.

[23] H. Vogt, “Mechanisms of mass transfer of dissolved gas from a gas-evolving electrode and their effect on mass transfer coefficient and concentration overpotential”, *Journal of applied electrochemistry*, vol. 19, no. 5, pp. 713–719, 1989.

[24] T. Burdyny, P. J. Graham, Y. Pang, *et al.*, “Nanomorphology-enhanced gas-evolution intensifies CO2 reduction electrochemistry”, *ACS Sustainable Chemistry & Engineering*, vol. 5, no. 5, pp. 4031–4040, 2017.

[25] A. S. Products, *Zirfon perl utp 500 - specialty products*, http://www.agfa.com/specialty-products/solutions/membranes/zirfon-perl-utp-500/, Accessed: 2018-03-07.

[26] Y. Kuang, C. Chen, D. Kirsch, and L. Hu, “Thick electrode batteries: Principles, opportunities, and challenges”, *Advanced Energy Materials*, vol. 9, no. 33, p. 1 901 457, 2019.

[27] R. Elango, A. Demortière, V. De Andrade, M. Morcrette, and V. Seznec, “Thick binder-free electrodes for Li-ion battery fabricated using templating approach and spark plasma sintering reveals high areal capacity”, *Advanced Energy Materials*, vol. 8, no. 15, p. 1 703 031, 2018.

[28] J. Haverkort, “A theoretical analysis of the optimal electrode thickness and porosity”, *Electrochimica Acta*, vol. 295, pp. 846–860, 2019.

[29] R. Gilliam, J. Graydon, D. Kirk, and S. Thorpe, “A review of specific conductivities of potassium hydroxide solutions for various concentrations and temperatures”, *International Journal of Hydrogen Energy*, vol. 32, no. 3, pp. 359–364, 2007.

4

Effect of Different Alkali Metal Cations on the Oxygen Evolution Activity and Battery Capacity of Nickel Electrodes in Concentrated Hydroxide Electrolytes

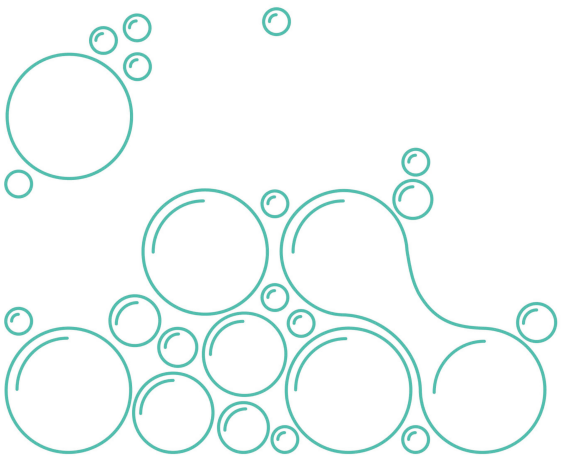

The effect of different alkali metal cations on the oxygen evolution activity and battery capacity of nickel electrodes has recently been studied in low concentration alkali hydroxide electrolytes. As high concentration hydroxide electrolytes are favored in applications due to their high conductivity, we investigate if the cation effects observed in low concentration electrolytes translate to more industrially relevant conditions for both alkaline water electrolysis and nickel iron batteries. We investigate the alkali metal cation effect on the electrochemical properties of nickel electrodes in highly concentrated hydroxide electrolytes by adding Li^+, Na^+, Cs^+ and Rb^+ cations to a 6.5 M KOH electrolyte, while keeping the hydroxide concentration constant. For OER we find a trend in activity similar to that at low concentrations Rb^+>Cs^+>K^+>Na^+>Li^+, where especially larger additions of Rb^+ and Cs^+ (1 M or 0.5 M) cause a significant decrease in OER potential. Smaller cations interact with the layered hydroxide structures in NiOOH to stabilize the α/γ phases and increase the potential for OER. The intercalation of small cations also causes an increase in battery electrode capacity because of the higher average valence of the $Ni(OH)_2$/NiOOH α/γ pair. Small concentrations of Li^+ added to a concentrated KOH electrolyte can therefore be beneficial for the nickel electrode battery functionality and for an integrated battery and electrolyser system, where it increases the battery capacity without a significant increase in OER onset potential.

4

Highlights

1. *The effect of highly concentrated alkali hydroxide mixtures on the oxygen evolution activity and battery capacity of nickel electrodes has been investigated*
2. *A similar trend in oxygen evolution activity is found as reported for low concentration electrolytes*
3. *Additions of Li^+ are found to have a lasting effect on the battery capacity of nickel electrode*
4. *Small additions of LiOH to concentrated KOH are found to be optimal for an integrated battery and alkaline electrolysis device*

This chapter has been published in Electrochimica Acta Volume 415, 20 May 2022, 140255

4.1. INTRODUCTION

An increase in both global population and energy demand, together with a rising percentage of renewable energy sources on the grid, demand an increase in energy storage capacity[1][2][3]. Electrochemical storage techniques will play a key role in the energy transition to cleaner and more sustainable energy forms[4][5][6].

Batteries have a high energy efficiency and high roundtrip efficiency, but are not ideal for longer term storage due to self-discharge and costs. Water electrolysis can be advantageous for longer term, seasonal storage as the hydrogen that is produced can be stored for prolonged periods of time[7]. Battery storage and water electrolysis can also be integrated in a single device to provide both long-term and short-term storage capacity[7]. The battolyser, an integrated battery and electrolyser device, combines two different energy storage functionalities: a nickel-iron battery and an alkaline electrolyser[8][9]. Electricity can be stored and generated from the materials in the electrodes via the $Ni(OH)_2$/NiOOH and $Fe(OH)_2$/Fe redox couples[10]. When the maximum battery capacity is reached, the battolyser makes use of the electrocatalytic properties of Fe and NiOOH for electrochemical hydrogen and oxygen evolution and the device acts as an alkaline electrolyser. Thereby, the excess electricity that cannot be stored in the battery functionality is used to split water molecules from the electrolyte, generating hydrogen and oxygen[7][11]. The relevant reactions on both the nickel and iron electrode are given below, alongside their standard equilibrium potention (E^0):

Nickel electrode:

$$Ni(OH)_2 + OH^- \longleftrightarrow NiOOH + H_2O + e^- \ (E^0 = 0.53\,V \text{ vs SHE})$$
$$4\,OH^- \longleftrightarrow O_2 + 2\,H_2O + 4\,OH^- \ (E^0 = 0.40\,V \text{ vs} \cdot \text{ SHE})$$

Iron electrode:

$$Fe(OH)_2 + 2\,e^- \longleftrightarrow Fe + 2\,OH^- \ (E^0 = -0.87\,V \text{ vs} \cdot \text{ SHE})$$
$$2\,H_2O + 2\,e^- \longleftrightarrow H_2 + 2\,OH^- \ (E^0 = -0.83\,V \text{ vs} \cdot \text{ SHE})$$

The development and evaluation of different catalysts for the oxygen evolution reaction (OER) has been the subject of a considerable amount of research in recent years. Nickel oxyhydroxide layered double hydroxides (NiOOH-LDH) are promising materials for OER in alkaline conditions because of their excellent catalytic performance and lower costs compared to other good electrocatalytic materials, such as IrO_2 and RuO_2[12]. Nonetheless, most experimental studies have used dilute electrolyte solutions to study these electrocatalysts, even though the pH of the electrolyte solution is known to affect the catalytic properties of NiOOH materials and industrial applications make use of highly concentrated electrolytes[13][14].

Studies focusing on electrolyte effects have shown that cations can intercalate into the $Ni(OH)_2$ layered structure and thereby modify its electrocatalytic performance[15][16]. Constantin et al. report a modification in the hydroxide layers leading to an increase in the catalytic activity of OER on NiOOH in the presence of Li^+[17]. The intercalation of Cs^+ cations has been shown to elongate Ni-O bonds because of their larger size[18][19]. Garcia et al. report that the OER activity of NiOOH in alkali hydroxide electrolytes follows the trend Cs^+>Na^+>K^+>Li^+. Using surface enhanced Raman spectroscopy (SERS) they

show that the presence of cations affects the formation of the superoxo OER intermediate ($Ni-OO^-$). The cations interact with the $Ni-OO^-$ species, forming a $Ni-OO^-M^+$ species that is stabilized by bigger cations, such as Cs^+. The $Ni-OO^-M^+$ species then serve as a precursor to OER[20]. This indicates that alkali metal cations have a significant effect on OER activity of NiOOH and therefore can be used to tune the reactivity of the catalytic surface[18]. However, all of these effects have solely been reported in low concentration electrolytes, typically using a 0.1 M alkali hydroxide electrolyte, and therefore there is little insight on how these processes affect alkaline electrolysis in more industrially relevant, concentrated alkali hydroxide electrolytes.

Moreover, the presence of alkali cations in the electrolyte has a substantial effect on NiFe battery operation. Typically, LiOH is added to KOH electrolytes in NiFe batteries to increase the lifetime and cycleability of the batteries[21]. Specifically, the addition of LiOH has been shown to increase the lifetime of the positive $Ni(OH)_2$ electrode[10], as at temperatures above 40°C Fe can dissolve into the concentrated KOH electrolyte and migrate towards the positive Ni electrode. This leads to Fe inclusions in the Ni electrode that can stabilize the NiOOH α/γ phase, leading to a lower onset potential for OER[22]. Fe has been reported to intercalate into $Ni(OH)_2$ after only 5 cyclic voltammetry cycles, resulting in larger intersheet spacing in the $NiFe(OH)_2$ structure [23]. This in turn causes a shift in potential for the $Ni(OH)_2$/NiOOH redox couple and a reduction in the onset potential for OER. These alterations result in a higher electron capacity for battery storage due to the higher average valence of the $Ni(OH)_2$/NiOOH α/γ pair and a higher loss due to the secondary oxygen evolution reaction [24] [25] [26].

Here, we investigate the effect of concentrated alkali hydroxide electrolyte mixtures on the OER performance and battery functionality of nickel electrodes. We do this by adding specific concentrations of alkali cations, namely Li^+, Na^+, Cs^+, and Rb^+, to highly concentrated KOH electrolytes and performing both rotating disk electrode (RDE) and battery cycling experiments. Moreover, we optimize the electrolyte composition for the integration of both the NiFe battery and alkaline electrolysis functionalities in a hybrid device such as the battolyser. For OER we find a trend in activity similar to that at low concentrations $Rb^+ > Cs^+ > K^+ > Na^+ > Li^+$, where especially larger additions of Rb^+ and Cs^+ (1 M or 0.5 M) cause a significant decrease in OER potential. Smaller cations interact with the layered hydroxide structures in NiOOH to stabilize the α/γ phases. The intercalation of small cations also causes an increase in battery electrode capacity because of the higher average valence of the $Ni(OH)_2$ /NiOOH α/γ pair. Small concentrations of Li^+ added to a concentrated KOH electrolyte can therefore be beneficial for the nickel electrode battery functionality and for an integrated battery and electrolyser system, where it increases the battery capacity without a significant increase in OER onset potential.

4.2. Experimental Methods

4.2.1. Electrode preparation for RDE experiments

5 mm diameter, 4 mm thick Sigradur G glassy carbon (GC) mirror polished disks (HTW Hochtemperatur-Werkstoff GmbH) were used as working electrode substrates. To clean the electrodes, the GC disks were sonicated for 10 minutes each in ultrapure water, ace-

tone, isopropanol, and again in ultrapure water.

The drop-casting procedure used in this study is based on a literature procedure[27][28]. Powder-based inks were made using the active material of the commercial battery electrodes (Ironcore Batteries, patent nr. US20140377626A1), using 3.8 mL ultrapure water (MilliQ), 1.0 ml 2-propanol (≥ 98 technical grade, VWR Chemicals), 40 μ l of 5% Nafion 117 solution (Sigma Aldrich), and 80 mg of the active battery material powder. The metal oxide powder contains impurities and graphitic carbon included in the battery for additional conductivity. Characterization of the commercial electrode materials using ICP-OES results are presented in Appendix B, Table B.2. The inks were sonicated for 15 minutes after which 10 μ l of catalyst ink was drop-cast onto the mirror-polished GC disk and subsequently dried in an oven at 60°C for 10 minutes.

4.2.2. ELECTROLYTE PREPARATION

Experiments were performed in electrolytes with a 6.5 M hydroxide ion concentration prepared from high-purity LiOH (99.995% trace metals basis, Sigma-Aldrich), NaOH (99.99% trace metals basis, Sigma-Aldrich), KOH (99.99% trace metals basis Sigma-Aldrich), CsOH (≥99.5%, Sigma-Aldrich) and RbOH (99%, Sigma-Aldrich). MilliQ ultrapure water (18 MΩ) was used to prepare the electrolytes. The electrolyte consisted of either pure KOH or KOH with a MOH additive, where M is either Li^+, Na^+,Cs^+,Rb^+. The concentration of KOH and MOH is varied in accordance to Table 4.1, while keeping the total OH^- concentration constant, resulting in a total of 17 different electrolyte compositions being tested.

Table 4.1: Electrolyte composition variations used in this study. The total hydroxide concentration is kept constant at 6.5 M, while different alkali hydroxides (M = Li, Na, Cs, Rb) are mixed with KOH.

KOH	MOH (M=Li, Na, Cs, Rb)
5.5 M	1 M
6 M	0.5 M
6.4 M	0.1 M
6.45 M	0.05 M

4.2.3. ROTATING DISK ELECTRODE (RDE) MEASUREMENTS

The GC working electrodes were mounted on a RDE assembly (Pine MSR) and cyclic voltammograms (CVs) were recorded in a three electrode cell using a Biologic VSP-300 potentiostat. A literature methodology for testing OER catalysts was used for the RDE experiments to obtain reproducible results[29]. Prior to the electrochemical measurements, the electrolyte solution was purged with O_2 for 30 minutes. During the CV measurements the cell was kept blanketed under O_2 by applying an O_2 flow over the electrolyte. A schematic representation of the RDE assembly is presented in Appendix B, Figure B.4.

A three electrode cell configuration with an Ag/AgCl reference electrode (Origalys, sat. KCl) and a carbon rod counter electrode (99.999%, Strem Chemicals) was used for all electrochemical tests. All potentials were converted from the Ag/AgCl scale to the

reversible hydrogen electrode (RHE) scale and are reported as such. The ohmic drop was measured using Potentiostatic Electrochemical Impedance Spectroscopy (PEIS) with a 20 mV amplitude and CV measurements and corrected for at 85% using the Biologic EC-Lab software. The additional ohmic drop was compensated for manually. CV scans were recorded from 0.7 to 1.7 V vs. RHE for 5 cycles at 1600 rpm with a scan rate of 20 mV $s^{-}1$. The charge of the nickel oxide reduction peak was used to calculate the total amount of active material drop-cast on the electrodes.

Consequently, all of the CVs are plotted with respect to the mass (in mg) of active material present on the electrodes for the sake of accurate comparison.

4.2.4. Battery cycling

A BioLogic BCS-815 Battery cycler was used to run the charge/discharge cycles on commercial NiFe batteries (Ironcore Batteries). Galvanostatic charge/discharge cycles were performed with a potential limitation of 1.1 V to avoid over-discharging.

First, thirty battery conditioning cycles were performed on each battery using a 5 M KOH (85% Sigma Aldrich) solution as electrolyte. The rated capacity of these batteries is 10Ah. The charge/discharge cycles were performed using a recommended charging rate of C/5 and a discharge rate of C/6.6. This coincides with a constant current of 2 A during charging and -1.5 A during discharge. The long-term battery experiments were performed in a highly resistant plastic enclosure, namely the cell where the commercial batteries are sold. This ensures that the experiments are performed in highly alkaline resistant cells. The electrolyte level was kept above the minimum by manual inspection and addition of MilliQ ultrapure water when necessary. After the conditioning phase the electrolyte composition was varied as shown in Table 4.2. Thirty galvanostatic charge/discharge cycles were performed at the same charge and discharge rate as mentioned before.

Table 4.2: Battery cycling test steps and details

Test phase	Electrolyte Details	Number of cycles
1	5 M KOH	30
2	6.5 M OH^- concentration	30
3	5 M KOH	30

4.3. Results and Discussion

4.3.1. Rotating disk electrode measurements

The effect of different cations on both the battery and the electrolysis reactions can be seen in cyclic voltammetry (CV) scans using a RDE setup. A detailed schematic of the setup is shown in Appendix B, Figure B.4. The electrode material is dropcasted using a binder, which can result in (partial) coverage of the active material by the binder itself. Additionally, during the CV experiments, some of the dropcasted material can detach from the electrode surface due to bubble formation. This makes it difficult to relate the amount of electrode material dropcasted on the GC electrode to the actual amount of active material. To provide a comparable measurement between different electrolyte

compositions, the total amount of active material is calculated using the total charge of the nickel hydroxide reduction peak.

Four different concentrations of each alkali cation in KOH were tested, and the results of the experiments with the highest MOH concentrations (1.0 M MOH + 5.5 M KOH) are shown in Figure 1. The total data set of cyclic voltammograms with different MOH concentrations is included in Appendix B, Figure B.1. Although iron incorporations in the nickel material will affect the electrochemical performance of the anode, they are considered to be uniform across all measurements as the electrode material contains 0.1 wt% iron (see Table B.2). Therefore we hypothesize that iron inclusions from electrolyte impurities will have a negligible effect.

On the basis of the CVs shown in Figure 4.1, we can determine the effect of the electrolyte composition on both the battery and the electrolyser functionalities of the nickel hydroxide electrode. The peak potentials for both $Ni(OH)_2$ oxidation and NiOOH reduction are used to determine the effect of adding specific alkali metal cations on the battery functionality, as these potentials are key performance indicators for the charging and the discharging reactions. This is due to the fact that a decrease in the potential difference between the $Ni(OH)_2$ oxidation and

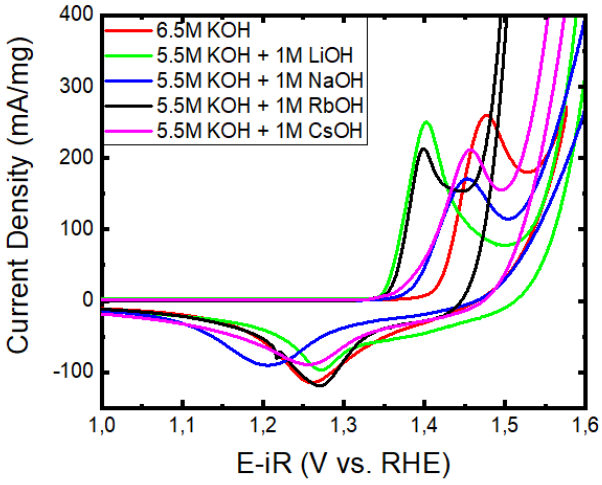

Figure 4.1: Cyclic voltammograms of $Ni(OH)_2$ material deposited on a GC electrode recorded in different electrolytes with a total OH- concentration of 6.5 M. Measurements were performed using an RDE setup with a rotation speed of 1600 rpm and the voltammograms were recorded at scan rate of 20 mVs^{-1}. Five cycles were performed, and the figure shows the third cycle for all electrolyte compositions. The currents are normalized by milligrams of $Ni(OH)_2$ electrocatalyst present for the sake of comparison.

NiOOH reduction peak potential indicates a higher voltaic efficiency for the battery functionality.

In Figure 4.1 we see that the addition of different alkali metal cations has different effects on the $Ni(OH)_2$/NiOOH redox potentials. In the presence of Li^+ and Rb^+ a lower oxidation potential is observed, with respect to a pure KOH electrolyte, while the highest

reduction potentials are observed in the presence of Li^+, Rb^+ and in a pure KOH electrolyte.

To investigate the effect of alkali metal cation additions on the OER activity in concentrated hydroxide electrolytes, we compare the potential necessary to reach a current density of 200 mA/mg. In Figure 4.1 we can clearly observe that these potentials are dependent on the presence of the alkali cations in the electrolyte. In these highly concentrated electrolytes the trend for OER activity, comparing the potential necessary to reach 200 mA/mg, is $Rb^+ > Cs^+ > Na^+ > Li^+$. It is important to note that the majority of the electrolyte for all these experiments is composed of KOH, and only a fraction of the cations present stem from the MOH additions. The trend we observe in concentrated solutions is similar to the trends observed in low concentration electrolytes, where the trend for OER activity is reported to be $Cs^+ > Na^+ > K^+ > Li^+$[30].

A summary of the CV characteristics, including peak oxidation and reduction potential and OER potential of all the alkali metal cation concentrations tested is shown in Figure 4.2. To improve battery functionality the peak oxidation potential (purple) should be as low as possible, and the peak reduction potential (green) should be as high as possible. This will result in the lowest charging potential and the highest discharging potential. To increase gas production, the potential at which OER happens (blue) should be as low as possible.

The mixture with the most favorable onset potential for OER is 1 M of RbOH and 5.5 M KOH. The addition of Rb^+ shows a proportional trend in the peak oxidation and reduction potentials of $Ni(OH)_2$ /NiOOH and OER potential with respect to concentration, meaning that an increase in Rb^+ concentration will result in an increase in the potential at which the discharging reaction takes place and a decrease in the potentials of the charging reaction and OER. For Li^+ mixtures a similar trend is observed for the peak oxidation and reduction potentials of $Ni(OH)_2$ /NiOOH, however the OER potentials remain rather constant at different Li^+ concentrations. The OER potentials for the Li^+ mixtures are the highest in comparison to the mixtures with other alkali cation mixtures, indicating that Li^+ additions have a negative effect on the OER activity of the NiOOH electrode.

This is in agreement with earlier work in low concentration hydroxide electrolytes[20]. The increase in concentration of Na+ does not result in a proportional difference in the redox potentials or OER potential. For CsOH additions an increase in the peak oxidation potential is observed with increasing Cs^+ concentrations, while both the peak reduction potential and OER potential are relatively constant and are not affected by the concentration of CsOH added.

Overall, the data shows how the addition of different concentrations of alkali metal cations can be used to tune the reactions happening, both for the battery functionality and the electrolysis functionality of a nickel electrode. In an integrated device the modification of the electrolyte composition can be used to alter the ratio of the different products, battery storage and hydrogen production. Taking the results of Figure 4.2 into account, LiOH, RbOH, and CsOH additions seem to be the most suitable to integrate both technologies, because they allow for a higher voltaic battery efficiency, and depending on the alkali metal cation concentration, can also result in a lower potential for the OER, depending on the concentration.

It is reported that the α/γ phases of $Ni(OH)_2$ /NiOOH have a higher onset potential

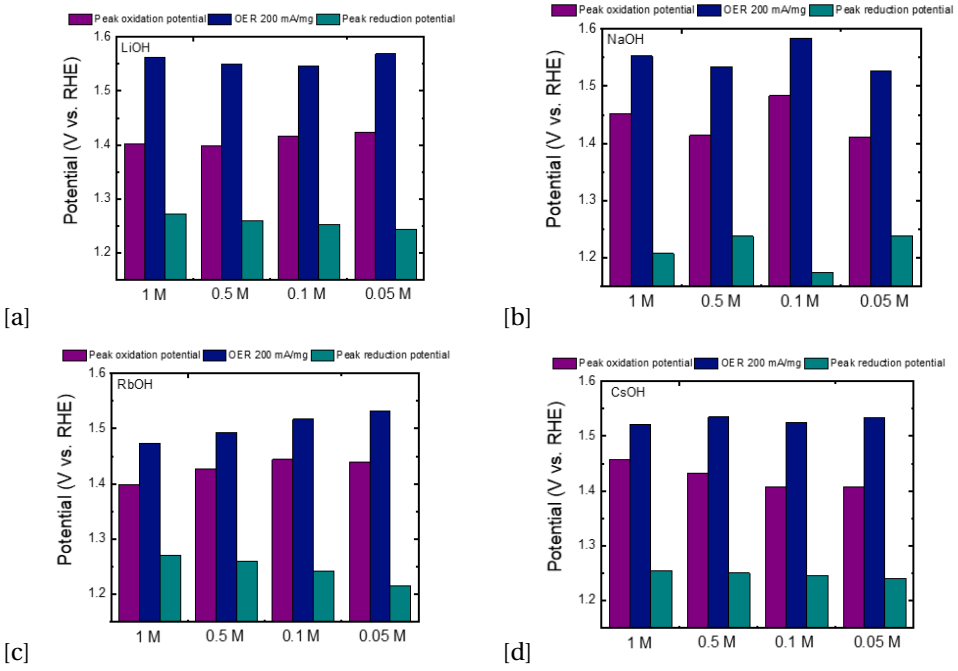

Figure 4.2: Peak oxidation (red) and reduction (green) potential of the $Ni(OH)_2$ /NiOOH redox couple and the potential at which 200 mA/mg for OER (blue) is reached for different electrolyte compositions. (a) LiOH, (b) NaOH, (c) RbOH, and (d) CsOH additions to a KOH electrolyte. Data from cyclic voltammograms of a $Ni(OH)_2$ film deposited on a GC-RDE at 1600 rpm.

for OER[22][31][32][33]. It is therefore possible that the Li^+ cations can intercalate in the nickel layered hydroxide structure and stabilize the α/γ phases. This could further explain the difference in the catalytic activity of OER reported by Garcia et. al[20], where there is a different behavior at higher potentials with Li^+ and K^+ electrolyte than with Cs^+ and Na^+ at low concentrations. In their results this is shown in a different slope during LSVs with the different cations, where Li^+ and K^+ behave differently than Cs^+ and Na^+. In highly concentrated, pure KOH electrolytes, Cappadonia et al. found that β-$Ni(OH)_2$ is more stable than α-$Ni(OH)_2$, and that the α phase will transform into the β phase over time[32]. We believe that the presence of specific alkali metal cations, namely Li^+ because of its smaller size, can stabilize the α/γ phase in highly alkaline electrolyte solutions. Even small additions of Li^+ result in a consistently modified electrochemical behavior. The resulting lower OER activity coincides with the stabilization of α/γ phases of $Ni(OH)_2$ /NiOOH, where Li^+ additions result in a higher onset potential for OER.

Although the RDE experiments provide information on both the battery and the electrolyser functionalities, the amount of material on the surface is small. Therefore, to test the long-term effects of alkali metal cation additions and to better mimic the effects on the integration of both electrolysis and battery charging/discharging reactions, further experiments were performed in battery setups to determine whether these effects are

also observed during longer time battery cycling experiments.

4.3.2. Battery Cycling

To compare the results of long-term battery cycling experiments, the discharge capacity of each battery cycle has been calculated. First, the batteries electrodes were conditioned for 30 cycles in 5 M KOH. Then, 30 additional charging/discharging cycles were run with the electrolytes detailed in Table 4.1. Finally, 30 cycles in 5 M KOH were run after the cycles with electrolyte mixtures to determine if the effect of the alkali metal cation is only present when the cation is present in the electrolyte solution. The last cycle (cycle number 30) of each step in the protocol is shown in Appendix B, Figure B.2 for all 16 batteries. Changes in the battery capacity after the charging/discharging cycles in a 5 M KOH electrolyte and in the electrolyte mixtures are shown in Figure 4.3. The discharge capacity of each battery in the last cycle of the activation phase was used as a reference point and the discharge capacity of each battery in the relevant electrolyte was compared to the reference point. All changes in the battery capacity are given as percentages. Increasing the concentration of both Li^+ and Rb^+ leads to lower increases in battery capacity. For Cs^+ mixtures this is not the case as the battery capacity remains constant with 0.05 M Cs^+ in the electrolyte and increases only with higher Cs^+ concentrations. The findings of the battery tests coincide with the findings of the RDE experiments where Li^+ presented a low peak oxidation potential and a high peak reduction potential, together with a lower OER activity.

Only with the addition of LiOH, in all concentrations except the lowest (0.05 M LiOH + 6.45 M KOH), does the capacity not decrease after flushing the batteries and replacing the electrolyte by a pure KOH solution. This indicates that the addition of LiOH in the electrolyte brings about a permanent change in the electrode materials. The effect of the Li^+ addition can be seen up to 30 cycles after it is removed from the electrolyte. Thereby, Li^+ additions improve the battery capacity even after the Li^+ has been removed from the electrolyte. Although some of the other cations have a positive effects on the battery discharge capacity, this is only the case with the cation present in the electrolyte. For the other cations, in particular Rb^+ and Cs^+, the increased battery capacity starts to lower in the first cycle where the electrolyte is changed, but drops off considerably after approximately 20 cycles.

There is little information on the effect of Li^+ in NiFe batteries reported in literature. Lei et al. report that the use of LiOH in KOH electrolyte enhances the dissolution of iron in the electrolyte, therefore increasing Fe crossover in the battery cell. They attribute this increased capacity to the formation of porous iron structures in the negative electrode due to Li^+ incorporation[34]. Posada and Hall also report an increase in the performance of the battery with the addition of LiOH[35]. Hills confirms that an increase in the efficiency of the nickel oxide electrode is the cause of the enhanced performance in batteries containing LiOH in the electrolyte, possibly due to a change in the conductivity[36]. Here we have shown that the addition of Li^+ brings about a permanent change in the capacity of the nickel electrode. This is a strong indication that Li^+ is intercalated into the nickel electrode, stabilizing the α/γ phases that have higher average oxidation states.

It has been shown that the standard electrode potentials of the $Ni(OH)_2$ /NiOOH redox couple can shift due to the organization of the lattice structure in both α/γ and β/β

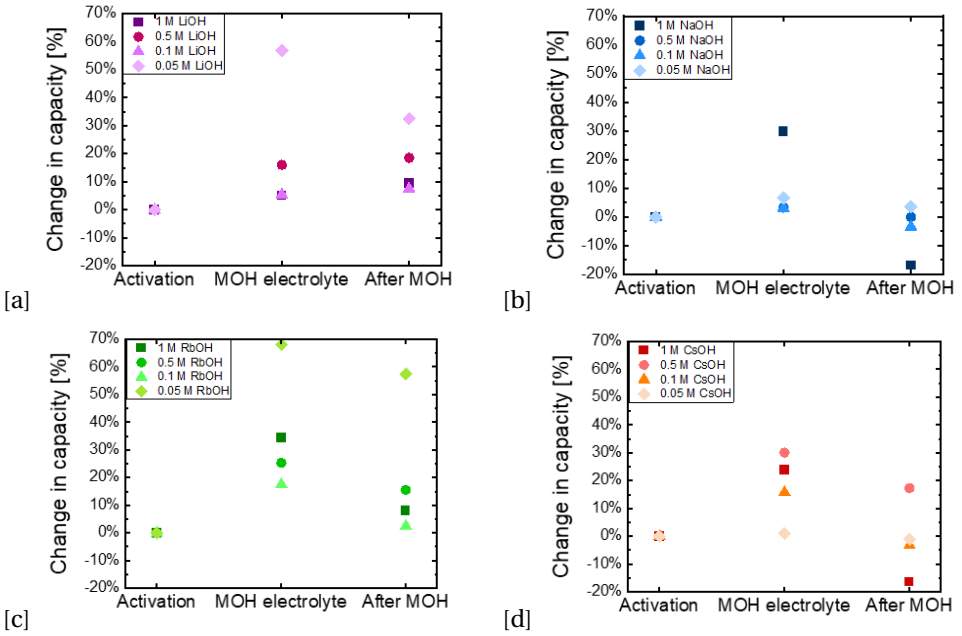

Figure 4.3: Changes in the discharge capacity after 30 subsequent charging/discharging cycles in 5 M KOH (activation), electrolyte mixtures (MOH electrolyte) and 5 M KOH (after MOH). The discharge capacity of the last cycle of each phase is calculated and compared to the capacity after activation of each individual battery. Changes in the discharge capacity are displayed as percentages with respect to the activation phase as references. The figures shows electrolytes containing: (a) LiOH, (b) NaOH, (c) RbOH, and (d) CsOH additions to a KOH electrolyte.

systems[22]. Therefore, it is possible that by including the cations in long-term cycling of the battery, the lattice parameters are stabilized and organized in a specific way. The γ-NiOOH phase has a larger interspatial sheet distance due to the presence of additional water and alkali metal cations. Furthermore, it has a higher average oxidation state, which would explain the larger battery capacity obtained. It is reported that the uptake of alkali metal cations is expected in the γ-NiOOH phase and not in the β-NiOOH phase[22]. Therefore, by adding a small percentage of LiOH to the KOH electrolyte the α/γ phase is stabilized resulting in a higher battery capacity. As shown by the RDE experiments the stabilization of this phase does not significantly increase the potential at which oxygen is evolved. Our results indicate that there is an optimal cation concentration for the stabilization of the α/γ phase, leading to concentration dependent increases in battery capacity. The interaction of Li^+ with the NiOOH phases is strong, as the addition of Li^+ brings about a permanent change in the electrode, indicating that Li^+ is not leached out of the electrode during charging/discharging cycles.

4.3.3. BATTOLYSER ELECTROLYTE OPTIMIZATION

Since the battolyser functions as both a battery and an electrolyser it is also important to investigate the potential at which water electrolysis takes place with the addition of these

cations. For optimizing a hybrid application, such as the battolyser, positive effects on the battery capacity can be counteracted by an increase in the potential for water splitting, as the energy efficiency of the application is dependent on both functionalities. To determine the cell potential at which water electrolysis occurs in the integrated device, the last 5 cycles of the experiments with different MOH concentrations added to the KOH electrolyte are taken into account. The highest potential of the charging plateau from the last 5 cycles are averaged to determine the average potential at which gas evolution happens. Figure 4.4 indicates the average cell potentials at which water electrolysis occurs, and the error bars indicate the deviation of these values over the last 5 cycles.

The data in Figure 4.4 indicates that for high concentrations of LiOH and NaOH (1 M and 0.5 M Li^+, 1 M Na^+) the potential for gas evolution is indeed significantly higher than that for pure KOH. The decrease in potential with decreasing MOH concentration is very closely related to the an increase in the overall conductivity of the electrolyte, the electrolyte mixture had a 6.5 M MOH concentration while the benchmark is a 5 M KOH electrolyte used for the activation cycles. Therefore, we mainly observe that the gas evolution functionality increases when the conductivity of the solution results in a decreased gas evolution potential.

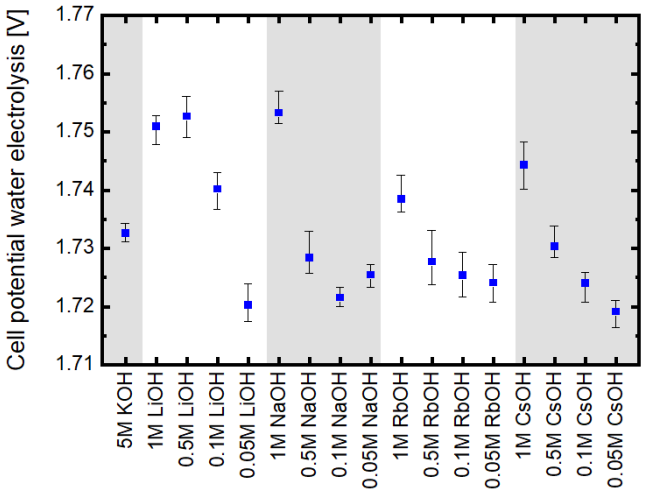

Figure 4.4: Cell potentials at which gas evolution (H_2 and O_2 evolution) occurs after full charging NiFe batteries for 17 different electrolyte compositions at a 2 A charging current. Average values of 5 cycles are presented, where the error bars indicate the maximum and minimum values of the 5 last cycles.

With regards to electrolyser functionality and optimizing the amount of hydrogen produced, we look to reduce the cell potential for gas evolution. Therefore, in this case, taking into account the data from RDE and battery cycling, the lower concentrations of alkali metal cation additions are beneficial. Regarding the NiFe battery functionality and the widespread use of LiOH in high concentrations, we have shown that the Li^+ additions increase battery capacity and in high concentrations will increase the onset potential for

gas evolution. Therefore, to optimize the battery functionality high concentrations of LiOH are beneficial.

For the integrated device it is important to optimize including the trade-offs of the combined effects. Therefore, LiOH additions seem promising, since they result in higher battery capacity. These additions should be kept in the low concentrations, as increasing the LiOH will only decrease the electrolyte conductivity and will result in a higher onset potential for gas evolution. In this way, both functionalities can be integrated and the battolyser device can combine both battery and electrolysis functionalities. Interestingly, 0.05 M RbOH additions also display a large increase in the battery capacity, even surpassing the effect of LiOH additions. The cell potential necessary for gas evolutions with a 0.05 M RbOH addition is however slightly higher than the cell potential with a 0.05 M LiOH addition. This indicates that these RbOH additions are preferred when optimizing for battery capacity, while LiOH additions are preferred when optimizing for gas evolution. It should be noted however that Li^+ additions will be less costly than Rb^+ additions if used for larger scale applications. Overall, we conclude that the electrolytes that should be used to provide optimum energy efficiencies for this integrated device are either a 0.05 M LiOH + 6.45 M KOH electrolyte or a 0.05 M RbOH + 6.45 M KOH electrolyte, since these will result in the highest battery capacity and the lowest cell potential for gas evolution.

4.4. CONCLUSIONS

Here, we have investigated the effect of alkali hydroxide additions to concentrated KOH electrolytes on the OER performance and battery capacity of nickel electrodes. We show that the addition of different metal alkali cations has an effect on the electrochemical performance of the nickel electrode, both with regards to battery capacity and OER activity. For OER activity, the trend found during RDE setup experiments in high concentration hydroxide electrolytes is Rb^+>Cs^+ >K^+>Na^+>Li^+. This is possibly due to the size effect of the different cations, as smaller cations, such as Li^+, can intercalate in the NiOOH-LDH and stabilize the γ-NiOOH phase. This results in a higher onset potential for OER. For the larger cations, Rb^+ and Cs^+, we find that only large additions (of 1 M or 0.5 M) cause a significant decrease in OER potential. The intercalation of small cations also causes an increase in battery electrode capacity because of the higher average valence of the $Ni(OH)_2$ /NiOOH α/γ pair. Small concentrations of Li^+ added to a concentrated KOH electrolyte can therefore be beneficial for the nickel electrode battery functionality and for an integrated battery and electrolyser system, where it increases the battery capacity without a significant increase in OER onset potential Further experiments with NiFe batteries at longer time scales show that the effect of lithium inclusions in the nickel electrode are still present in the battery capacity for at least 30 cycles after the electrolyte has been changed to pure KOH. For an integrated device, with both battery and electrolyser functionality, we find that the optimum electrolytes are either a 0.05 M LiOH + 6.45 M KOH electrolyte or a 0.05 M RbOH + 6.45 M KOH electrolyte, as these result in a higher battery capacity and lowest cell potentials for gas evolution.

4.5. Acknowledgements

The authors would like to acknowledge Michel van den Brink for performing ICP-OES measurements and Simone Asperti for SEM images.

BIBLIOGRAPHY

[1] M. D. Leonard, E. E. Michaelides, and D. N. Michaelides, "Energy storage needs for the substitution of fossil fuel power plants with renewables", *Renewable Energy*, vol. 145, pp. 951–962, 2020.

[2] T. Tsoutsos, N. Frantzeskaki, and V. Gekas, "Environmental impacts from the solar energy technologies", *Energy policy*, vol. 33, no. 3, pp. 289–296, 2005.

[3] G. Coppez, S. Chowdhury, and S. Chowdhury, "The importance of energy storage in renewable power generation: A review", in *45th International Universities Power Engineering Conference UPEC2010*, IEEE, 2010, pp. 1–5.

[4] S. P. Badwal, S. S. Giddey, C. Munnings, A. I. Bhatt, and A. F. Hollenkamp, "Emerging electrochemical energy conversion and storage technologies", *Frontiers in chemistry*, vol. 2, p. 79, 2014.

[5] S. C. Mueller, P. G. Sandner, and I. M. Welpe, "Monitoring innovation in electrochemical energy storage technologies: A patent-based approach", *Applied Energy*, vol. 137, pp. 537–544, 2015.

[6] Z. Yang, J. Zhang, M. C. Kintner-Meyer, *et al.*, "Electrochemical energy storage for green grid", *Chemical reviews*, vol. 111, no. 5, pp. 3577–3613, 2011.

[7] F. Mulder, B. Weninger, J. Middelkoop, F. Ooms, and H. Schreuders, "Efficient electricity storage with a battolyser, an integrated Ni-Fe battery and electrolyser", *Energy & Environmental Science*, vol. 10, no. 3, pp. 756–764, 2017.

[8] F. Mulder, "Implications of diurnal and seasonal variations in renewable energy generation for large scale energy storage", *Journal of Renewable and Sustainable Energy*, vol. 6, no. 3, p. 033 105, 2014.

[9] S. U. Falk and A. J. Salkind, "Alkaline storage batteries", 1969.

[10] B. Hariprakash, S. Martha, M. Hegde, and A. Shukla, "A sealed, starved-electrolyte nickel–iron battery", *Journal of Applied Electrochemistry*, vol. 35, no. 1, pp. 27–32, 2005.

[11] A. Ursua, L. M. Gandia, and P. Sanchis, "Hydrogen production from water electrolysis: Current status and future trends", *Proceedings of the IEEE*, vol. 100, no. 2, pp. 410–426, 2011.

[12] D. Zhou, Z. Cai, Y. Bi, *et al.*, "Effects of redox-active interlayer anions on the oxygen evolution reactivity of Ni-Fe-layered double hydroxide nanosheets", *Nano Research*, vol. 11, no. 3, pp. 1358–1368, 2018.

[13] B. J. Trześniewski, O. Diaz-Morales, D. A. Vermaas, *et al.*, "In situ observation of active oxygen species in Fe-containing Ni-based oxygen evolution catalysts: The effect of pH on electrochemical activity", *Journal of the American Chemical Society*, vol. 137, no. 48, pp. 15 112–15 121, 2015.

[14] O. Diaz-Morales, D. Ferrus-Suspedra, and M. T. Koper, "The importance of nickel oxyhydroxide deprotonation on its activity towards electrochemical water oxidation", *Chemical science*, vol. 7, no. 4, pp. 2639–2645, 2016.

[15] I. Faria, R. Torresi, and A. Gorenstein, "Electrochemical intercalation in NiOx thin films", *Electrochimica acta*, vol. 38, no. 18, pp. 2765–2771, 1993.

[16] M. Wehrens-Dijksma and P. Notten, "Electrochemical quartz microbalance characterization of Ni(OH)2-based thin film electrodes", *Electrochimica acta*, vol. 51, no. 18, pp. 3609–3621, 2006.

[17] D. M. Constantin, E. M. Rus, L. Oniciu, and L. Ghergari, "The influence of some additives on the electrochemical behaviour of sintered nickel electrodes in alkaline electrolyte", *Journal of power sources*, vol. 74, no. 2, pp. 188–197, 1998.

[18] J. D. Michael, E. L. Demeter, S. M. Illes, Q. Fan, J. R. Boes, and J. R. Kitchin, "Alkaline electrolyte and Fe impurity effects on the performance and active-phase structure of NiOOH thin films for OER catalysis applications", *The Journal of Physical Chemistry C*, vol. 119, no. 21, pp. 11 475–11 481, 2015.

[19] J. Zaffran, M. B. Stevens, C. D. Trang, *et al.*, "Influence of electrolyte cations on Ni(Fe)OOH catalyzed oxygen evolution reaction", *Chemistry of Materials*, vol. 29, no. 11, pp. 4761–4767, 2017.

[20] A. C. Garcia, T. Touzalin, C. Nieuwland, N. Perini, and M. T. Koper, "Enhancement of oxygen evolution activity of nickel oxyhydroxide by electrolyte alkali cations", *Angewandte Chemie International Edition*, vol. 58, no. 37, pp. 12 999–13 003, 2019.

[21] T. B. Reddy, *Linden's handbook of batteries*. McGraw-Hill Education, 2011.

[22] R. Barnard, C. Randell, and F. Tye, "Studies concerning charged nickel hydroxide electrodes i. measurement of reversible potentials", *Journal of Applied Electrochemistry*, vol. 10, no. 1, pp. 109–125, 1980.

[23] L. Trotochaud, S. L. Young, J. K. Ranney, and S. W. Boettcher, "Nickel–iron oxyhydroxide oxygen-evolution electrocatalysts: The role of intentional and incidental iron incorporation", *Journal of the American Chemical Society*, vol. 136, no. 18, pp. 6744–6753, 2014.

[24] P. Oliva, J. Leonardi, J. Laurent, *et al.*, "Review of the structure and the electrochemistry of nickel hydroxides and oxy-hydroxides", *Journal of Power Sources*, vol. 8, no. 2, pp. 229–255, 1982.

[25] M. W. Louie and A. T. Bell, "An investigation of thin-film Ni-Fe oxide catalysts for the electrochemical evolution of oxygen", *Journal of the American Chemical Society*, vol. 135, no. 33, pp. 12 329–12 337, 2013.

[26] A. Iranzo and F. Mulder, "Nickel-iron layered double hydroxides for an improved Ni-Fe hybrid battery-electrolyser", *Materials Advances*, vol. 2, no. 15, pp. 5076–5088, 2021.

[27] S. Jung, C. C. McCrory, I. M. Ferrer, J. C. Peters, and T. F. Jaramillo, "Benchmarking nanoparticulate metal oxide electrocatalysts for the alkaline water oxidation reaction", *Journal of Materials Chemistry A*, vol. 4, no. 8, pp. 3068–3076, 2016.

[28] T. Reier, M. Oezaslan, and P. Strasser, "Electrocatalytic oxygen evolution reaction (OER) on Ru, Ir, and Pt catalysts: A comparative study of nanoparticles and bulk materials", *Acs Catalysis*, vol. 2, no. 8, pp. 1765–1772, 2012.

[29] C. C. McCrory, S. Jung, I. M. Ferrer, S. M. Chatman, J. C. Peters, and T. F. Jaramillo, "Benchmarking hydrogen evolving reaction and oxygen evolving reaction electrocatalysts for solar water splitting devices", *Journal of the American Chemical Society*, vol. 137, no. 13, pp. 4347–4357, 2015.

[30] A. C. Garcia, T. Touzalin, C. Nieuwland, N. Perini, and M. T. Koper, "Enhancement of oxygen evolution activity of nickel oxyhydroxide by electrolyte alkali cations", *Angewandte Chemie International Edition*, vol. 58, no. 37, pp. 12 999–13 003, 2019.

[31] B. S. Yeo and A. T. Bell, "In situ raman study of nickel oxide and gold-supported nickel oxide catalysts for the electrochemical evolution of oxygen", *The Journal of Physical Chemistry C*, vol. 116, no. 15, pp. 8394–8400, 2012.

[32] M. Cappadonia, J. Divisek, T. von der Heyden, and U. Stimming, "Oxygen evolution at nickel anodes in concentrated alkaline solution", *Electrochimica acta*, vol. 39, no. 11-12, pp. 1559–1564, 1994.

[33] D. S. Hall, D. J. Lockwood, C. Bock, and B. R. MacDougall, "Nickel hydroxides and related materials: A review of their structures, synthesis and properties", *Proceedings of the Royal Society A: Mathematical, Physical and Engineering Sciences*, vol. 471, no. 2174, p. 20 140 792, 2015.

[34] D. Lei, D.-C. Lee, A. Magasinski, E. Zhao, D. Steingart, and G. Yushin, "Performance enhancement and side reactions in rechargeable nickel–iron batteries with nanostructured electrodes", *ACS Applied Materials & Interfaces*, vol. 8, no. 3, pp. 2088–2096, 2016.

[35] J. O. G. Posada and P. J. Hall, "The effect of electrolyte additives on the performance of iron based anodes for Ni-Fe cells", *Journal of The Electrochemical Society*, vol. 162, no. 10, A2036, 2015.

[36] S. Hills, "Beneficial effect of lithiated electrolyte on iron battery electrodes", *J. Electrochem. Soc*, vol. 112, no. 10, pp. 1048–1049, 1965.

5

EFFECT OF FLOW IN AN INTEGRATED BATTERY AND ELECTROLYSER SYSTEM- A PRELIMINARY EXPERIMENTAL STUDY

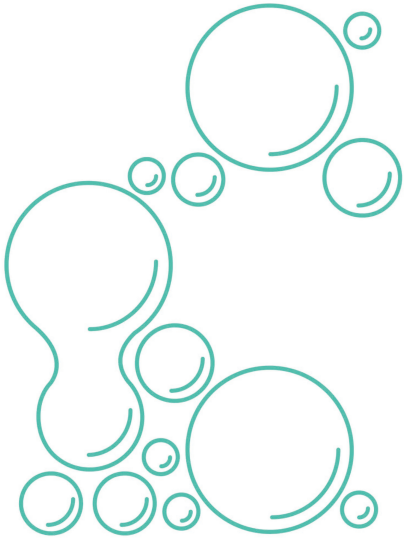

5.1. INTRODUCTION

INCREASINGLY ambitious EU net-zero emissions targets, together with worldwide population growth requires a widespread increase in renewable energy penetration. To increase the percentage of renewables in the grid, new technological developments in large-scale energy storage are required [1][2][3]. Currently, there are many electrochemical energy storage technologies that could potentially supply this need. These technologies include flow batteries, fuel cells, and electrolysers[4][5][6].

Batteries can be used to bridge the gap between renewable energy production and short term storage capacity, while hydrogen can be used for longer-term storage. An integrated battery and electrolyser system can combine both long-term and short-term storage capacity[7] [8].

The battolyser -an integrated battery and electrolyser system- functions as a battery during charging, and when fully charged splits water from the KOH electrolyte, functioning as an alkaline electrolyser. The NiOOH and Fe electrodes act as OER and HER catalysts when fully charged.

The integration of both technologies presents an optimization exercise, as both electrolysers and batteries are operated at specific conditions. One conflicting operating parameter is the use of electrolyte flow on the electrode surface. Batteries typically do not use electrolyte flow, however most electrolysers integrate electrolyte flow into the system. Specifically in alkaline water electrolysis, the major efficiency losses are due to the presence of bubbles on the surface of the electrodes[9]. One way to avoid bubble accumulation is to include convection in the electrolyte gap. Therefore, the use of flow field patterns can benefit bubble removal, mass transfer limitations, product removal, and heat management[10]. As the electrodes of the battolyser are thick and porous, including flow could facilitate charge and discharge processes in the active material of the battery, increasing mass transfer mechanisms inside the electrodes. In the electrolyser mode, adding electrolyte flow could benefit in bubble mitigation, minimizing losses typically seen in alkaline electrolysers.

The design of the flow field patterns determines the current distribution and the pressure drop in the cell. Serpentine channels are typically used to evenly distribute the reacting fluid, however they can cause stagnation when cross flow occurs. Nagai et al[11] studied the optimum electrode gap for alkaline electrolysis in no flow conditions. They report an optimum gap thickness of 1-2 mm in alkaline electrolysis setups. When using flow, the optimum inter-electrode gap decreases significantly. The electrode gap has an inverse proportionality with the electrolyte flow rate[12].

Flow field designs including serpentine flow fields (SFF), parallel flow fields (PFF) and interdigitated flow fields (IFF), as shown in Figure5.3 have been investigated to improve the performance of redox flow batteries[10]. 3D printing has been used in other studies because of the ability of rapid prototyping of different cell configurations[13]. Here, we have used 3D printed prototypes to design and build a flow setup to study the effect of serpentine flow field and parallel flow fields on an integrated battery and electrolyser system.

5.2. EXPERIMENTAL METHODS

5.2.1. CELL DESIGN AND SETUP

The experimental flow cell was designed to for flexible operation of different flow fields and flow rates. Five essential requirements for an optimal operation include:

- To provide a uniform distribution of the reactants and products over the active electrode surface
- High mechanical strength for stack integrity
- Impermeability to product gases
- Chemical resistance to highly concentrated KOH electrolyte
- Resistance to corrosion and long lifetime

A flow cell was designed, prototyped, and built to test different flow field patterns (FFP). The initial designs were made in SolidWorks and prototyped by 3D printing. A prototype is made using the 3D printing technology Low Force Sterolithography (LFS) using a Clear V4 resin that allows for 0.1 mm precision. A Formlabs Form 3+ SLA Printer was used which allows for rapid iterations of design modifications to develop a prototype cell. After the design was tested and modified to avoid leakages, a final cell was manufactured in PMMA. PMMA was chosen because of its high stability in highly concentrated KOH solutions. The design was modified slightly to make it possible to machine in PMMA, as the precision is larger than the 3D printing precision. 1 mm silicone gaskets are fit to avoid leakage. The electrodes are connected with nickel wire (ALFA 0.5mm diameter, annealed, 99.98% (metals basis)) and epoxy (RESION Resin Technology EP101) is used to avoid leakage through the electric connections.

The cell is a stack of plates, including gaskets between every plate and put together with pressure from bolts on 6 points.

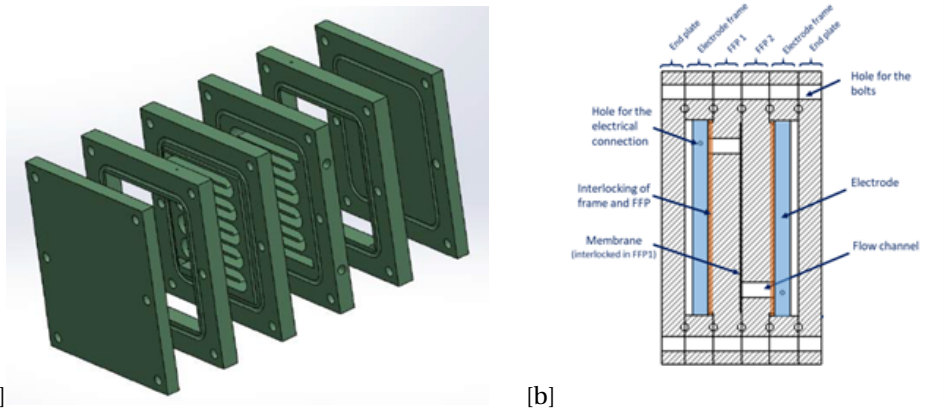

[a] [b]

Figure 5.1: Schematic view of the flow cell designed and built for this study, (a) exploded view of the serpentine flow field design and (b) stacked cell.

The cell consists of 6 frames: 2 end plates, 2 electrode frames, and 2 flow field plates. Drawings of the designed plates are presented in Appendix A. Three different flow field plates are fabricated: a serpentine, parallel and free flow field. Each FFP has an inlet and outlet connection on the side. The size of each flow field plate is defined by the size of the commercial electrodes available. Commercial Ni-Fe batteries used were purchased from Ironcore Batteries. Dimensions of all the cell components are included in Appendix C.

5.2.2. EXPERIMENTAL TESTS

A peristaltic pump (RotaLab LongerPump BT100-1L Peristaltic Pump) was used to pump the 5 M KOH (85%, Merck) in ultrapure water (MilliQ IQ 7000, 18.2 MΩ) liquid electrolyte through the cell. A BT Biologic Battery Charging station (type) was used to provide the current to perform the charge/discharge cycles. The electrodes were tested before assembly and a typical charge/discharge cycle is presented in Appendix C.

Three different flow field plates were tested at three different flow rates and at no flow. The flow plates were filled with 200 ml electrolyte and pumping started before charging and discharging the battery electrodes. The amount of hydrogen gas produced during the measurement was not measured.

5.3. RESULTS AND DISCUSSION

5.3.1. EFFECT OF THE GAP AND THE MEMBRANE

Preliminary COMSOL Multiphysics simulations to determine the effect of electrolyte flow on the battolyser device indicated that the benefits of including flow were relatively small. The model is comprehensively described in Chapter 3 of this thesis. However, the limitations of the study were considerable, as the model solves only for 1 dimension cutting across the electrodes and the gap, across the thickness of the cell.

One of the design limitations to enable flow in the battolyser setup is the necessity to include a thicker electrolyte gap. This will result in a high ohmic drop through the gap, thereby increasing the cell potentials. The effect of the Zirfon PERL membrane can be seen in Figure 5.2, where a measurement with one empty FFP with no separator is compared to a measurement with an empty FFP with a separator. Using the separator results in a higher discharge potential than the standard setup with the separator. Possible explanations for the higher resistance than reported for highly conductive Zirfon membranes[14] are unevent current distribution and the presence of bubbles.

The effect of the electrolyte gap is constant in all the flow field setups as all the FFPs have the same thickness. However, this has to be taken into account when comparing the results with a no-gap or smaller gap cell.

5.3.2. EFFECT OF THE SHADOWED AREA

When comparing the different flow field designs it is important to take into account the different shadowed area. Ideally the design of all the flow fields would be on the same shadowed area plates. However, in practice this is not possible. To allow for machining and physical stability of the flow field plates, the shadowed area, the area where PMMA material separates one electrode from the other, is different when switching from one plate to another. Therefore, it is important to mention that the FFPs allow for a different

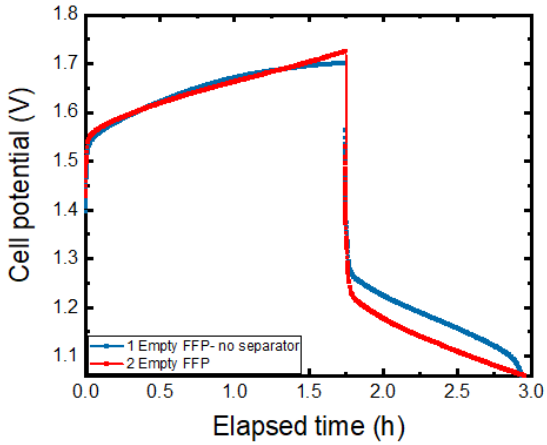

Figure 5.2: Charge/discharge curve of the battolyser flow setup with one empty FFP vs. 2 empty FFPs and a separator.

effective electrode area. This can be clearly seen in Figure 5.4, from which the open area is calculated. Therefore, comparing the charging and discharging potential might not be straightforward.

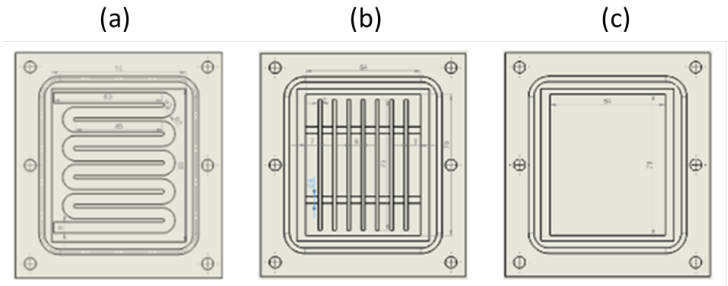

Figure 5.3: Schematic view of the flow field pattern (FFP) designs; a) Serpentine pattern, b) Parallel pattern, c) Empty pattern.

As the batteries are charged and discharged at a constant current, it is challenging to compare the effects of the changing effective electrode area. Although all 3 runs were done with the same electrode that had been activated and with the same battery capacity, they do not reach the electrolysis potential for all three. Further experiments could be run at a constant potential to study the effects of current relative to the effective electrode area. With the data measured, it is challenging to compare the FFPs among themselves. However, we can compare the different flow field velocities chosen in a specific flow field plate. From Figure 5.2 it is clear that there is a linear relationship relating shadowed area and charge/discharge potential, which is related to the efficiency of the device. In an ideal situation, to avoid charging and discharging losses, we want to charge the device at

the lowest possible potential and discharge at the highest possible potential. Because of the kinetic limitations, charge and discharge will never be at the same potential, but to optimize the energetic efficiency, the aim is to get as close as possible. Furthermore, the potential of the highest point in the charging curve is related to the potential at which hydrogen gas is produced, and therefore we would also like to maintain this value as low as possible. This is more closely linked to the overpotentials related to the kinetics of the battery material towards oxygen evolution.

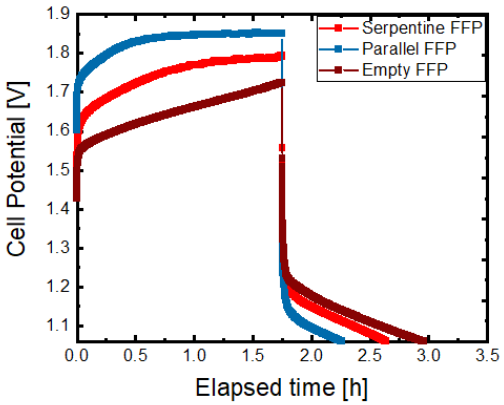

Figure 5.4: Charge/discharge curve of the battolyser flow setup with different FFPs without flow.

5.3.3. COMPARING DIFFERENT FLOW FIELD PATTERNS

If we compare the empty flow field pattern, which has the lowest relative shadowed area we see that there is a small advantage in the discharge potential when using a flow field. In Figure 5.5 we see that there is only a small difference among the three different flow speeds, however, the charging potential is higher for the experimental runs that include flow. It is possible that the production of gas bubbles during the charging process causes enough convective flow to avoid concentration overpotentials, and therefore there is no added benefit during charging when using flow. However, this effect is lost during the discharging stage, and therefore we observe a small benefit in the discharging potentials when using any speed of flow.

From Figure 5.6 we can see that for both the serpentine flow field pattern and the parallel flow field pattern there is no noticeable difference with flow and without. It is possible that the ohmic losses, because of the large gap added to the high percentage of shadowed area, are the major contributions for losses in the cell. Therefore, it is not possible to observe any benefit from flowing the electrolyte and developing a more constant concentration throughout the electrode gap. Because of this it is necessary to further develop more optimized cells to test different flow conditions. Further experiments should be done where the gap thickness and the shadowed area by the FFPs are not the major contributors to loss mechanisms in the charge/discharge process. To do this, it is necessary to totally redesign the cell and reposition the inlet and outlet streams so that the

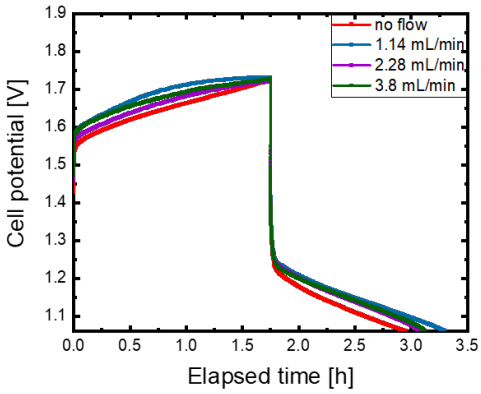

Figure 5.5: Charge/discharge curve of the battolyser flow setup with the Empty flow field pattern at different flow field rates.

cell design is not constrained by the minimum fitting diameters.

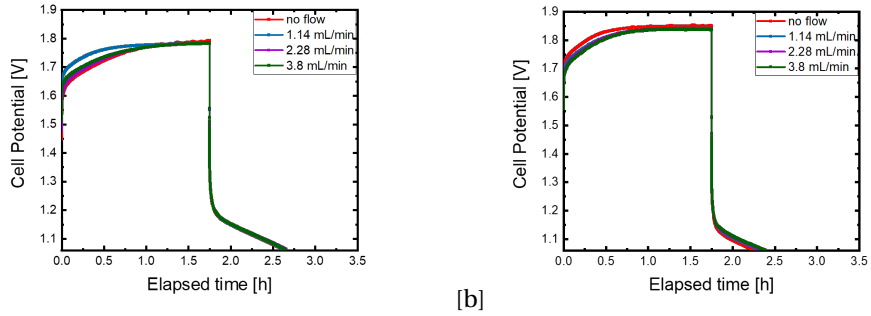

Figure 5.6: Charge/discharge curve of the battolyser flow setup with the (a) serpentine and (b) parallel flow field pattern at different flow field rates.

Cross flow can be another limitation in the battolyser setup. Because of the highly porous electrode materials, it is possible that at high pressure drops the electrolyte flows through the electrodes across the cell. This can result in stagnation in the serpentine and parallel flow channels. Cross flow would happen when electrolyte can flow through the electrode, from the back side toward the gap. This would interfere with bubble formation and cause high pressure drops across the whole system.

In Figure 5.7 we can see that even only one FFP with no membrane is too large of a gap to observe the effect of different flow field speeds. Although not many differences can be observed, we see a drop in battery capacity at the higher flow speeds. To further understand the effect of flow and how different flow fields affect both the battery and the electrolyser function, a new setup has to be designed. Because of this, the setup has to be replaced and modifed to allow for a smaller gap.

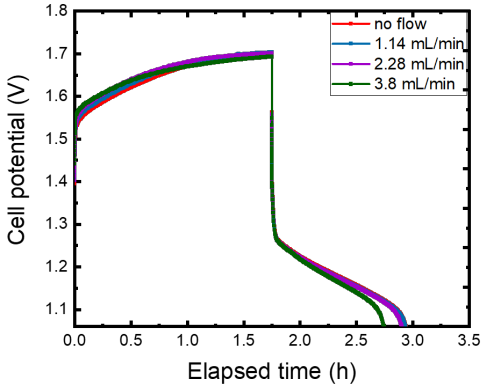

Figure 5.7: Charge/discharge curve of the battolyser flow setup with the serpentine flow field pattern at different flow field rates with one serpentine FFP and no membrane.

5.4. CONCLUSIONS

One of the major conclusions is that it is important to have comparable effective areas in different configurations to compare the effect at different conditions. This might be difficult to achieve in the current setup, but could be designed for in future experiments. To achieve comparable charge and discharge curves, similar current densities per effective area are required. Furthermore, it would be interesting to study gas production, as this could include more details on what is happening in the setup. In 5.4, we observe that although these electrodes were charged for the same amount of time and at the same current, they have not all reached the plateau at which gas evolution takes place. If the experimental setup allowed for gas collection we could confirm this is the case. Other observations that can affect current distribution in the cell include gas buildup and liquid levels in the cell. Gas buildup is not expected in a gap as large as the one present in the cell designed, however, it is possible that inside the electrodes bubbles have accumulated and limit the active surface area, affecting the current density and thus the reaction rate. Liquid levels in the cell proved to be difficult to stabilize, and at some flow speeds varied significantly. This can affect the active surface area, causing an increase in potential. Although the preliminary experiments cannot be used to bring about conclusions on the basis of this study, they serve as a starting point to develop further experiments that can help elucidate the combined effects on an integrated device. Some of the recommendations for future experiments include the following.

5.4.1. FURTHER EXPERIMENTS

More experiments are necessary to further dive into the effects of liquid flow in the Battolyser setup. This setup has some technical limitations, such as the large ohmic gap and the electrode contacts that have to be addressed to further study the effect of the flow field on the battery charge/discharge processes. The limitations of the thickness of the plates come from the fittings used to provide electrolyte flow. As these are the

smallest fittings, the flow plates cannot be made thinner. The setup has to be completely redesigned, where the electrolyte flow is connected in a different way to the setup. Because of the thickness of the electrodes, the connection was not put on the end plates, however this might be the only alternative. In the future, it would be ideal to measure gas production during charging and discharging.

Furthermore, the flow of highly alkaline electrolyte is hazardous, and it was difficult to obtain a leak-tight cell. As this setup is quite bigger than typically bench-scale experiments, the amount of highly concentrated KOH is significantly larger. If this could be done in a safer way for lab users it would be beneficial. It would also improve the quality of the study to quantify the gases produced, and detail the coulombic and energetic efficiency of the device, including the energy requirements of the pump.

A more detailed model, including the effects of bubbles and two phase flow could provide some more details on the effects of flow in thick battery electrodes.

BIBLIOGRAPHY

[1] IRENA, "Electricity storage and renewables: Costs and markets to 2030", 2017.

[2] S. P. Badwal, S. S. Giddey, C. Munnings, A. I. Bhatt, and A. F. Hollenkamp, "Emerging electrochemical energy conversion and storage technologies", *Frontiers in chemistry*, vol. 2, p. 79, 2014.

[3] R. A. Huggins, *Energy storage*. Springer, 2010, vol. 406.

[4] H. Beltran, S. Harrison, A. Egea-Àlvarez, and L. Xu, "Techno-economic assessment of energy storage technologies for inertia response and frequency support from wind farms", *Energies*, vol. 13, no. 13, p. 3421, 2020.

[5] H. A. Behabtu, M. Messagie, T. Coosemans, *et al.*, "A review of energy storage technologies' application potentials in renewable energy sources grid integration", *Sustainability*, vol. 12, no. 24, p. 10 511, 2020.

[6] A. S. Lord, "Overview of geologic storage of natural gas with an emphasis on assessing the feasibility of storing hydrogen.", Sandia National Laboratories, Tech. Rep., 2009.

[7] F. M. Mulder, *Hybrid battery and electrolyser*, WO2016178564A1, 10 2016. [Online]. Available: https://patents.google.com/patent/WO2016178564A1/und.

[8] F. Mulder, B. Weninger, J. Middelkoop, F. Ooms, and H. Schreuders, "Efficient electricity storage with a battolyser, an integrated Ni-Fe battery and electrolyser", *Energy & Environmental Science*, vol. 10, no. 3, pp. 756–764, 2017.

[9] M. David, C. Ocampo-Martınez, and R. Sánchez-Peña, "Advances in alkaline water electrolyzers: A review", *Journal of Energy Storage*, vol. 23, pp. 392–403, 2019.

[10] Y. Zeng, F. Li, F. Lu, *et al.*, "A hierarchical interdigitated flow field design for scale-up of high-performance redox flow batteries", *Applied energy*, vol. 238, pp. 435–441, 2019.

[11] N. Nagai, M. Takeuchi, T. Kimura, and T. Oka, "Existence of optimum space between electrodes on hydrogen production by water electrolysis", *International journal of hydrogen energy*, vol. 28, no. 1, pp. 35–41, 2003.

[12] R. S. Jupudi, H. Zhang, G. Zappi, and R. Bourgeois, "Modeling bubble flow and current density distribution in an alkaline electrolysis cell", *The Journal of Computational Multiphase Flows*, vol. 1, no. 4, pp. 341–347, 2009.

[13] J. R. Hudkins, D. G. Wheeler, B. Peña, and C. P. Berlinguette, "Rapid prototyping of electrolyzer flow field plates", *Energy & Environmental Science*, vol. 9, no. 11, pp. 3417–3423, 2016.

[14] M. T. de Groot and A. W. Vreman, "Ohmic resistance in zero gap alkaline electrolysis with a zirfon diaphragm", *Electrochimica Acta*, vol. 369, p. 137 684, 2021.

6

Conclusions and Recommendations

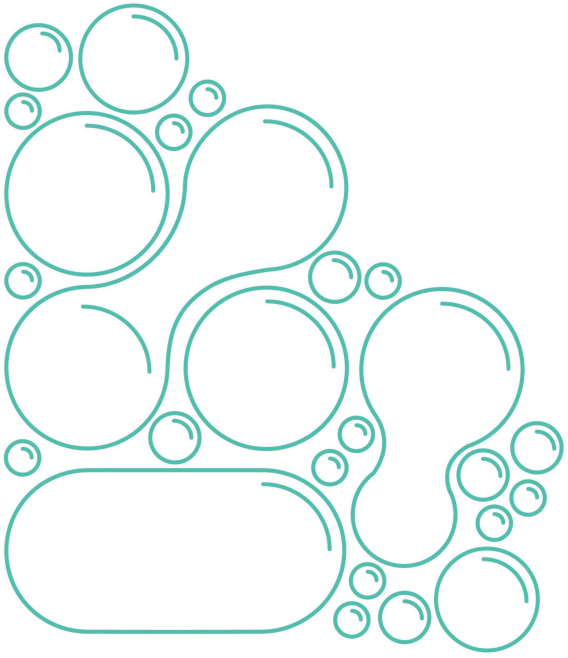

6.1. CONCLUSIONS

In this dissertation, a combined experimental and modelling approach has been developed to further study and understand the working parameters of an integrated battery and electrolyser device. Parameters including the cell design and setup were optimized by means of a COMSOL Multiphysics 1D model. Further experimental studies include the effect of different alkali metal cations in the electrolyte to further optimize the integrated device. A final study on the effect of flow fields and flow velocities provides a starting point for further experiments to better understand the effect on the integration of both functionalities, namely electrolysis and battery storage.

In Chapter 3, a model was developed to optimize the unit cell energy efficiency of the battolyser. The model includes the electrochemical reactions related to battery charging and discharging, electrochemical reactions of hydrogen and oxygen production, transport mechanisms through the electrolyte gap, membrane and porous electrodes, and effective diffusivity and conductivity inside the porous electrodes. We validated the model with experimental results. Using the simulation results we showed that the optimum electrode thickness is smaller than that of the commercial Ni-Fe battery electrodes used, 0.75 times the commercial electrode thickness, corresponding to an electrode thickness of 3 mm for the nickel electrode and 2.25 mm for the iron electrode. Optimizing for the porosity of the electrodes we found that the optimum range of electrode void fraction lies between 0.15 – 0.35. Both modifications result in a combined overall efficiency of 86%, compared to a base-case efficiency of 80%.

The electronic resistance from the electrode material and battery capacity are the main limitations of the battolyser design. Battery electrodes are comparatively orders of magnitude thicker than those used in alkaline electrolysis. Therefore, the optimization of the integrated device is a complex process with many trade-offs and depends on application demands. Depending on the application profile of the device and the main product required – being hydrogen or electricity – the system can easily be optimized by running these simulations.

For a combined approach where both battery storage and hydrogen production are used, an optimized cell design was obtained by modifying the electrode thickness and porosity. Electrolyte conductivity and gap width were also optimized. However, due to the high ionic conductivity of the electrolyte and limited current density, the effect is negligible.

In Chapter 4, we have investigated the effect of alkali hydroxide additions to concentrated KOH electrolytes on the OER performance and battery capacity of nickel electrodes. We show that the addition of different metal alkali cations has an effect on the electrochemical performance of the nickel electrode, both with regards to battery capacity and OER activity. For OER activity, the trend found during RDE setup experiments in high concentration hydroxide electrolytes is Rb^+>Cs^+ >K^+>Na^+>Li^+. This is possibly due to the size effect of the different cations, as smaller cations, such as Li^+, can intercalate in the NiOOH-LDH and stabilize the γ-NiOOH phase. This results in a higher onset potential for OER. For the larger cations, Rb^+ and Cs^+, we find that only large additions (of 1 M or 0.5 M) cause a significant decrease in OER potential.

The intercalation of small cations also causes an increase in battery electrode capacity because of the higher average valence of the $Ni(OH)_2$ /NiOOH α/γ pair. Small con-

centrations of Li^+ added to a concentrated KOH electrolyte can therefore be beneficial for the nickel electrode battery functionality and for an integrated battery and electrolyser system, where it increases the battery capacity without a significant increase in OER onset potential. Further experiments with NiFe batteries at longer time scales show that the effect of lithium inclusions in the nickel electrode are still present in the battery capacity for at least 30 cycles after the electrolyte has been changed to pure KOH.

For an integrated device, with both battery and electrolyser functionality, we find that the optimum electrolytes are either a 0.05 M LiOH + 6.45 M KOH electrolyte or a 0.05 M RbOH + 6.45 M KOH electrolyte, as these result in a higher battery capacity and lowest cell potentials for gas evolution.

Finally, in Chapter 5 a flow cell was designed and built by using 3D printing technology for quick iterations of design modifications. Although the preliminary experiments cannot be used to bring about conclusions on the basis of this study, they serve as a starting point to develop further experiments that can help elucidate the combined effects on an integrated device. Some of the recommendations for future experiments include the following section.

6.2. RECOMMENDATIONS

An integrated battery and electrolyser device presents the challenge of optimizing two separate functionalities. Because of the two functionalities coexisting, the device can be tailored to the specific application. Therefore, an upscaled battolyser will be dependent on the application required. The studies performed for this dissertation provide a better understanding of the operating parameters. Further experiments and recommendations are detailed in this section.

The model developed is applicable to many different setups and can be tailored to different operational parameters. At low current densities, it can be used to explain phenomena and design an upscaled unit cell. Because of the simplifications and operation at low current densities, the COMSOL Multiphysics 1D model developed is useful to understand the effect of cell parameters on the overall efficiency of the device. However, it would be interesting to include 2, or even 3 dimensions in the study to study the effects of fluid dynamics and bubbles. At high current densities, bubbles can generate additional resistance on the surface of the electrodes, and would therefore be important to include. The disadvantage of this is that the model would be computationally very expensive, and running simulations would take considerable amounts of time. However, including bubble effects in the model could further explain the effects of gap thickness and provide insight for further optimization.

The addition of alkali metal cations in highly concentrated electrolytes in concentrated KOH was studied here. Further experiments including in-situ surface enhanced Raman could help explain the effects of the $Ni(OH)_2$ /NiOOH crystal structure and how the alkali metal cations interact. Regarding the large-scale battery experiments, long-term experiments including gas production could provide more information on the energetic efficiency of the setup and the effect of the electrolyte here.

More experiments are necessary to further dive into the effects of liquid flow in the Battolyser setup. This setup has some technical limitations, such as the large ohmic gap and the electrode contacts that have to be addressed to further study the effect of the

flow field on the battery charge/discharge processes. The limitations of the thickness of the plates come from the fittings used to provide electrolyte flow. As these are the smallest fittings, the flow plates cannot be made thinner. The setup has to be completely redesigned, where the electrolyte flow is connected in a different way to the setup. Because of the thickness of the electrodes, the connection was not put on the end plates, however this might be the only alternative.

Furthermore, the flow of highly alkaline electrolyte in a flow through design of the battolyser is hazardous, and it was difficult to obtain a leak-tight cell. As this setup is quite bigger than typically bench-scale experiments, the amount of highly concentrated KOH is significantly larger. If this could be done in a safer way for lab users it would be beneficial. It would also improve the quality of the study to quantify the gases produced, and detail the coulombic and energetic efficiency of the device, including the energy requirements of the pump.

Integrating the recommendations for Chapter 3 and Chapter 5 would be beneficial for the optimization of a large-scale battolyser. A more detailed model, including the effects of bubbles and two phase flow could provide some more details on the effects of flow in thick battery electrodes.

A

APPENDIX CHAPTER 3

A.1. MODEL PARAMETERS

The kinetic and thermodynamic parameters that were used in the simulations are detailed in this section.Further information on parameters that were measured experimentally can be found in the following sections.

The kinetic and thermodynamic parameters of the $Ni(OH)_2$ electrode are from Paxton and Newman[1] and are presented in Table A.1. Sinha [2] measured these kinetic parameters in different electrolyte concentrations. Paxton and Newman took this data and made a fit to the general Butler-Volmer equation to determine the average values. These average values were used in the presented model.

Table A.1: Kinetic parameters for the battery charging reactions for $Ni(OH)_2$ from [1].

i_0	$1.04x10^{-4} A/cm^2$
α_a	0.13
α_c	0.074

The equilibrium potential of $Ni(OH)_2$ is taken as dependent on the state of charge of the electrode. Conway and Gilead have shown that the nickel electrode is a mixed potential electrode due to the effect of OER at higher states of charge[3].

A

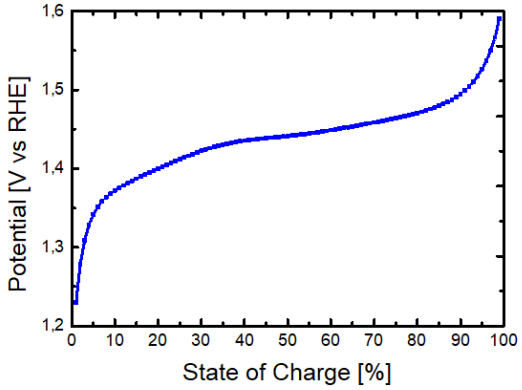

Figure A.1: Standard electrode potential of the nickel hydroxide positive electrode dependent on state of charge of the battery[1].

The iron electrode, on the other hand is considered to have a constant potential throughout the charging process and the material consists of two different phases with a standard electrode potential of -0.164 V vs RHE. The kinetic parameters of the iron electrode have been used to calculate the onset potential of the integrated battery and electrolyser system, with an exchange current density of 0.003 A/m^2 and anodic and cathode coefficients of 0.5.

The kinetic parameters of the gas production reactions are presented in Table A.2 .

Table A.2: Kinetic parameters for the gas production reaction (OER and HER) on both electrodes.

	OER	HER
E^0	1.23 V vs RHE	0 V vs RHE
i_0	0.00005 A/m^2	0.0003 A/m^2
α_a	0.45	0.5
α_c	0.5	0.5

Table A.3: Parameter values used- base case scenario.

Parameter	Value	Units
Nickel electrode thickness	4	[mm]
Iron electrode thickness	3	[mm]
Gap thickness	3	[mm]
Membrane thickness	0.5	[mm]
Membrane porosity	0.5	
Electrode porosity	0.5	
Temperature	293.15	[K]
Electrolyte concentration	5	[mol/L]
Electrolyte diffusion coefficient	3.75×10^{-9}	[m2/s]

A

A.2. SEM IMAGES OF ELECTRODE PARTICLES

SEM imaging and EDX were performed using a JEOL JSM 6500F microscope.

With regards to the nickel material used in the positive electrode, SEM images are presented in Figure A.2(a). As can be seen in this Figure, the particle size distribution is quite broad. Using EDX, the large particles are identified as graphitic carbon. The graphite particles are approximately 5 times larger than the active material nickel particles. Nickel particle size ranges from 30 μm to only a few μm. The average particle size for the nickel material is 2.3 μm.

For the iron electrode presented in Figure A.2 (b), it can be observed that the iron particle size distribution is more narrow. The larger particles in the image are graphitic carbon, identified by EDX. The iron particles are more similar in size, and also smaller than the nickel hydroxide particles in the nickel electrode. The average iron particle size is 2 μm.

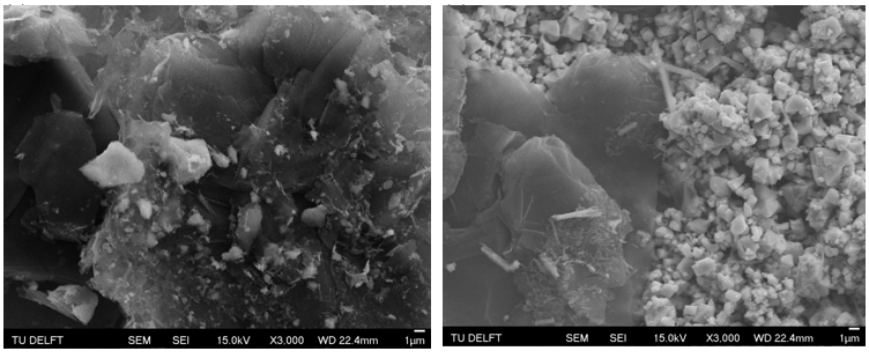

Figure A.2: SEM-SEI images of the active electrode material. (a) Nickel positive electrode material and (b) Iron negative electrode material.

A.3. XRD OF ELECTRODE MATERIALS

XRD analysis was done using a Bruker D2 PHASER. The results were analyzed using the DIFFRAC SUITE software package.

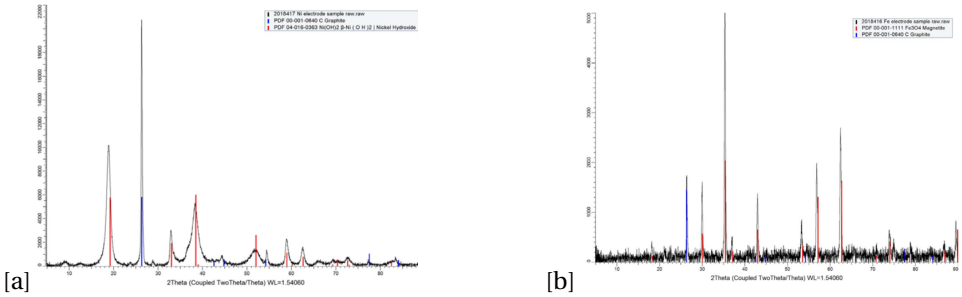

Figure A.3: . XRD analysis of the active electrode material. (a) Nickel positive electrode material, where the red lines indicate the peaks associated with β- $Ni(OH)_2$ and the blue lines are related to graphitic carbon peaks and (b) Iron negative electrode material, where the red lines indicate peaks associated with magnetite Fe3O4 and the blue lines are again related to the graphitic carbon content.

This confirms the main composition of the Nickel positive electrode material as graphite and β- $Ni(OH)_2$. The XRD diffraction pattern of the iron active material is presented in Figure A.3. This confirms that there is also graphite present in the sample and the iron material is present in magnetite (Fe_3O_4) form. This is due to a self-discharging mechanism because of the stability of the material in air.

A

A.4. BET SURFACE AREA CALCULATION

Brunauer-Emmett-Teller (BET) theory serves as the theoretical basis for a standard specific surface area measurement technique. The analysis uses multilayer adsorption with probing gases that do not chemically react with the material surfaces to quantify the specific surface area. Nitrogen was used, and therefore the analysis is conducted at the boiling temperature of N_2. A Gemini VII 2390p analyzer was used to perform this technique. The surface area was measured via BET analysis, and the adsorption isotherm is presented in Figure A.4. This is a straight line as expected.

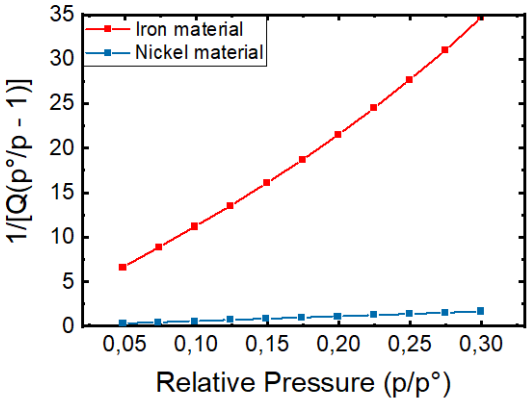

Figure A.4: BET surface area plot for the nickel and iron materials.

For the nickel electrode material, the specific surface area obtained is 17.99 m^2/g. The BET surface area measured is approximately 50 times larger than the area calculated for a packed bed of spherical particles with a diameter equal to the average particle.

For the iron electrode material, the specific surface area obtained is 0.88 m^2/g. The BET area calculated is less than two times as large as that of the theoretical calculation. By this measurement, the iron active material is less porous than the nickel material.

A.5. ELEMENTAL COMPOSITION OF THE ELECTRODE MATERIALS

Inductively Coupled Plasma Optical Emission Spectroscopy (ICP-OES) was used as an analytical technique to determine the elemental composition of a sample. Samples are dissolved in H_2O_2 and digested close to boiling point for 4 hours. Then the samples were diluted in 3 v% HNO_3. This liquid is injected in the form of aerosol into an argon plasma. The plasma excites the atoms and ions, causing them to emit electromagnetic radiation at a particular wavelength characteristic to a particular element. The intensity of the emission is proportional to the concentration of the element.

The elemental composition of the active material inside the pockets was obtained by ICP-OES analysis. The electrode pockets were opened and the compacted material was extracted. The results are presented in Table A.4.

Table A.4: ICP-OES results for the nickel and iron electrode sample

Element	Nickel Electrode Mass percentage [%]	Iron Electrode Mass percentage [%]
Fe	0.100	98.193
Ni	93.253	0.252
Al	0.012	0.032
SO_4^{-2}	0.146	0.191
Li	4.636	0.017
Na	4.636	1.094
Zn	0.037	0.056
Si	0.062	0.065
PO_4^{-2}	0.102	0.046
Cd	0.013	0.013
Sn	0.013	0.038
Ca	0.022	-
Ti	-	0.004
Ba	-	1.447

Due to the dilution process, carbon is not included in ICP-OES analysis results. The nickel hydroxide positive electrode, as expected, is composed mainly of nickel. Some iron is also present in the nickel electrode. This can be due to crossover during charging and discharging cycles because of the solubility of iron in KOH. This is expected as the sediment found in the bottom of the battery has a high mass percentage of iron. The iron crossover can decrease the overpotential for oxygen evolution in NiOOH materials[4]. Lithium and sodium can be present because of the use of LiOH and NaOH in the KOH electrolyte during previous battery cycles. The role of different cations in the nickel hydroxide structure is not yet well understood. Zn, Cd, and Sn are typical HER inhibitors, and are believed to have been added to the iron electrode to avoid the secondary reaction. Cadmium and cobalt are used as additives to the nickel hydroxide electrode to increase the conductivity and the oxygen evolution potential.

A

A.6. EXPERIMENTAL SETUP FOR VALIDATION

The experimental setup used for validation tests is composed of a commercial battery setup. A schematic representation is presented in Figure A.5 (a).

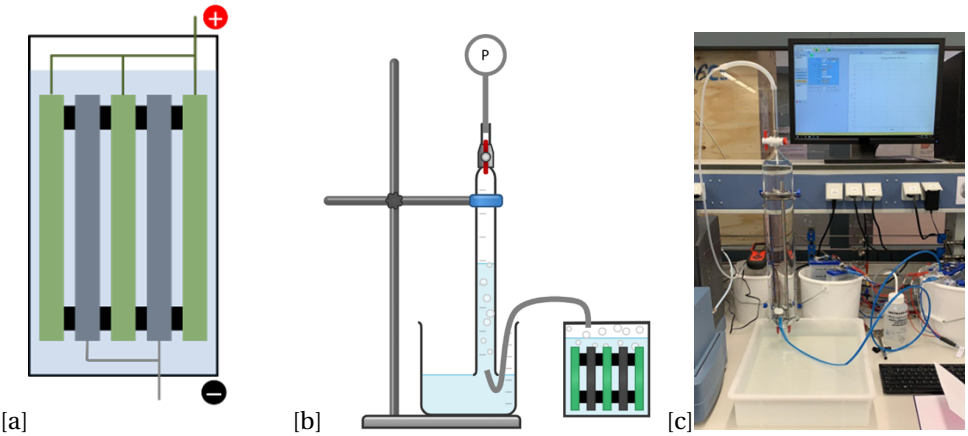

[a] [b] [c]

Figure A.5: (a) Commercial battery setup including: 3 positive nickel electrodes (in green), 2 negative iron electrodes (in grey), alkaline electrolyte and rubber separators (black) to avoid short-circuits. The cell is encased in a plastic casing with metal connectors for the positive and negative electrodes. (b) Schematic of the reverse burette experimental setup to measure the total gas production (c) Experimental setup used to measure total gas production.

A schematic representation of the experimental setup used to measure gas production is presented in Figure A.5 (b) and A.5 (c). Before the charging cycle the system was flushed with Argon gas. After charging the battery, samples of the collected gas were taken and the composition determined in a microGC. The microGC model is Varian μ -GC CP4900, with a 1 m CP-COX column and a TCD detector. The carrier gas is Argon.

The volume of gas produced was measured every 15 minutes. The total gas production results are shown in Figure A.6. The volumetric percentage of hydrogen in the gas collected is 60% according to the measurement with a microGC.

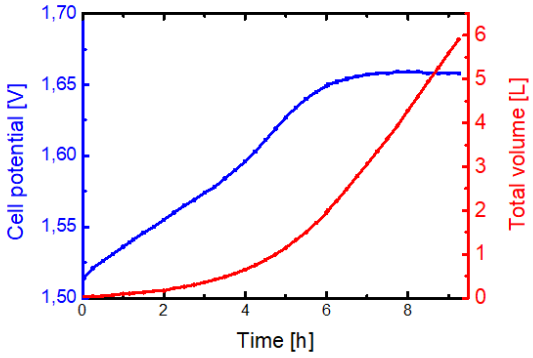

Figure A.6: Cell potential vs. elapsed time during a charging gas production cycle

During the first 6 hours of the measurement, when the cell potential is still increasing the battery is charging. Therefore, the catalysts for HER/OER are still being produced inside the battery electrodes. After this time, the battolyser functions in electrolysis mode and the total volume produced is expected to be linear, as shown in the measurement above.

The relationship between total gas produced versus elapsed time is only linear when the battery is fully charged and the amount of gas produced is constant. Therefore, before the time when the electrodes are fully charged the relationship is not expected to be linear, as the catalysts for HER/OER are being produced on both electrodes.

A

A.7. MODEL VALIDATION AT DIFFERENT CHARGING RATES

To further validate the model results, different simulations were run at different current densities. These are compared to experimental measurements at the same charge/discharge currents.

These results are presented below for inserted charge of 1.5 A, 2 A, and 4 A. Discharge was performed at the same current, but in the opposite direction.

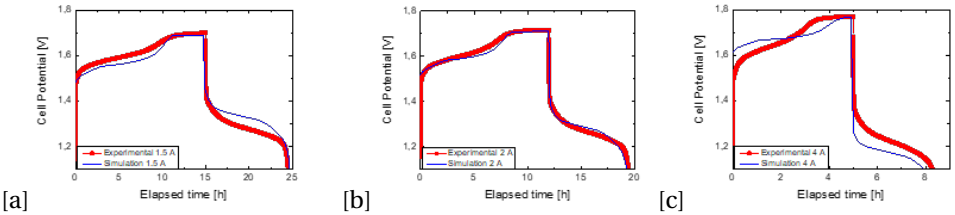

[a] [b] [c]

Figure A.7: Cell potential vs. elapsed time during a charging gas production cycle at (a) 1.5A (b) 2A and (c) 4A.

Generally speaking, the onset potential of the battery charging is fairly constant in experiments but strongly dependent on current density in the simulations. The parameters were fit to the 2A current as this is the rated current for the batteries. Further optimization simulations were run at the equivalent for 2A in a 2 electrode system since this is the rated current recommended by the battery manufacturer. Validation measurements at higher current densities are carried out only to determine whether the variations are significant.

The onset potential of HER/OER is accurate on all 3 experimental sets, and comparable to the simulation results. Furthermore, the battery capacity is estimated well for all 3 current values.

The discharging potential is overestimated for the 1.5 A measurement and underestimated for the 4 A results. This, together with the overestimation of the onset potential of the battery charging leads us to think that the ohmic drop might be higher in the model than in the experimental cell. As you increase the current the ohmic losses would increase disproportionately, resulting in a mismatch of potential. This can be due to the assumption that parameters such as the porosity and surface area are considered not to scale with SoC.

However, all 3 results are adequate to proceed with the optimization scenarios, as the simulated gas production values and the efficiency results at the rated charging current are accurate and comparable to the experimental results.

A.8. GAP THICKNESS AND ELECTROLYTE CONDUCTIVITY OPTIMIZATION

Gap thickness

The gap thickness was multiplied by a scaling factor to study the effect on battery and total efficiency In Figure A.8 (a) it can be seen how battery efficiency and total efficiency increase until the gap thickness is double the starting dimension of 3 mm on each side of the membrane. Because the products of the secondary reactions, namely H_2 and O_2 are produced in a gaseous state, the effect of product accumulation should be further studied. Furthermore, bubble accumulation and its effect on fluid dynamics will play a role in determining the optimal gap thickness for the battolyser.

Ohmic losses increase as the gap thickness increases, however this will also allow for bubble removal and more turbulent flow due to bubble movement. Since battery capacity and hydrogen production does not increase considerably, 3 mm gap thickness is chosen, but must be further studied to determine if a larger gap is beneficial. Barton et al. discuss the effect of increasing the gap thickness on the total ohmic losses in a similar battolyser cell[5].

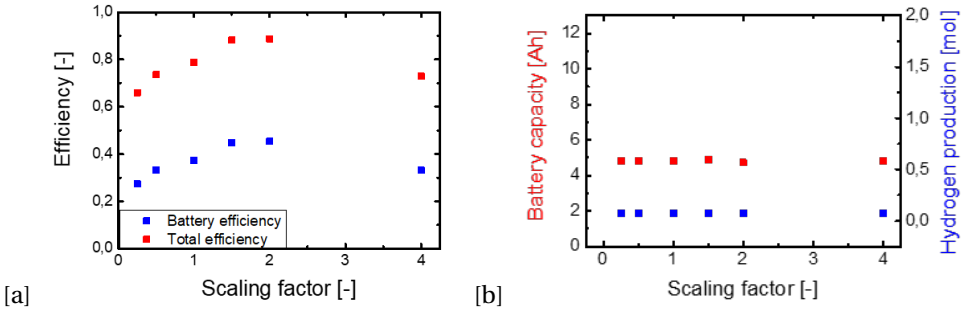

Figure A.8: (a) Battery and total integrated efficiency with respect to a scaling factor that multiplies the gap thickness (b) Battery capacity and total hydrogen production vs. gap thickness.

Ohmic losses are not dominating in this application because of low currents and high KOH conductivity. Therefore, the gap thickness is not the dominating contributor losses. Both the optimization of the electrolyte conductivity and the gap thickness were run to determine if they were important in further designs of the battolyser. Through these simulations it was determined that they were not as significant as other parameters

A

Electrolyte conductivity

The electrolyte conductivity was also optimized. Figure A.9 (a) shows the small increase in efficiency at half the value of the conductivity of the electrolyte. Since the increase is small, more information was looked at for this parameter optimization.

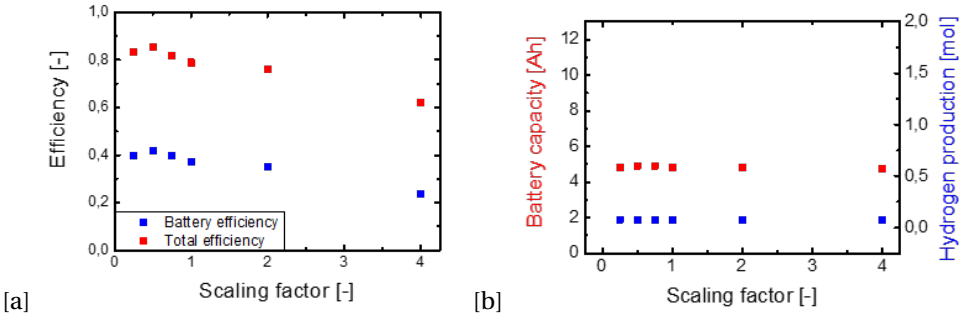

[a] [b]

Figure A.9: (a) Battery and total integrated efficiency with respect to the electrolyte conductivity (b) Battery capacity and total hydrogen production vs. electrolyte conductivity.

According to Gilliam et al. at room temperature, conductivity of KOH reaches a plateau value as the concentration increases. To consider cost effects of high electrolyte concentrations, for further optimization scenarios, 5 M KOH is used.[6] However, this should be studied further as the increase in efficiency at lower concentrations of electrolyte is not fully understood.

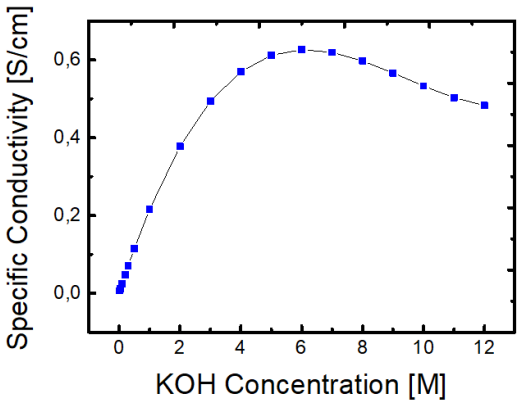

Figure A.10: Specific conductivity of KOH with respect to concentration at 20 °C. Data from Gilliam et al. [6]

A

A.9. ELECTROLYTE CONCENTRATION PROFILES CALCULATED WITH THE MODEL

The concentration profiles of OH^- concentration through the x-coordinate of the cell are presented in this section.

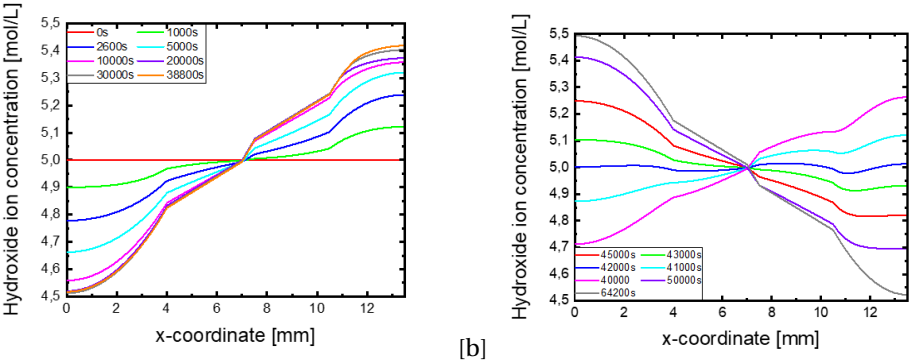

[a] [b]

Figure A.11: ((a) Hydroxide concentration profiles in the x-coordinate during charge and electrolysis (b) Hydroxide concentration profiles in the x-coordinate during discharge.

BIBLIOGRAPHY

[1] B. Paxton and J. Newman, "Modeling of nickel/metal hydride batteries", *Journal of the Electrochemical Society*, vol. 144, no. 11, p. 3818, 1997.

[2] S. Sinha, B. D. Humphrey, and A. B. Bocarsly, "Reaction of nickel electrode surfaces with anionic metal-cyanide complexes: Formation of precipitated surfaces", *Inorganic Chemistry*, vol. 23, no. 2, pp. 203–212, 1984.

[3] B. Conway and E. Gileadi, "Electrochemistry of the nickel oxide electrode: Part iv. electrochemical kinetic studies of reversible potentials as a function of degree of oxidation", *Canadian Journal of Chemistry*, vol. 40, no. 10, pp. 1933–1942, 1962.

[4] A. C. Garcia, T. Touzalin, C. Nieuwland, N. Perini, and M. T. Koper, "Enhancement of oxygen evolution activity of nickel oxyhydroxide by electrolyte alkali cations", *Angewandte Chemie International Edition*, vol. 58, no. 37, pp. 12 999–13 003, 2019.

[5] J. P. Barton, R. J. Gammon, and A. Rahil, "Characterisation of a nickel-iron battolyser, an integrated battery and electrolyser", *Frontiers in Energy Research*, p. 318, 2020.

[6] R. Gilliam, J. Graydon, D. Kirk, and S. Thorpe, "A review of specific conductivities of potassium hydroxide solutions for various concentrations and temperatures", *International Journal of Hydrogen Energy*, vol. 32, no. 3, pp. 359–364, 2007, Fuel Cells, ISSN: 0360-3199. DOI: https://doi.org/10.1016/j.ijhydene.2006.10.062. [Online]. Available: https://www.sciencedirect.com/science/article/pii/S0360319906005428.

B

Appendix Chapter 4

B.1. RDE results

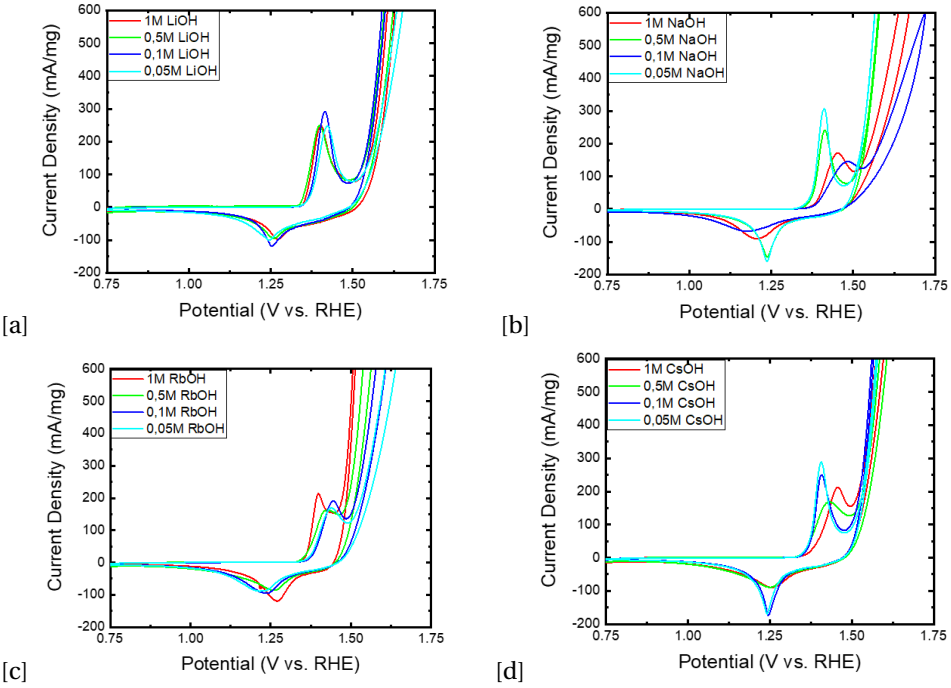

Figure B.1: (a)-(d) Cyclic voltammogram of a $Ni(OH)_2$ film deposited on a GC-RDE at 1600 rpm with 6.5 M MOH electrolytes, where M consists of the K^+ and Li^+, Na^+, Rb^+ and Cs^+ additions. (a) LiOH concentrations, (b) NaOH concentrations, (c) RbOH concentrations, and (d) CsOH concentrations added to a KOH electrolyte, while keeping the final OH^- contentration at 6.5 M.

Table B.1: Peak oxidation potential and peak reduction potential of cycle 3 of consecutive CVs shown in Figure B.1 compared to the average value of 3 consecutive cycles.

	Peak potential Oxidation Potential [V]		Peak potential Reduction Potential [V]	
	Cycle 3	Average 3 cycles	Cycle 3	Average 3 cycles
6.5M KOH	1.476	1.482	1.261	1.258
1M LiOH	1.402	1.406	1.272	1.271
0.5M LiOH	1.398	1.406	1.260	1.260
0.1M LiOH	1.415	1.417	1.253	1.252
0.05M LiOH	1.423	1.428	1.244	1.243
1M NaOH	1.453	1.471	1.207	1.196
0.5M NaOH	1.414	1.419	1.237	1.237
0.1M NaOH	1.484	1.511	1.174	1.159
0.05M NaOH	1.411	1.416	1.238	1.238
1M RbOH	1.399	1.396	1.270	1.271
0.5M RbOH	1.427	1.435	1.260	1.258
0.1M RbOH	1.444	1.452	1.241	1.235
0.05M RbOH	1.440	1.449	1.215	1.206
1M CsOH	1.457	1.464	1.254	1.255
0.5M CsOH	1.432	1.436	1.250	1.248
0.1M CsOH	1.407	1.409	1.246	1.246
0.05M CsOH	1.407	1.409	1.240	1.242

B.2. BATTERY CYCLING DATA COMPARISON

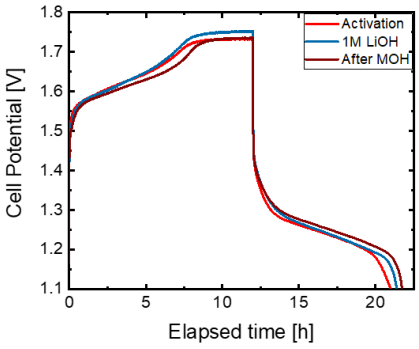

[a]

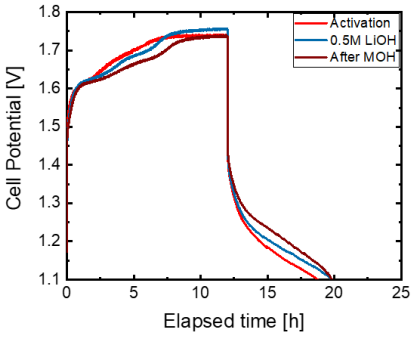

[b]

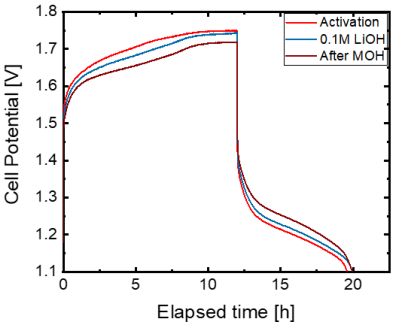

[c]

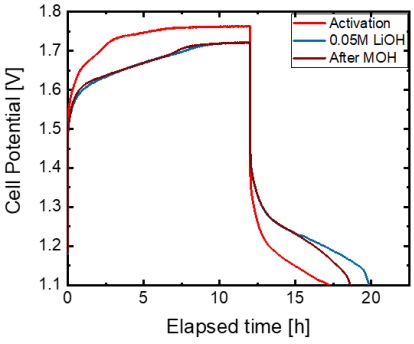

[d]

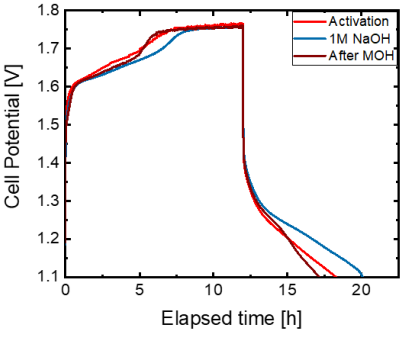

[e]

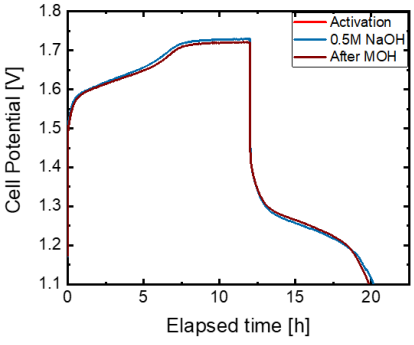

[f]

B

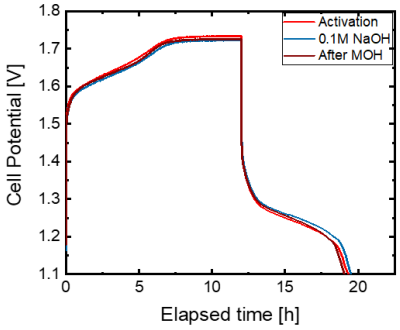
Activation
0.1M NaOH
After MOH
Cell Potential [V]
Elapsed time [h]

[g]

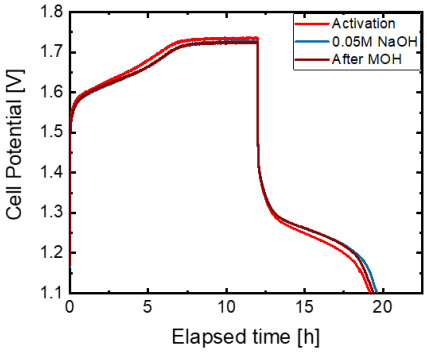
Activation
0.05M NaOH
After MOH
Cell Potential [V]
Elapsed time [h]

[h]

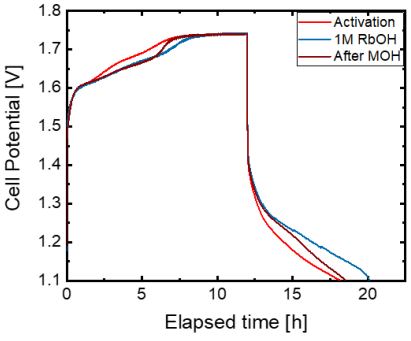
Activation
1M RbOH
After MOH
Cell Potential [V]
Elapsed time [h]

[i]

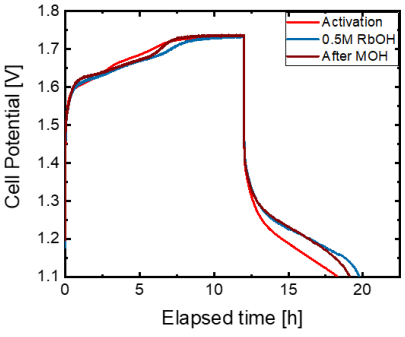
Activation
0.5M RbOH
After MOH
Cell Potential [V]
Elapsed time [h]

[j]

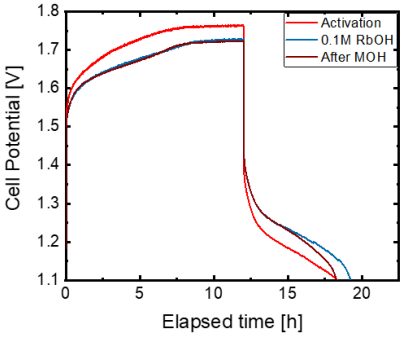
Activation
0.1M RbOH
After MOH
Cell Potential [V]
Elapsed time [h]

[k]

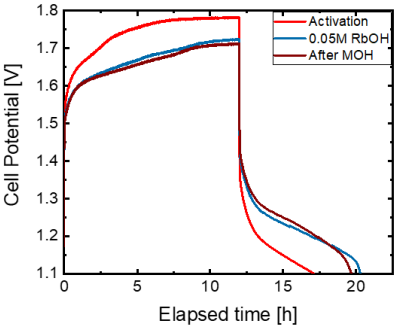
Activation
0.05M RbOH
After MOH
Cell Potential [V]
Elapsed time [h]

[l]

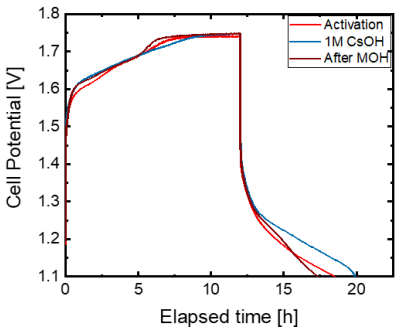

[m]

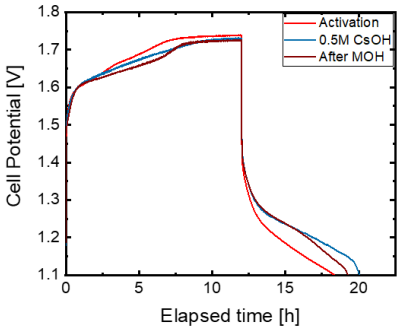

[n]

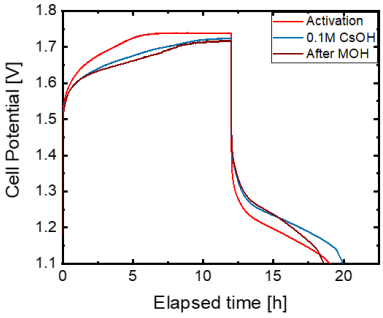

[o]

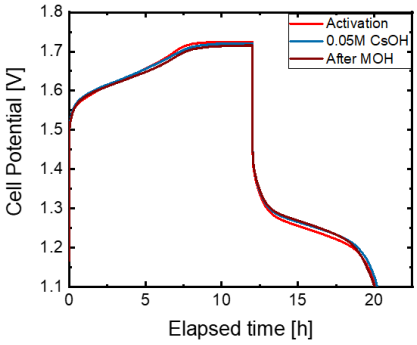

[p]

Figure B.2: Battery charge/discharge cycles with different MOH concentration additions.

B.3. SEM IMAGES FOR THE NICKEL ELECTRODE USED IN 1 M MOH BATTERY CYCLING EXPERIMENTS

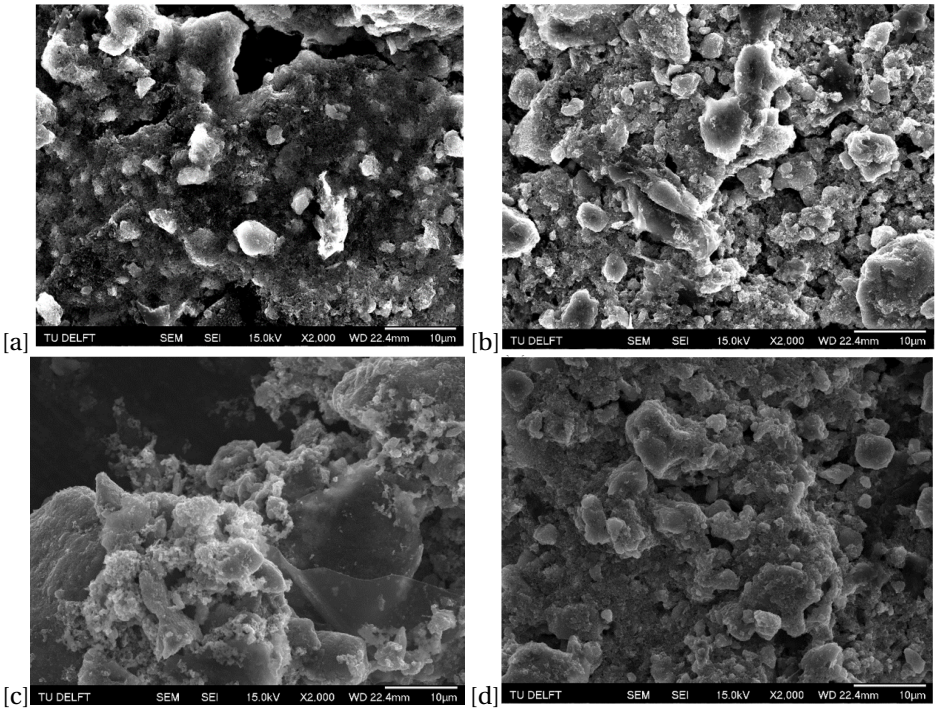

Figure B.3: SEM SEI images at x2000 magnification of the nickel electrode material from batteries with the highest concentrations of alkali metal cations. (a) 1M LiOH + 5.5M KOH, (b) 1M NaOH + 5.5M KOH, (c) 1M RbOH + 5.5M KOH, (d) 1M CsOH + 5.5M KOH.

B.4. ELEMENTAL COMPOSITION OF THE COMMERCIAL NICKEL ELECTRODE MATERIALS

Inductively Coupled Plasma Optical Emission Spectroscopy (ICP-OES) was used as an analytical technique to determine the elemental composition of a sample. Samples are dissolved in H_2O_2 and digested close to boiling point for 4 hours. Then the samples were diluted in 3 v% HNO_3. This liquid is injected in the form of aerosol into an argon plasma. The plasma excites the atoms and ions, causing them to emit electromagnetic radiation at a particular wavelength characteristic to a particular element. The intensity of the emission is proportional to the concentration of the element

The elemental composition of the active material inside the pockets was obtained by ICP-OES analysis. The electrode pockets were opened and the compacted material was extracted. The results are presented in Table B.1.

Table B.2: ICP-OES results for the nickel electrode sample

Element	Nickel Electrode Mass Percentage [%]
Fe	0.100
Ni	93.253
Al	0.012
$SO_4{}^{-2}$	0.146
Li	4.636
Na	4.636
Zn	0.037
Si	0.062
$PO_4{}^{2-}$	0.102
Cd	0.013
Sn	0.013
Ca	0.022
Ti	-
Ba	-

Due to the dilution process, carbon is not included in ICP-OES analysis results. The nickel hydroxide positive electrode, as expected, is composed mainly of nickel. As the material comes from commercial electrodes that have been used in Ni-Fe batteries, some iron is also present in the nickel electrode. This can be due to crossover during charging and discharging cycles because of the solubility of iron in KOH. This is expected as the sediment found in the bottom of the battery has a high mass percentage of iron. The iron crossover can decrease the overpotential for oxygen evolution in NiOOH materials[1]. Lithium and sodium can be present because of the use of LiOH and NaOH in the KOH electrolyte during previous battery cycles. Zn, Cd, and Sn are typical HER inhibitors, and are believed to have been added to the iron electrode to avoid the secondary reaction. Cadmium and cobalt are used as additives to the nickel hydroxide electrode to increase the conductivity and the oxygen evolution potential.

B.5. RDE SETUP

[a] 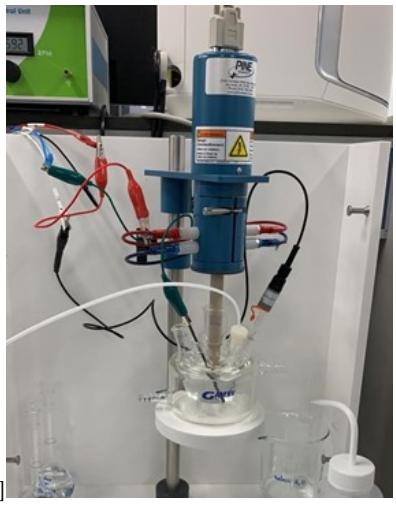

[b] 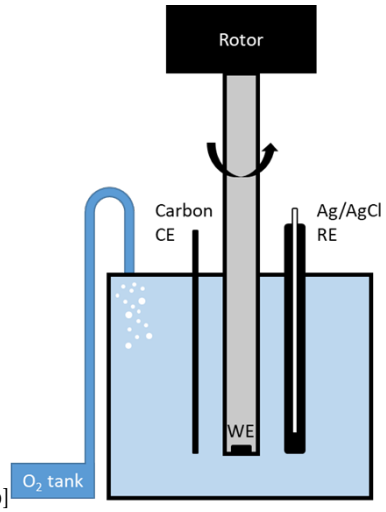

Figure B.4: (a) Photograph and (b) schematic of the RDE setup used for experiments.

B.6. BATTERY CYCLING SETUP

A BioLogic BCS-815 Battery cycler was used to run the charge/discharge cycles on commercial NiFe batteries (Ironcore Batteries). Galvanostatic charge/discharge cycles were performed with a potential limitation of 1.1 V to avoid over-discharging. The capacity of these batteries is 10Ah. The charge/discharge cycles were performed using a recommended charging rate of C/5 and a discharge rate of C/6.6. This coincides with a constant current of 2 A during charging and -1.5 A during discharge. The long-term battery experiments were performed in a highly resistant plastic enclosure, namely the cell where the commercial batteries are sold. This ensures that the experiments are performed in highly alkaline resistant cells.

[a] 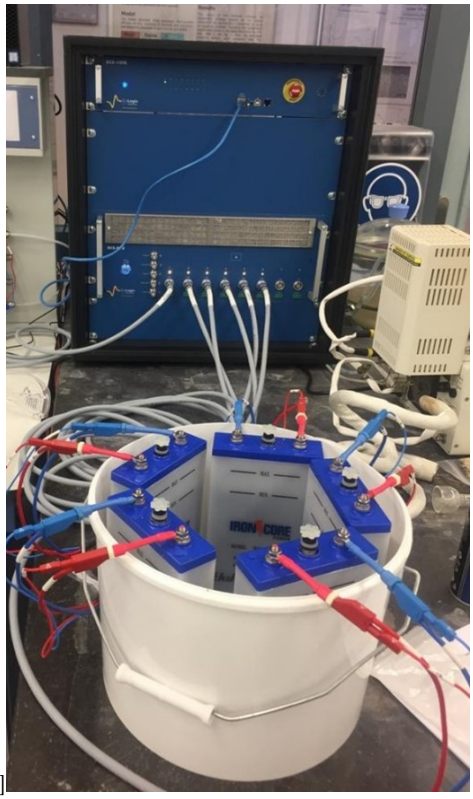 [b] 

Figure B.5: (a) Photograph of the (a) Battery charging setup and (b) commercial Ni-Fe IronCore batteries used for experiments.

B.7. ADDITIONAL CVS

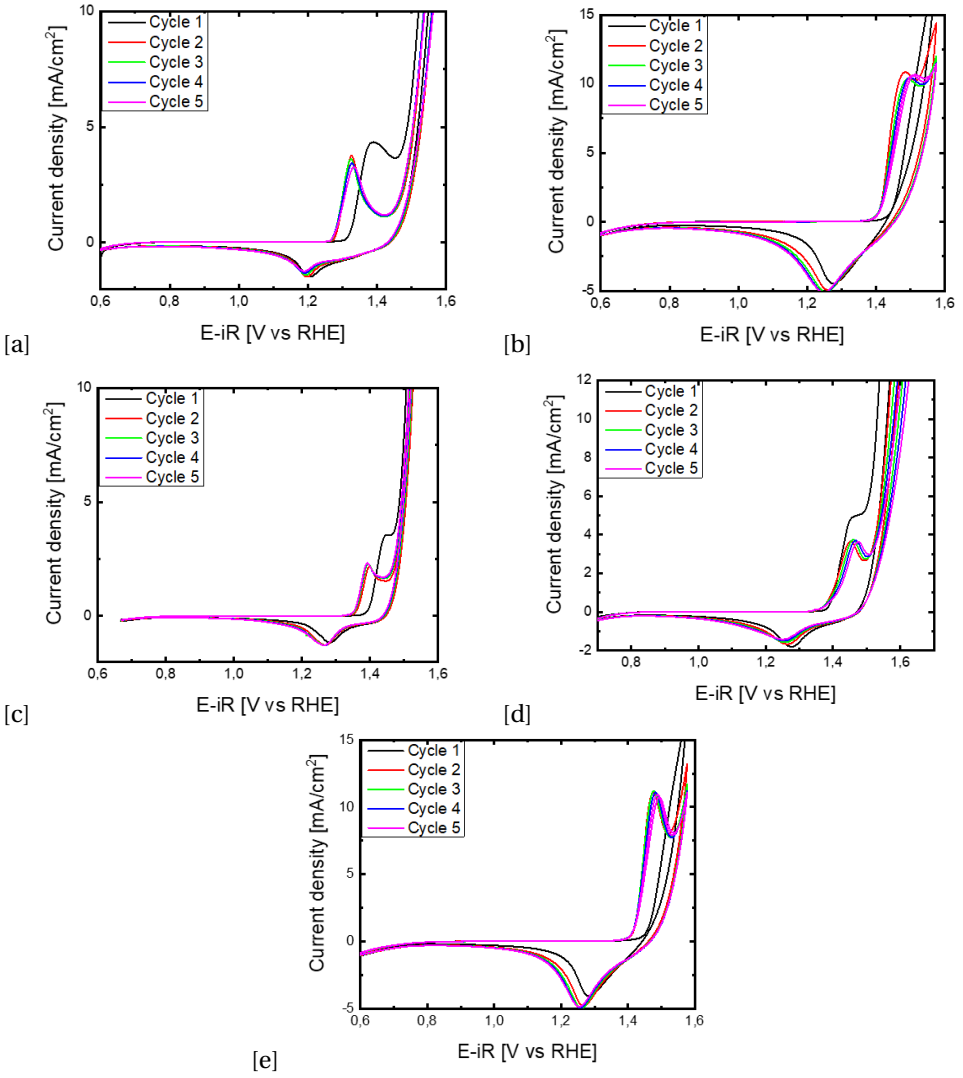

Figure B.6: Cyclic voltammograms of $Ni(OH)_2$ material deposited on a GC electrode recorded in different electrolytes with a total OH- concentration of 6.5 M. Measurements were performed using an RDE setup with a rotation speed of 1600 rpm and the voltammograms were recorded at scan rate of 20 mV s1 in the following electrolyte compositions: (a) 5.5M KOH + 1M LiOH, (b) 5.5M KOH + 1M NaOH, (c) 5.5M KOH + 1M RbOH, (d) 5.5M KOH + 1M CsOH, (e) 6.5M KOH.

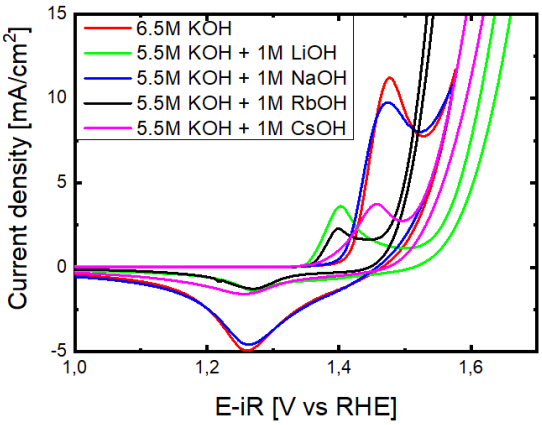

Figure B.7: Figure 1 with current density in mA/cm-2, using the geometric surface area of the GC electrode.

BIBLIOGRAPHY

[1] A. C. Garcia, T. Touzalin, C. Nieuwland, N. Perini, and M. T. Koper, "Enhancement of oxygen evolution activity of nickel oxyhydroxide by electrolyte alkali cations", *Angewandte Chemie International Edition*, vol. 58, no. 37, pp. 12 999–13 003, 2019.

C

Appendix Chapter 5

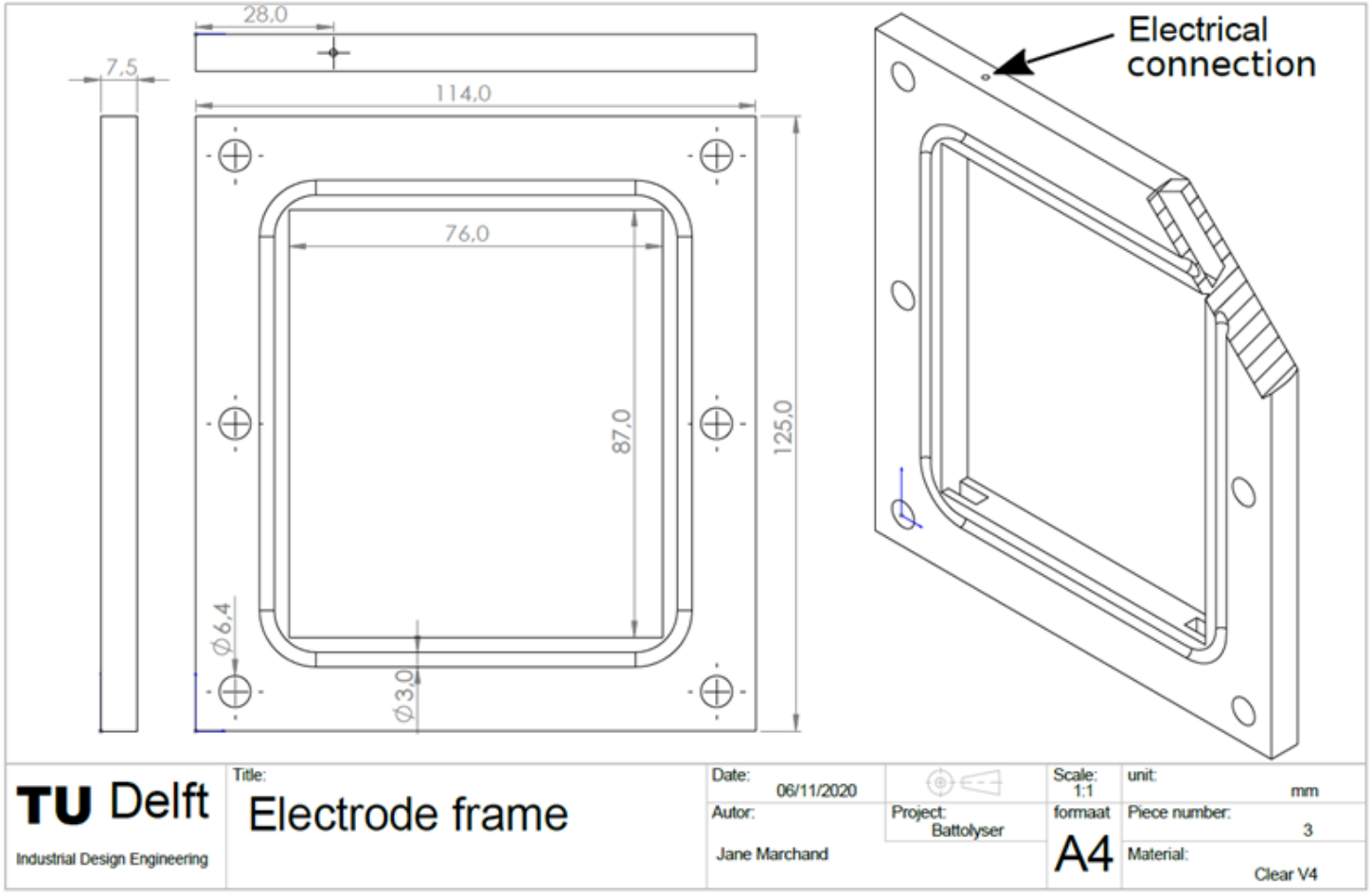

Figure C.1: Electrode frame

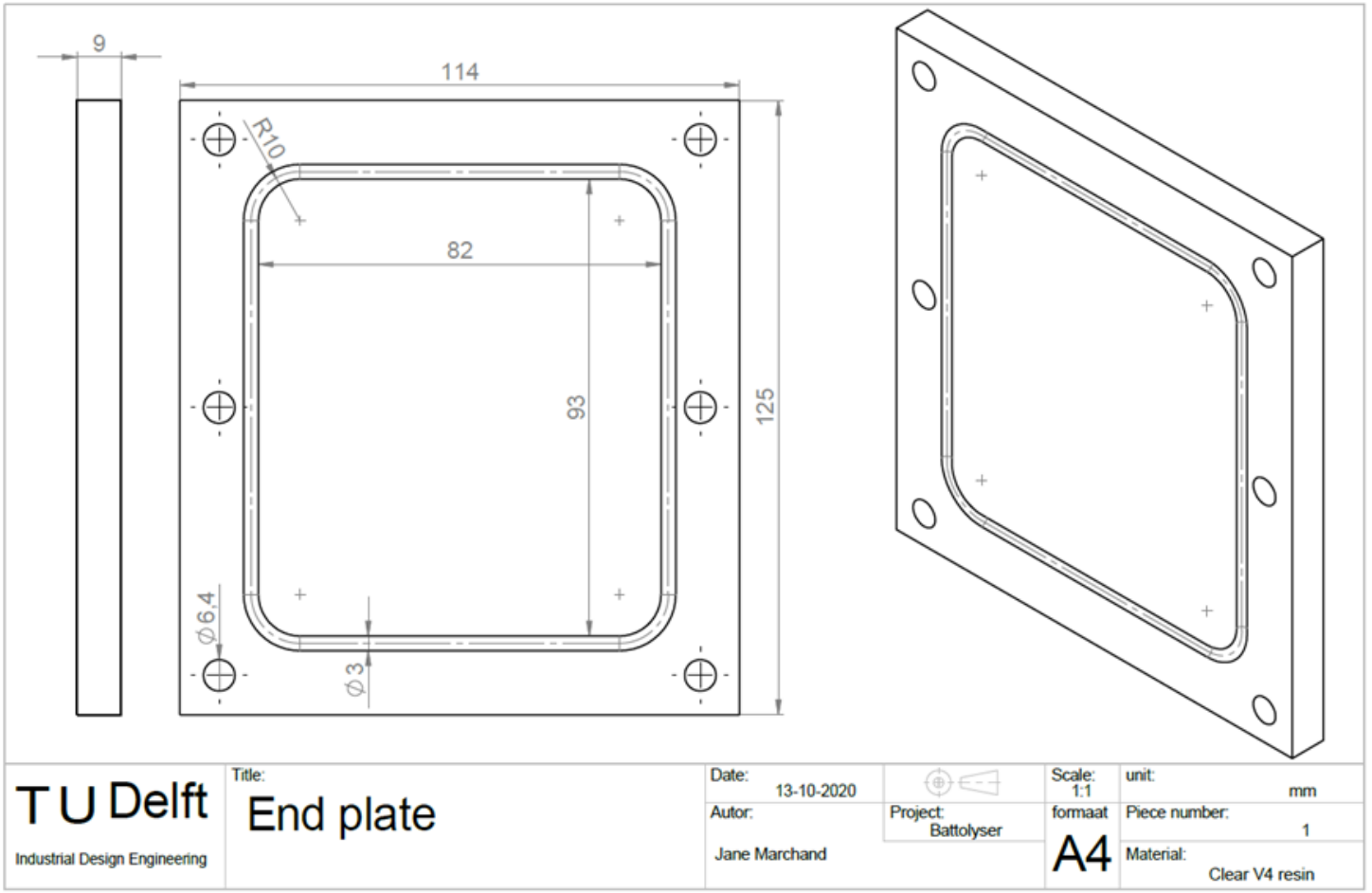

Figure C.2: End plate frame

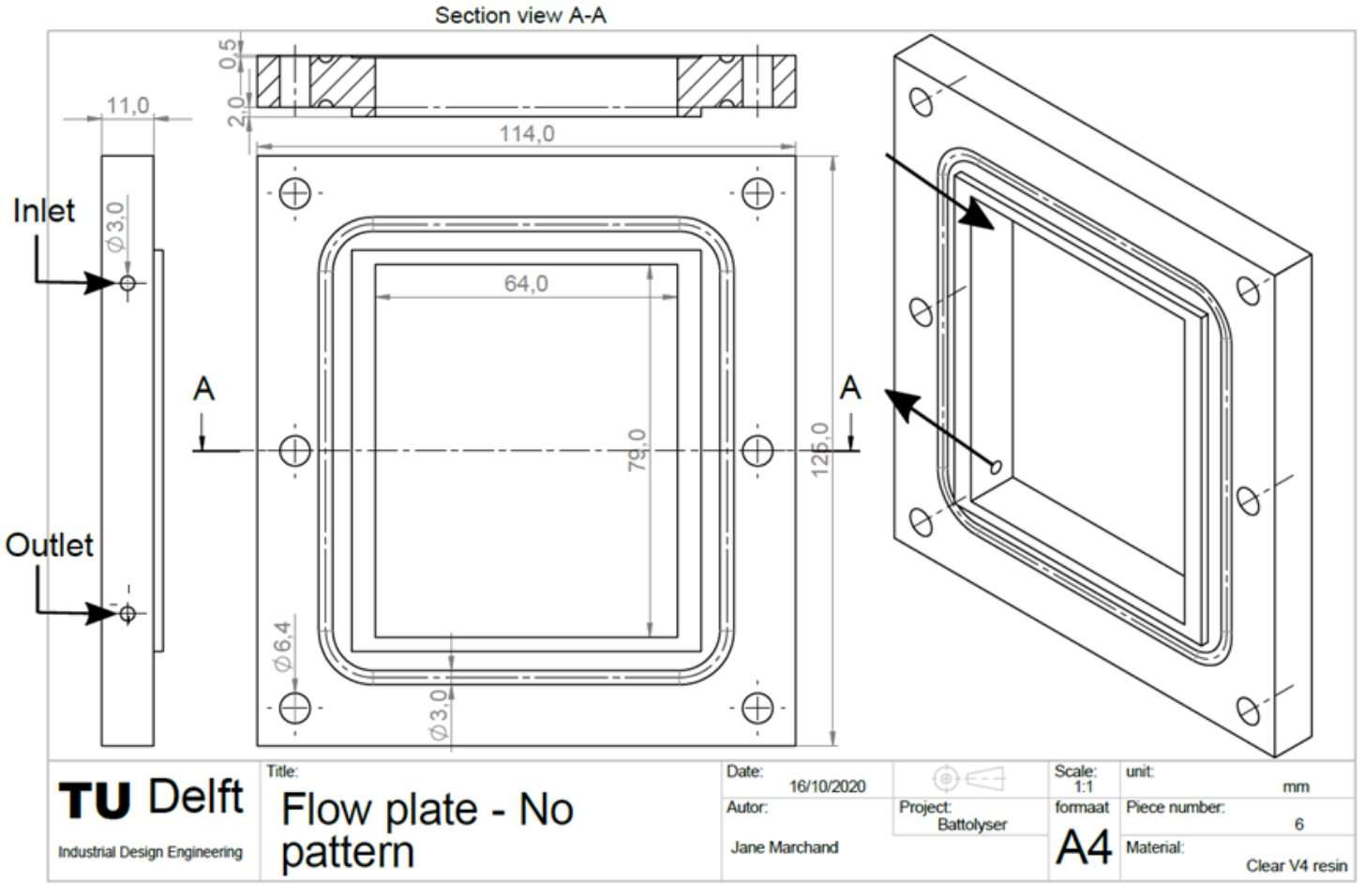

Figure C.3: Empty flow plate pattern frame

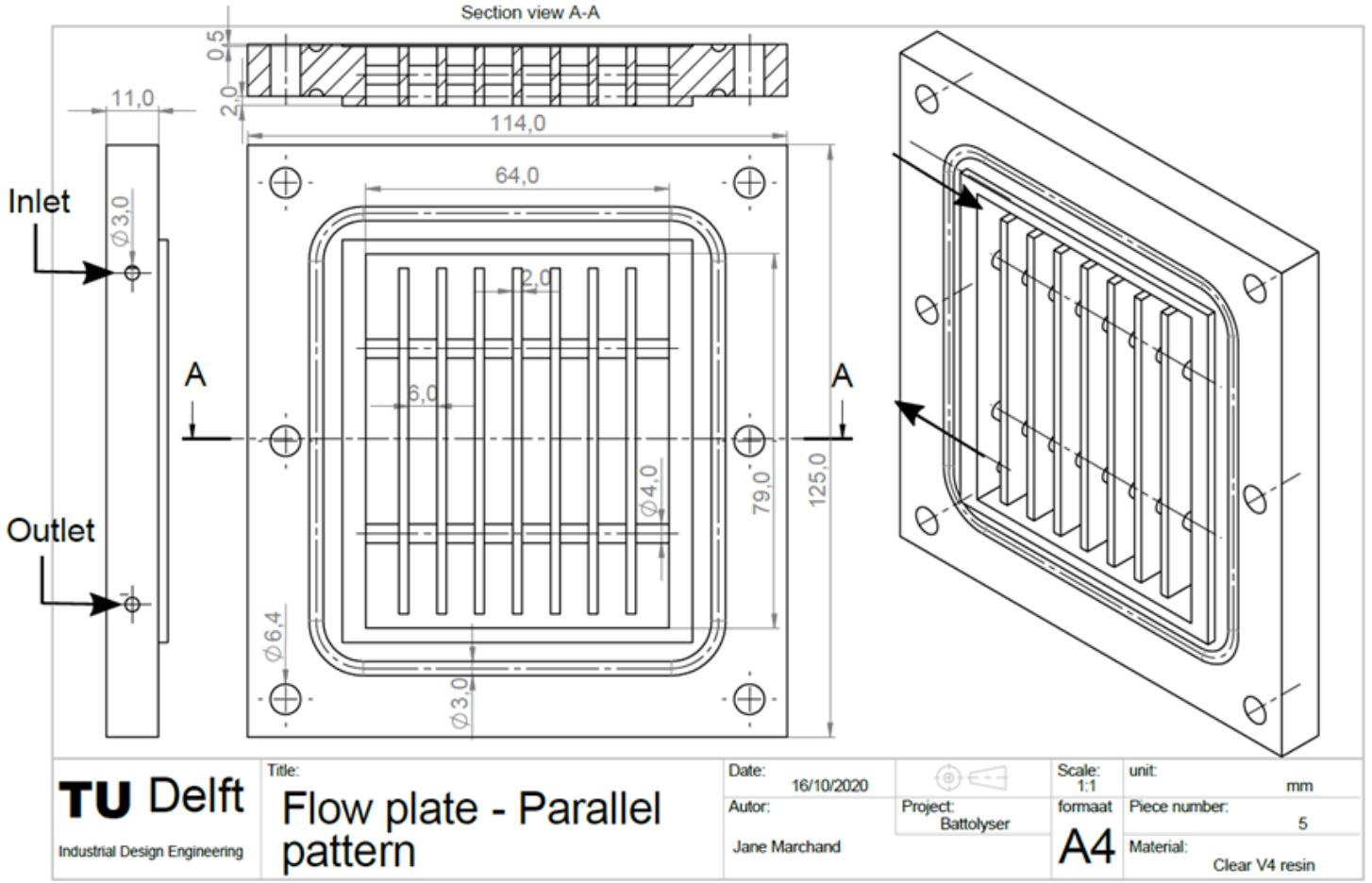

Figure C.4: Parallel flow pattern frame

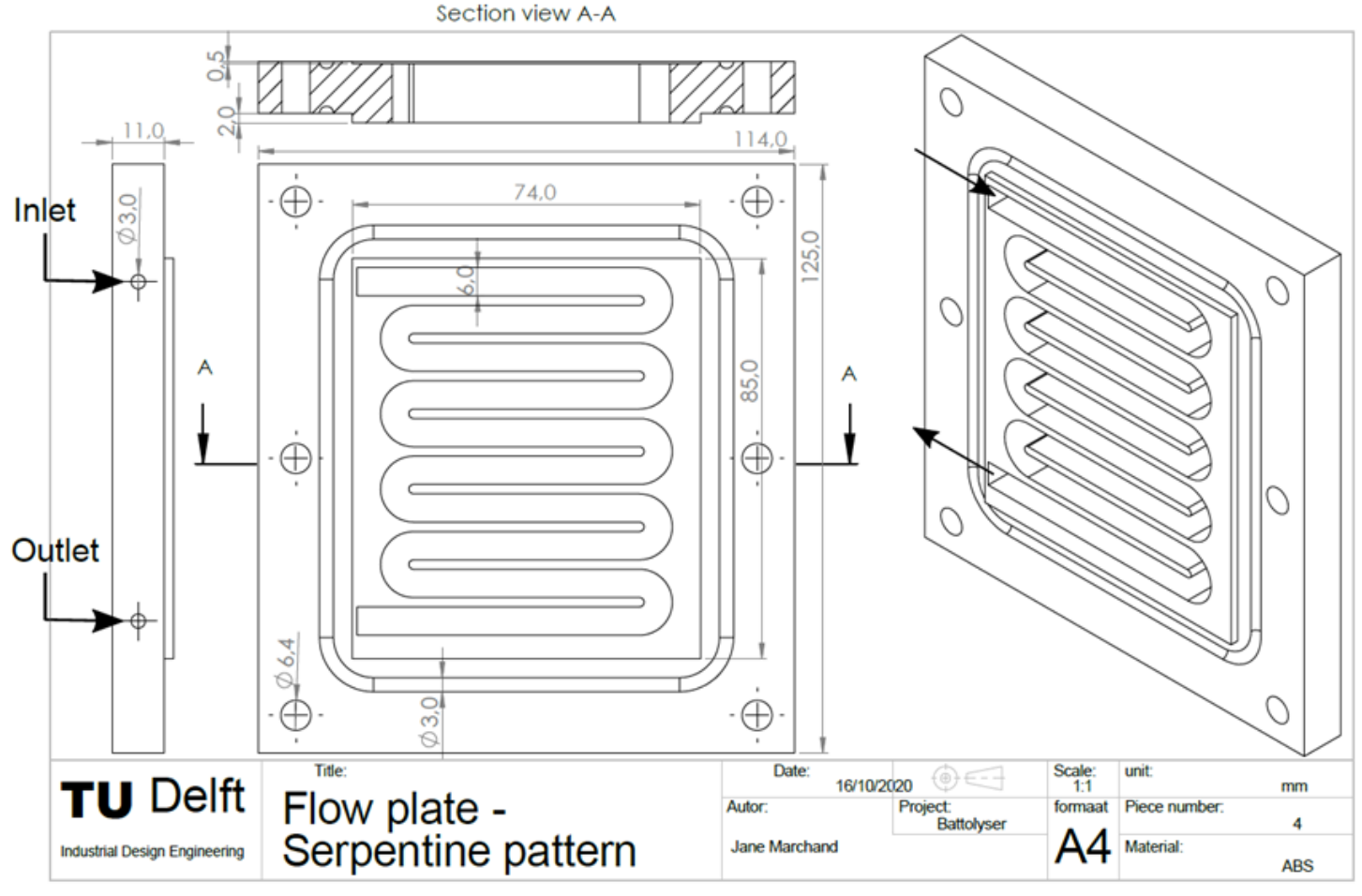

Figure C.5: Serpentine flow pattern frame

D

NOMENCLATURE

Variables and greek symbols used throughout the document are presented in Table D.1.

Table D.1: Variables and greek symbols used throughout the document.

Variable	Definition	Units
A	Arhenius pre-exponential factor	$[s^{-1}]$
a_i	Activation energy	[J/mol]
A	geometric area	$[m^2]$
c	concentration	$[mol/m^3]$
D	Diffusivity	$[m^2/s]$
d_b	characteristic length scale	[m]
E^0	Standard Cell Potential	[V]
i	Current	[A]
j	Current density	$[A/m^2]$
j_0	Exchange current density	$[A/m^2]$
n	number of electrons	[-]
N	Flux	$[mol/(m^2 \mathring{u} s)]$
R	Universal gas constant	[J/(K·mol)]
R	Resistance	[]
R	Radius	[m]
Re	Reynolds number	[-]
SoC	State of Charge	[%]
Sc	Schmidt number	[-]
Sh	Sherwood number	[-]
t	time	[s]
T	Absolute temperature	[K]
u	velocity vector	[m/s]
u_m	mobility	[s·mol/kg]
v	Rate of reaction	$[k^{-1}]$

Table D.1: Variables and greek symbols used throughout the document.

Variable	Definition	Units
V	Volume	$[m^3]$
z	valence of ionic species	[-]
Greek symbols		
α	charge transfer coefficient	[-]
γ	Bruggeman coefficient	[-]
ΔG	Gibbs free energy	[kJ/mol]
ΔH	Change in Enthalpy	[kJ/mol]
ΔS	Change in Entropy	[kJ/mol]
ϵ	Porosity	[-]
η	activation overpotential	[V]
θ	Bubble coverage	[%]
ϕ	potential	[V]
σ	conductivity	[mS/cm]
υ	kinematic viscosity	$[m^2/s]$

Subscripts, superscripts and abbreviations used throughout the document are included in Table D.2

Table D.2: Subscripts, superscripts and abbreviations used throughout the document.

Subscripts	
anode	Refers to the anode of the electrochemical cell
cathode	Refers to the cathode of the electrochemical cell
cell	Refers to the overall electrochemical cell
i	Refers to the chemical species i
s	solid
l	liquid
max	maximum
Superscripts	
eff	effective
Abbreviations	
AEL	Alkaline electrolysis
CV	Cyclic voltammetry
DC	Direct current
EDX	Energy-dispersive X-ray spectroscopy
FFP	Flow Field Pattern
GC	Glassy carbon
GD	Gas Chromatography
HER	Hydrogen evolution reaction
ICP-OES	Inductively Coupled Plasma Optical Emission Spectroscopy
LCOS	Levelized Cost of Storage
LDH	Layered double hydroxides
OER	Oxygen evolution reaction
PCCEL	Proton conductive ceramic electrolysis
PEIS	Potentiostatic electrochemcial impedance spectroscopy
PEMEL	Proton exchange membrane electrolysis
RDE	Rotating disk electrode
RHE	Reversible hydrogen electrode
SEM	Scanning electron microscope
SoC	State of Charge
SOEL	Solid oxide electrolysis
TCD	Thermal conductivity detector
TRL	Technological Readiness Level

Curriculum Vitæ

Andrea Mangel Raventos was born in San Jose, Costa Rica and studied Chemical Engineering at the University of Costa Rica. She worked in a PVC processing plant and subsequently at the University of Costa Rica, both as a lecturer and researcher.

In 2014 she moved to the Netherlands to do her MSc degree in Sustainable Energy Technology at TU Delft. Her master thesis was focused on the development of a semiconductor photoelectrode for direct solar to hydrogen conversion in a multidisciplinary project with the Photovoltaic Materials and Devices (PVMD) research group and the Materials for Energy Conversion (MECS) research group. During this time she worked as a teaching assistant in the Photovoltaics Laboratory and in the development of a Sustainable Energy Massive Open Online Course (MOOC).

In March of 2017 she started a PhD in the Process and Energy department of the Mechanical, Maritime and Materials Engineering Faculty, on the upscaling of an integrated battery and electrolyser system (the Battolyser). In 2019, she was awarded a Marina van Damme award to pursue a leadership course for women in Science, Technology, Engineering, Maths and Medicine (STEMM).

List of Publications

- **Andrea Mangel Raventos** and Ruud Kortlever. Effect of different alkali metal cations on the oxygen evolution activity and battery capacity of nickel electrodes in concentrated hydroxide electrolytes. *Electrochimica Acta* 2022 415, 140255.

- **Andrea Mangel Raventos**, Gerard Kluivers, J.W. Haverkort, Wiebren de Jong, Fokko M. Mulder, and Ruud Kortlever. Modeling the Performance of an Integrated Battery and Electrolyzer System. *Industrial & Engineering Chemistry Research* 2021 60 (30), 10988-10996

- Paula Perez-Rodriguez, Drialys Cardenas-Morcoso, Ibadillah A. Digdaya, **Andrea Mangel Raventos**, Dr. Paul Procel, Dr. Olindo Isabella, Dr. Sixto Gimenez, Prof.Dr. Miro Zeman, Dr. Wilson A. Smith, Prof.Dr. Arno H. M. Smets. Improving the Back Surface Field on an Amorphous Silicon Carbide Thin-Film Photocathode for Solar Water Splitting. *ChemSusChem* 2018, 11, 1797 – 1804

- Paula Perez-Rodriguez, Ibadillah Digdaya, **Andrea Mangel Raventos**, Michael Falkenberg, Ravi Vasudevan, Miro Zeman, Wilson Smith, Arno H.M. Smets. Solar Fuel Production by Using PV/PEC Junctions Based on Earth Abundant Materials. 2016 IEEE 43rd Photovoltaic Specialists Conference (PVSC). DOI:10.1109/PVSC.2016.7750348.